ABSTRACT

Title of Thesis: INVESTIGATING THE STABILITY OF THE BLUE WHIRL

Lanford Shelley Price
Master of Science
2021

Thesis Directed By: Michael J. Gollner
Assistant Professor
Department of Mechanical Engineering,
University of California, Berkeley

The blue whirl, recently discovered while studying oil spill remediation over a water surface, sparked interest because of its soot free, fuel flexible nature. Preliminary experimentation, performed with buoyancy induced airflow via two lifted and offset quartz glass half-cylinder shells, revealed information about the flame's

structure, flow profile, and exhaust gas emissions and particulate. Additionally, several computational models produced results detailing flame structure and flow field. Questions regarding the impact of forced flow conditions and fuel type on flame stability and formation, however, remain unanswered. To answer these questions, an advanced experimental apparatus was developed. Varying forced airflow and fuel types were tested and measured against blue whirl flame stability. Further, hysteresis tests for airflow and fuel flow were performed. Stable blue whirls were observed across each airflow profile and fuel type. System response to fuel type was seen to be non-uniform. Lastly, hysteresis was only observed for airflow.

INVESTIGATING THE STABILITY OF THE BLUE WHIRL

by

Lanford Shelley Price

Thesis submitted to the Faculty of the Graduate School of the
University of Maryland, College Park, in partial fulfillment
of the requirements for the degree of
Master of Science
2021

Advisory Committee:
Professor Michael J. Gollner, Chair
Professor Arnaud Trouve, Full Member
Professor Peter Sunderland, Full Member

Acknowledgements

It's important this thesis start with the thanks and recognition due to Dr. Paul Anderson. Paul has proved an excellent mentor since I began my research fellowship at ARL in the fall of 2019. Paul has been instrumental in my development as a researcher and engineer. He helped guide my literature review, design and manufacturer our advanced burner, and produce the results detailed within this document. His creativity, hunger for excellence, and aptitude for experimentation are invaluable. I will always strive to achieve the standards set forth by Paul. I am forever thankful for my time at ARL, and I am forever thankful for the mentorship and friendship Paul and I have shared.

Of course, this thesis wouldn't be possible without my advisor, Dr. Michael Gollner. Michael, too, provided invaluable insight to project and still offered plentiful support from across the country at a different university. I'm very grateful to have been able to work with such a dedicated advisor.

I'd like to sincerely thank Dr. Sriram Hariharan. Ram's enthusiasm and kindness have been much appreciated over these last two years. Further, his knowledge surrounding the blue whirl is vast. When in discussion with Paul, Ram, and Michael, I am frequently reminded that I truly stand on the shoulders of giants.

I'd like to thank Dr. Peter Sunderland and Dr. Arnaud Trouve for serving on my advisory committee. Both professors are exceedingly knowledgeable about fires and flames, and I am humbled to have their input on my thesis.

Finally, I'd like to thank my friends and family, including those lost along the way, that helped me attain the goals I've reached today. It has been through your love and support that I have excelled, succeeded, and remained grounded.

Table of Contents

List of Figures

List of Tables

Chapter 1: Introduction

Fire whirls, a naturally occurring swirling flame, have been extensively studied for years. A variety of fire whirl-generating burners have been implemented for research. A rather common approach utilizes buoyancy induced flow [1]. Air is entrained circumferentially, drawn in from the low pressure region that exists at the center of two quartz glass half-cylinder shells. Studying the fire whirl's potential effectiveness for oil spill remediation over a water surface, a phenomenon named the blue whirl was discovered [2]. Xiao et. al used a configuration similar to that depicted in Figure 1 (Figure 1 shows the quartz glass half-cylinder shells suspended over an aluminum surface, not a water surface). Perhaps the most significant change to the burner setup used in [2] is the inclusion of a lift of the quartz shells (h in Figure 1).

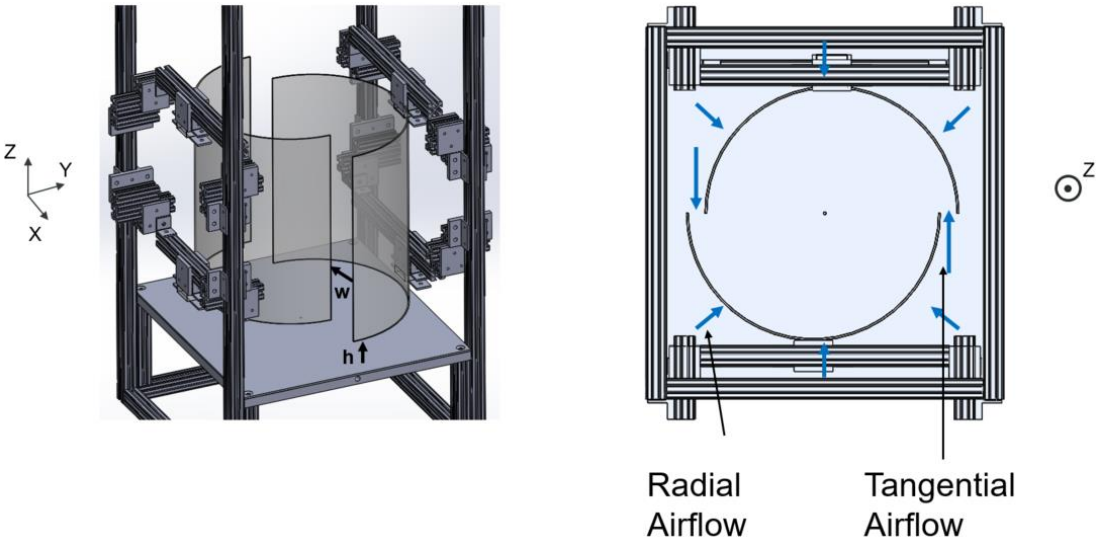

Figure 1: Left: Preliminary Blue Whirl Burner. The offset, w, allows for air to be drawn in tangentially to the centrally located fuel port. Similarly, the lifted height, h, allows for air to be drawn in radially along the boundary layer. Right: Airflow induced upon ignition. Depicted from the top down viewpoint.

The flame regime was seen to appear transitioning from a fire whirl. Upon formation, the blue whirl was readily identifiable. The typically sooty fire whirl had been replaced by an entirely blue flame, indicating soot free combustion of a typically sooty fuel. Geometric properties, in particular a cone at the base, bright blue rim in the center, and purple haze region atop, also served as testament to the drastically different flame regime that had formed. Figure 2 shows what the transition from a fire whirl to a blue whirl may have looked like.

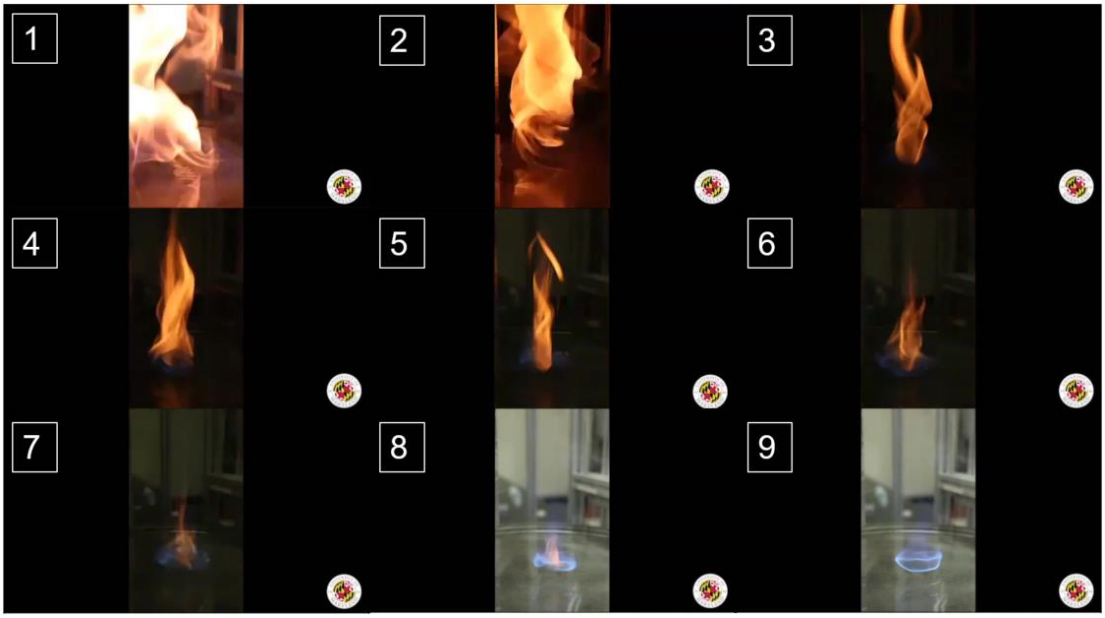

Figure 2: (1) pool fire; (2) fire whirl; (3)-(8) transition whirl – note the lifting of the flame, particularly evident in (7) and (8); (9) the blue whirl.

The combination of the key traits of the blue whirl are as follows:

(1) Complete combustion of a range of liquid fuels; (2) no atomization or pre-vaporization required of the fuel; (3) flame formation demonstrated with water

contaminants; (4) demonstrated with a buoyancy induced flow under ambient pressure conditions; and (5) soot free combustion. Combined, these traits hint at the potential for a fuel flexible energy conversion technology. The caveat, thus far, is size. Blue whirls formed in the lab have not surpassed 1 kW of heat release. Compared to industrial combustion technologies, producing 1000s of kW of energy, scaling up of the flame will be required for this flame regime to be of use as a fuel flexible energy conversion technology.

Thus far, all experimental and numerical methods have studied the blue whirl under buoyancy driven conditions. Further, although the flame appears to have some fuel flexible characteristics, the impact of fuel type and chemical structure remain unknown. Additionally, it is unclear why the blue whirl flame regime has only been demonstrated transitioning from a fire whirl. To help further the fundamental understanding of the blue whirl, this study sought to tackle these unknowns by investigating four things: (1) the effect of circumferential flow profile on blue whirl flame stability and soot production; (2) the effect of flame state on blue whirl formation; (3) the effect of fuel type on blue whirl flame stability and soot production; and (4) the effect of fuel flow on flame stability and soot production.

To address these questions, a new advanced experimental apparatus was designed and fabricated around independent variables of interest (suggested in [3]). A post processor, written in python, was implemented to extract flame characteristics from images captured during experimentation. Three circumferential flow profiles and fuel types were tested against flame stability and soot production to understand

the relationship and impact on the blue whirl. To address the formation characteristics of the blue whirl, hysteresis tests as a function of air and fuel flowrate were also performed. The results are presented as a function of radial and circumferential flowrate as well as radial flowrate and circulation. Explanations for blue whirl formation and flame stability are proposed for each circumferential flow profile tested. Reasons for the need to transition from a fire whirl to a blue whirl are suggested. Lastly, the impact of fuel type and fuel flow are analyzed.

Chapter 2: Literature Review

2.1 Fire Whirls

This section provides relevant information required for understanding the blue whirl, a flame regime that stems from fire whirls.

2.1.1 Fire Whirl Formation and Structure

Fire whirls are known by many names, but are identified as an intensification of combustion with whirling flame [1]. They are observed in nature in both wildland and urban large scale burning events. Although fire whirls are nothing new, they have remained an elusive phenomenon to understand because of their inherent non-static behavior. Because of their difficulty to measure in nature, experiments have predominantly been performed in laboratories. The most influential parameters for fire whirls can be found in the governing equations of mass, momentum, and energy [1]. The parameters of interest are U_r, U_z, Γ, H, and $\dot{m}$. Here, the time average velocity

vector U has components U_r, U_θ, U_z. Thus, the parameters U_r, U_z represent the radial and axial components of velocity. Γ represents circulation and is equal to $2\pi r U_\theta$. H represents flame height and $\dot{m}$ the mass burning rate.

Fire whirls can be classified into two types: (1) on source; (2) off source [1]. Hartl et. al define each by the following rules: a fire whirl is said to be on source if it forms directly over the fuel source; alternatively, a fire whirl is said to be off source if it forms offset from the fuel source. These off source fire whirls have also been observed in nature. Zhou et. al describes how surrounding fire, impinging upon oxidizer flow to a central flame, can generate this off source fire whirl [4]. Fire whirls can further be classified by their height, H, often used as the characteristic length scale. Small scale fire whirls are defined as a fire whirl with flame heights between 0.1 and 1.0 m [5]. Medium and large scale fire whirls are classified by flame heights between 1 and 10 m, and on the order of tens to hundreds of meters respectively [5].

Three mechanisms are required for fire whirl formation: (1) the presence of an eddy and an eddy generating mechanism; (2) a fluid sink present with an eddy; and (3) friction or drag to the air movement at the lower boundary by a horizontal surface [6]. The fluid sink is created by the fire and plume naturally driving flow radially to the vortex [1]. The trick then, is the eddy mechanism. In nature, the eddy mechanism is generated and channeled from topological features and obstructions [7]. Further, other flames, as described by Zhou and Liu et. al [4], [8], or general rotation of horizontal vorticity to vorticity about the z axis, as described by Emori et. al [9], due to heat, also serve to generate the eddy mechanism. Different apparatuses have been

used to generate fire whirls in laboratory settings to form and sustain a fire whirl flame regime. There are four main apparatus types for generating fire whirls [1]. These are: (1) two half shells, offset with open slits; (2) four walls, offset with slits; (3) circular cylindrical air intake; and (4) a rotating mesh screen. In each design, hot exhaust gas exits the top of the enclosure, venting to atmosphere. Cool ambient air is entrained tangentially. As Γ increases, the spiraling flame, formed from a pool fire, transitions to a fire whirl [1], [6]. These systems generate the on source, quasi-steady fire whirls that have been studied extensively in the literature [2], [10], [19], [11]–[18].

Emmons et. al presented their findings from their rotating mesh setup. Of note is their temperature measurements. These measurements were averaged to account for flame wander and were taken with a tungsten wire used as a resistance thermometer. A key take-away from their temperature measurements is the observed fuel rich condition in the fire whirl's core. Further, through velocity measurement, Emmons et. al confirmed the hypothesis that outside the vortex core, the velocity profile is that of a free vortex. PIV measurements taken by Hartl et. al agree [19].

2.2 The Blue Whirl

The blue whirl was first discovered in 2016 while researching oil spill remediation techniques over a water surface [2]. The experimental setup consisted of two quartz glass half-cylinder shells suspended over a pan containing water (shown in Figure 1). The shells were offset, creating a vertical slit between the two. This offset

permitted air to be entrained tangentially in the circumferential direction. For preliminary experimentation, fuel was poured into the enclosed space. Upon ignition, a pool fire formed, proceeded by a tall fire whirl. Xiao et. al describe how the fire whirl further transitioned to a flame regime now known as the blue whirl. Xiao et. al identified the new flame regime by the lack of both visible soot and signs of turbulence. Further, Xiao et. al noted the difference in sound. Compared to the loud noise of the vigorously whirling fire whirl, the blue whirl was quiet.

2.2.1 Blue Whirl Flame Structure

Xiao et. al defined the blue whirl as a composition of two zones: a blue spinning flame at the base and a conical section at the top [2]. The flame description was further refined to consist of three regions. These three regions included: (1) the inverted blue cone at the base of the flame; (2) the vortex rim, identified by the bright blue rim region; and (3) the purple haze region atop the vortex rim. Figure 3 depicts these three regions. Of note is the position of the vortex rim. Because of its position above the inverted blue cone and off of the bottom boundary layer of the enclosure, this flame regime can be said to be a lifted flame.

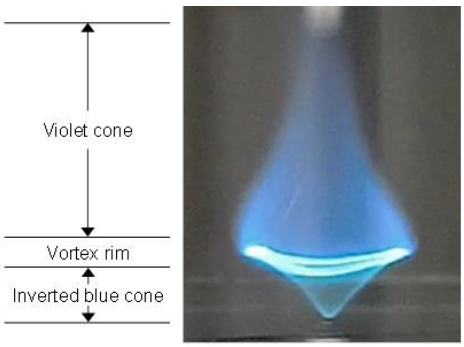

Figure 3: Blue whirl structure and shape.

It was hypothesized that the majority of the combustion reactions were occurring at the vortex rim due to its intense bright blue light compared to the other flame regions [2]. Hariharan et. al confirmed this hypothesis when capturing OH* chemiluminescent images. They found that the only flame region visible in the OH* spectroscopic region was the vortex rim, indicating predominant combustion reaction in that region [3].

Chung et. al studied the blue whirl through numerical simulation. Significant challenges were presented computationally such as the wide range of space and time scales involved. Further, simulating the blue whirl would require simulating a fire whirl subject to vortex breakdown, or finding a direct pathway to blue whirl formation and conditions [20], [21]. To attack the process, Chung et. al proceeded by: (1) developing the numerical method; and then (2) implementing the simulations to explore the effects of each control parameter. The process began by simulating vortex breakdown of nonreactive flows, resulting in the development of a low-Mach-number algorithm [22]. Chung et. al proceeded by developing a chemical-diffusion model (CDM) that reproduces features of both diffusion and premixed flames [23]. Once the

CDM was validated, Chung et. al simulated reactive vortex breakdown. Paired with the numerical model and general initial conditions used for n-heptane, the blue whirl was produced numerically. Chung et. al further defined the blue whirl as a composition of four flame types: (1) a premixed rich flame at the base; (2) a diffusion flame on top; (3) a premixed lean flame surrounding the top region; and (4) a triple flame at the vortex rim [20], [21]. Chung et. al also confirmed the hypothesis that the majority of combustion occurred at the vortex rim.

Carpio et. al also investigated the blue whirl's structure through numerical simulation [24]. Carpio et. al set out to refine the existing blue whirl model with the addition of a radiative heat transfer mechanism to the fuel source. Additionally, they considered the boundary layer surrounding the fuel pool that develops upon blue whirl formation. Simulations resulted in similar findings to that of [20], [21]. Streamline and reaction-rate plots concur with the tribrachial structure of the fuel-rich base interior, fuel lean top exterior, and diffusion flame on top, all meeting at the vortex ring to form the triple flame. The streamline plot also indicates a strong relationship between the recirculating bubble with downflow along the centerline of the vertical flow and the cone shape atop the flame; Carpio et. al hypothesize that the low velocity found inside the bubble enables the stabilization of the rich cone flame. Further, via the developed heat transfer model to the fuel pool, Carpio et. al determined that, due to the lifted flame's position high above the fuel pool, the fuel pool experiences heat loss via convective heat transfer. Radiative heat load from the

flame is thus the only heat transfer mechanism responsible for the fuel's transition from the liquid to gas phase.

2.2.2 Blue Whirl Flow Structure

The flow structure of the blue whirl closely resembles that of bubble mode vortex breakdown. Xiao et. al were first to make the comparison of the fire whirl and blue whirl to spiral and bubble mode vortices respectively [2]. Xiao et. al attribute increased residence time of the fuel due to vortex breakdown as the mechanism that lends the soot free nature of the flame. Hariharan et. al further postulated that the blue whirl obtains it shape from vortex breakdown because of the observation of luminous soot recirculation zones via high frame rate (HFR) imaging [3].

Hu et. al investigated the conditions for formation of the blue whirl flame regime. With the same two quartz half-shells suspended over a water surface, they were able to determine the required fuel supply rate for a given gap size S to observe blue whirl formation. Further, they were able to capture tangential air velocity at the inlet due to the buoyancy driven air entrainment. Measurements indicated a peak velocity at about 45 mm above the burning surface [25]. Hu et. al thought that the peak velocity at 45 mm above the water surface may correspond to the location of the vortex rim. Hu et. al also determined that the tangential velocity became constant after reaching a distance of about 100 mm above the water surface [25].

Hariharan et. al further investigated formation of the blue whirl through a scaling approach [26]. With previously measured experimental data, they sought to

understand the relationship between circulation, Γ, and buoyancy, measured by the heat release rate, $\dot{Q}$, in the burner. Each was non-dimensionalized. They used the ratio of the non-dimensionalized circulation and buoyancy terms to express the relative influence of circulation and buoyancy, hypothesizing that for blue whirl formation, the ratio R^*must be greater than one, or circulation dominated. They determined the blue whirl formed for R^* from 0.9-3.4, or more generally for $R^* > 1$. This agreed with their hypothesis that the blue whirl is a regime wherein circulation dominates local buoyancy. Further, they defined the transitional blue whirl as a regime where R^* is roughly 1, about where the effects of both circulation and buoyancy are equal. Finally, they found that the transition from the fire whirl to the blue whirl occurs at a threshold of R^* equal to 1, generating favorable conditions for a transition to a flow field dominated by circulation.

Coenen et. al setup a different experimental apparatus that consisted of a centrally located fuel port with twelve surrounding acrylic vanes. These vanes were offset 15.2 cm from the fuel port. In their experiments, they swept α, the inclination angle of the vanes with respect to the radial direction, to directly control ambient circulation. Coenen et. al found that larger radial pressure gradients accompanied higher values of α. At a value of α equal to seventy degrees, the previously formed fire whirl lengthened, and the resulting vigorous whirling motion led to bubble mode vortex breakdown, generating the blue whirl [27]. This finding echoes the results of Hu et. al and Hariharan et. al [3], [25]; a high enough radial pressure gradient and whirling flow are required for transition from the fire whirl to the blue whirl regime.

Chung et. al also presented the flow structure of the blue whirl as identified in their simulation [20], [21]. Of note is the revealed bubble mode vortex as hypothesized by Xiao et. al, Hu et. al, and Hariharan et. al [2], [3], [25]. The simulation locates the recirculation zones inside of the flame. Also of interest is that the recirculation zone lays just inside the visible vortex rim, identified by the bright blue light. In the inverted blue cone region, the simulation indicated high tangential velocity with a relatively narrow vortex core. Above the flame, the simulation showed accelerating flow in the z axis due to expansion of the hot gas.

2.2.3 Blue Whirl Exhaust Gas and Particulate Emissions

Anderson et. al investigated and compared emission characteristics of the blue whirl to fire whirls [28]. These comparisons were made for three fuels: (1) n-heptane; (2) n-octane; and (3) methyl acetate. The absence of NO_x and unburned hydrocarbons (UHCs) indicated that both flame regimes underwent near-complete combustion. Unsurprisingly, soot production for the fire whirl was almost three orders of magnitude larger than that of the blue whirl for the hydrocarbon fuels and about 400% more for methyl acetate. This finding reinforces Xiao et. al's hypothesis that longer residence times for the fuel may be driving the significantly lower soot production [2].

2.3 Vortex Breakdown

As discussed heavily in the literature surrounding the blue whirl, vortex breakdown, more specifically bubble mode vortex breakdown, is the main mechanism

that creates the soot free and stable nature of the flame. Vortical flows, however, are not unique to the blue whirl flame regime. They occur in nature and have been used in other combustion systems.

Vortex breakdown was initially discovered observing the effect of flow separation from leading edges of airplane wings with high inclination angles [29]. Research into vortex breakdown post discovery began to focus on vortex breakdown within tubes, yielding a much more controlled environment. Lucca-Negro et. al summarizes findings from [30]–[33]. Through experimentation with tubes, it became apparent that the vortex core size decreased as the Reynolds number, determined by the tube diameter, increased [34]. Further isolated and identified by Leibovich [35], this function is described as the ratio of tangential to axial velocity. This ratio is what leads to the formation of a downstream stagnation point and subsequently a recirculation zone along the vertical axis. Hall describes the critical angle of swirl, ∅, as the inverse tangent of the ratio of circumferential to axial velocity [36]. It was found that the angle ∅ upstream of breakdown is always greater than about 40 degrees. Hall also makes reference to the role of a positive or adverse pressure gradient along the axial direction. Sarpkaya's finding also reinforce Hall's findings that increased adverse pressure gradients lower the required swirl to form vortex breakdown [37].

As described by Sarpkaya's findings [38], the vortex breakdown type and location is dependent on the Reynolds number and circulation of the flow. Because

the blue whirl has been characterized as a bubble mode vortex, I will focus on vortex breakdown pertaining to bubble mode vortex breakdown.

2.3.1 Bubble Mode Vortex Breakdown

Brücker et. al presented results of particle tracking velocimetry (PTV) on vortex breakdown [39], [40]. They combined instantaneous PTV and volume scanning for low speed flows in a cylindrical tube. The flow was subjugated to introduction via guide vanes and an adverse pressure gradient, resulting in vortex breakdown. Key takeaways are the shape of the vortex. The bubble-mode vortex is axisymmetric, and the circumferential velocity profile can be represented by a Burgers vortex [41]. Further, the stagnation point was found to lie on the vortical axis, a defining characteristic for bubble-mode vortex breakdown. These characteristics agree with those as found by [38]. Filling of the bubble, discussed in [38], [39], was found to occur partly on the downstream end of the bubble, with emptying occurring upstream. Interestingly, in contrast to findings of Leibovich [35], Brücker found overall reversal flow inside of the bubble midplane. This flow reversal had a maximum negative axial velocity at the aft portion of the bubble and was found to be as large as the mean velocity [39].

2.3.2 Hysteresis of Vortex Breakdown

Of interest in regard to blue whirl formation is hysteresis. Thus far, the blue whirl has only been demonstrated to form transitioning from a fire whirl. This observation necessitates some background understanding of potential hysteresis

effects of vortex formation. Although not much literature exists surrounding hysteresis and vortex formation, two papers detail hysteresis effects regarding vortex formation analogous to flame regime transitions.

Horvath et. al present their findings on hysteresis of two dimensional vortex shedding for low Reynolds number flows [42]. They studied rapidly flowing soap film, formed between two vertically positioned nylon lines. These lines were 0.25 mm in diameter, positioned 6 cm apart, and ran the span of 45 cm vertically. Soap was fed into the experiment by a high precision metering valve. A rod, to perturb the fluid flow, was inserted between the nylon lines. $\bar{V}(t)$ and $V_x(t)$, measuring the mean flow speed and change in mean flow speed with respect to the x direction, were taken upstream and downstream of the rod respectively. Fluid velocity measurements were taken with a dual head laser Doppler velocimeter (LDV). Figure 4 depicts the experimental setup used in [42].

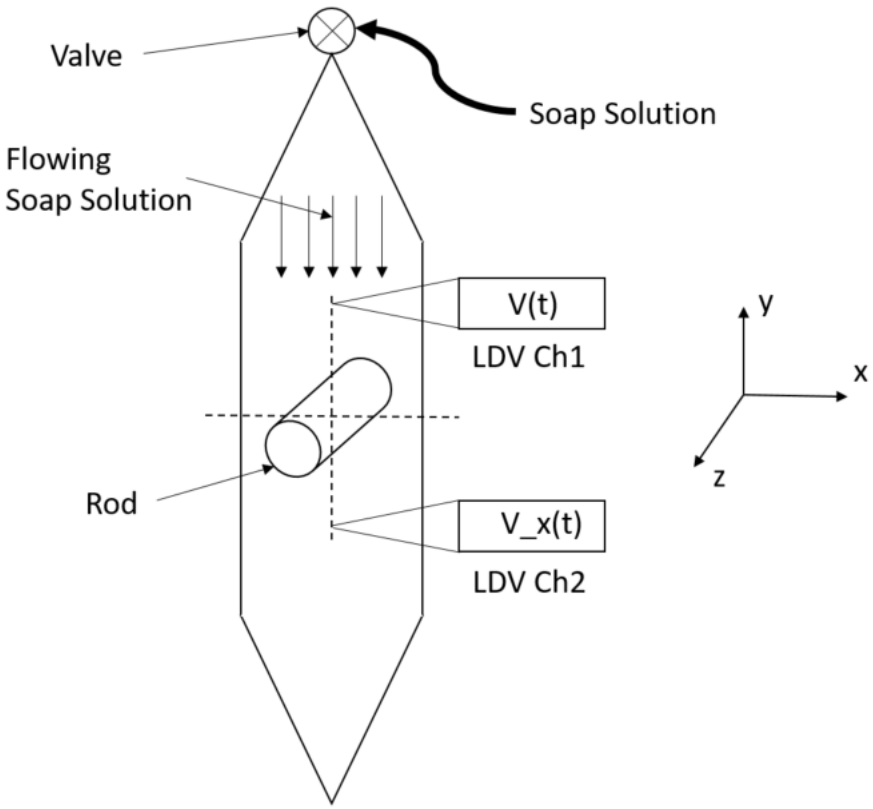

Figure 4: Experimental setup of Horvath et. al [42]

In these experiments, there is a critical flow at which the flow shifts from the laminar flow (LF) state to the vortex shedding (VS) state. Horvath et. al performed experiments to verify this critical velocity, named V_c. First, at a velocity such that the system was in the LF state, they increased flow of the fluid and observed a transition from LF to VS. The critical velocity for this transition is V_c^{up}. Then, at a velocity such that the fluid was in the VS state, they decreased flow of the fluid and observed a transition from VS to LF. The critical velocity for this transition is V_c^{down}. Results indicated a 14% difference between V_c^{up} and V_c^{down}, indicating hysteresis in the transition of the fluid flow state.

Horvath et. al acknowledge that this finding is surprising and contradictory to the expected system response. Further, they acknowledge that the mechanism for hysteresis in the system is still unclear. Although they have eliminated several potential factors, a theoretical explanation for the experimental findings is still needed.

Tummers et. al present their work on the study of swirl effects on turbulent transport, mixing, and chemical reaction in two flame states, a “blue” flame state, and a “yellow” flame state, at identical controlling parameters (equivalence ratio and rotation rate) [43]. To form each regime, the burner, depicted in Figure 5, was set to an arbitrary flow rate, either higher or lower corresponding to blue and yellow flame respectively. Formation of the blue flame occurred as the flow rate was decreased. Conversely, the formation of the yellow flame occurred as the flow rate was increased. The swirling air was controlled via a rotating pipe that surrounded the flowing air. Due to viscous shear stresses, the pipe’s rotation forced air to the desired swirl upon exit of the pipe. Further information regarding the burner configuration can be found in [44].

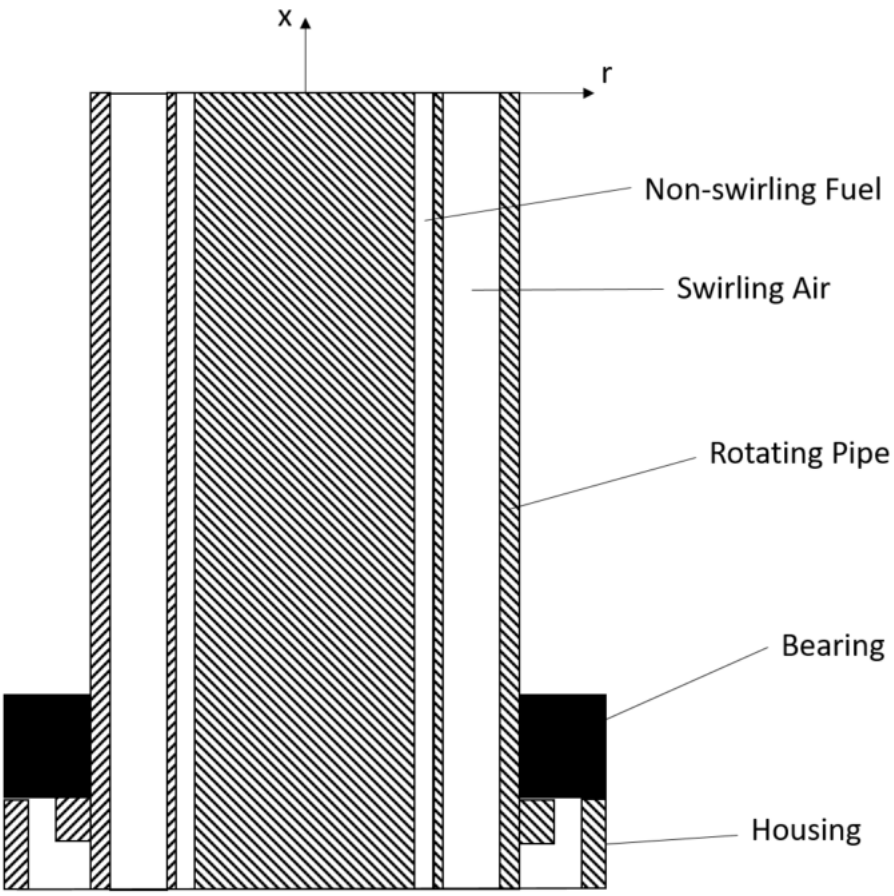

Figure 5: Experimental setup of Tummers et. al [43]

Three measurement techniques were implemented: (1) Particle image velocimetry (PIV); (2) Laser induced fluorescence; and (3) Coherent anti-Stokes Raman spectroscopy. Key findings by Tummers et. al in regards to the blue whirl lie in the hysteresis found when transitioning between the two flame regimes. At a fixed equivalence ratio of $\emptyset = 0.83$, the rotation rate was varied simultaneously to the air and fuel flow rates. Tummers et. al found that in the upwards transition from a yellow flame to a blue flame requires about twice as much rotation than that of the reverse transition from a blue flame to a yellow flame. Tummers et. al attribute the hysteresis

mechanism to the dynamic velocity field and thermal characteristics of each respective flame regime. For example, significantly improved mixing between the fuel and air can be seen for the blue flame structure. Even as the flow rate decreases, if the flame is that of the blue flame, the strong recirculation and backflow maintains the improved mixing of fuel and oxidizer, promoting and retaining the recirculation zone critical to the blue flame's structure. Similarly, when trying to transition from the yellow to blue flame, until the circulation is high enough, sufficient mixing between fuel and air is not present in the absence of the recirculation zone. Because of the inherent difficulty in measuring these flame characteristics, Tummers et. al suggest that further insight into the mechanisms causing hysteresis may be found through numerical simulation.

Chapter 3: Experimental Methods

This chapter addresses the design of the experimental apparatus, methods, procedures, and analysis employed for the study.

3.1 Design of Experimental Apparatus

To address our research question, we needed to shift away from the buoyancy induced flow incorporated in the quartz half-shell design and move to a system that utilized forced air induction. The need to move away from buoyancy induced flow comes from the requirement of variable circumferential flow profiles. Forced induction provides the most repeatable and consistent method for air flow delivery to the flame.

In designing an advanced experimental burner for the blue whirl, required criteria were set to ensure the burner would perform adequately for research purposes. Some of these requirements, i.e. adjustable burner geometry, were not set for completion for this study, rather to allow for completion of other studies of interest in the future. The requirements came from a list of independent variables. The list of independent variables of interest included the following:

- Fuel type
- Fuel Flow Rate
- Burner Size
- Radial Flowrate
- Circumferential Flowrate

- Circumferential Flow Profile
- Baseplate Temperature
- Air Temperature

Fuel type and fuel flowrate are required to test the impact of chemical kinetics on blue whirl formation and stability. These requirements necessitated a fuel system that was capable of running a wide range of fuels at a wide range of fuel flow rates.

An adjustable burner geometry, incorporating a variable burner height and diameter, allows for studies that seek to understand the impact of different boundary conditions on the flow field. Lower burner heights and smaller burner diameters create more significant pressure gradients along the radial and z axis respectively. Both variables remain untested and unstudied.

Independent control over tangential and radial flow was essential for the advanced burner. Anderson et. al and Chung et. al both determined the radial flow component to be key for generating the soot free, lifted flame that defines the blue whirl [20], [28]. Additionally, Anderson et. al identified a “sweet spot” in the ratio of the quartz gap size and height above surface. With independent control over each flow, radial flow can be introduced to any given circumferential flow, and an optimal stability point can be measured. Further added to flowrate is flow profile. Testing of the circumferential flow profile will lend insight into blue whirl sensitivity to local regions of high air flow. These profiles may also produce results that glean a critical height of flow to which the blue whirl is sensitive.

Temperature control was the last requirement to be set. We sought temperature control over both the burning surface and the incoming air. Temperature control over the burning surface was a requirement noted for implementing an aluminum plate instead of water [28]. It is hypothesized that the temperature regulated plate prevents local hot spots from developing, creating non-uniform fuel evaporation of the fuel puddle, destabilizing the flame. Further, an increased plate and air temperature will be needed for ignition of higher chained hydrocarbons. Fuels with high activation energies will not be ignitable under ambient temperature and pressure conditions. Heating the incoming air will aid in ignition. Heated air also serves to add any real world testing of the combustion system. Most commercial combustions systems utilize some form of exhaust gas recirculation (EGR), and consume oxidizers at elevated temperatures as the exhaust gas mixes with the fresh charge.

The dependent variable of interest is flame stability. Having selected image analysis as the primary means of determining flame regimes, plentiful optical access was required. Easy optical access, although a challenging feature to incorporate, was a requirement to ensure that a wide range of measurement techniques could be implemented. This requirement is more comprehensive than a simple viewing window. The burner needed to be readily accessible for lasers and imaging devices, as well as the burner operator. Relevant measurements considered in the design included: chemiluminescence; planar laser induced fluorescence (PLIF), general flame imaging; and particle image velocimetry (PIV) to name a few.

3.1.1 Advanced Burner Structure

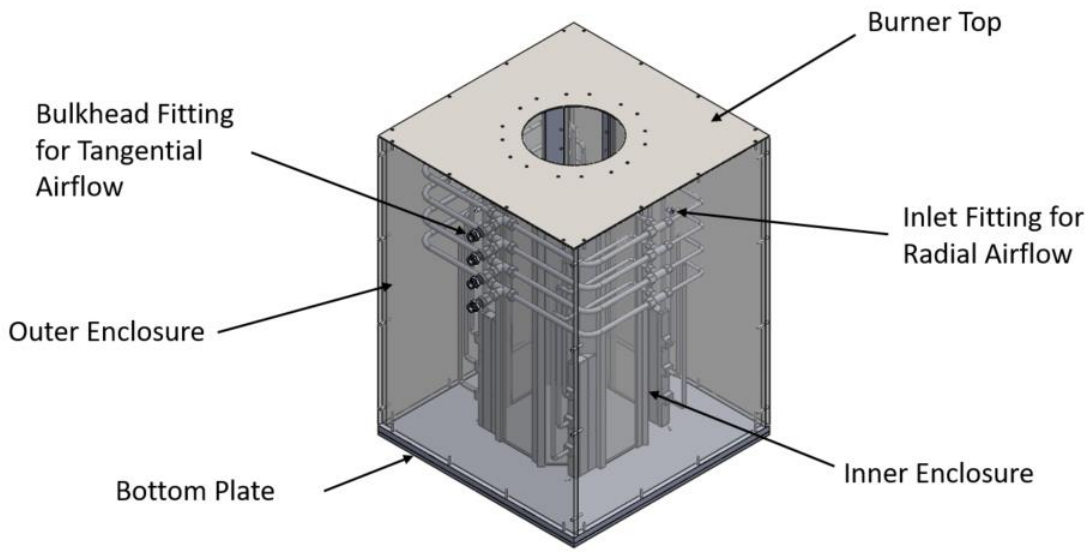

Figure 6: Isometric view of the advanced burner.

The final advanced experimental burner design, depicted in Figure 6 incorporates an inner octagonal enclosure, built with machined 6061 aluminum frames and quartz glass, and an outer square enclosure, built with 6061 aluminum plates for the top and bottom, and acrylic comprising the outer enclosure walls.

There are several strengths to this design. With a plenum created between the two enclosures, air can be supplied radially through a gap on the bottom of each wall of the octagon. At a uniform pressure in the plenum, air flow will be distributed evenly to each gap without the need for nozzles, which are opaque and would interfere with laser diagnostic measurements. The viewing windows on the inner enclosure are also parallel to the external acrylic walls comprising the outer enclosure (See Figure 9 - *PIV exhaust in place*). Further, when reducing or increasing the inner enclosure diameter, the flow setup is able to remain the same. Figure 7

demonstrates how the inner closure can shrink and expand similar to the iris of a camera. Air is easily delivered to the circumferential airflow straighteners via bulkhead connectors in the acrylic. Hardline takes air to either side of the burner where it meets T-unions. These T-unions deliver air to two flow straighteners.

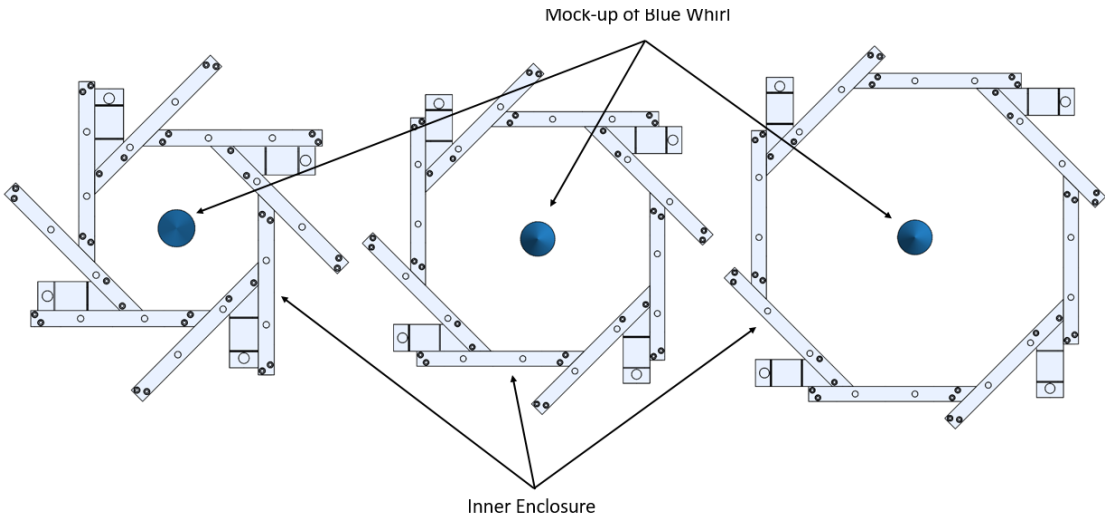

Figure 7: The inner enclosure acts as a camera eye, shrinking and expanding to change the burner diameter.

The burner stands at 30” tall with an inner diameter of about 12” at its larges configuration. These dimensions were selected to ensure replicability to the quartz half-shell design. The inner diameter can be reduced to about 6” before the circumferential flow inlets begin to impede flame visibility. The inner quartz viewing windows are 3.75” x 29.9” and 4.6” x 29.9”, and provide plenty of visibility to the flame.

3.1.2 Burning Surface and Burner Top

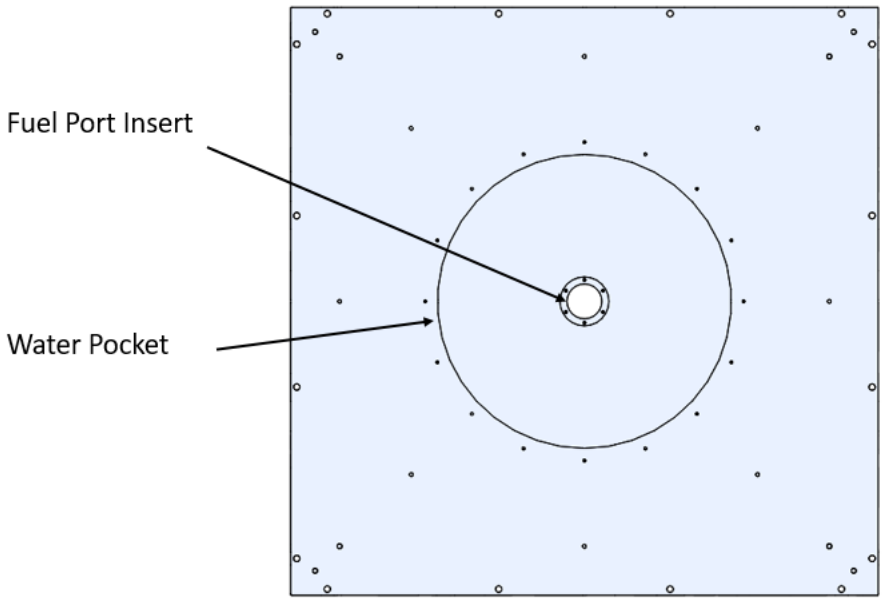

Figure 8: Burning surface plate with machined water pocket and fuel port insert.

The burning surface was manufactured from two plates: a 5/8” thick top plate; and a ¼” thick bottom plate, both 24” by 24”. The burning surface temperature is controlled by circulating water that is heated or cooled by a chiller. A pocket, machined into the 5/8” thick top plate, allows for the circulating water to create an even temperature distribution on the burning surface. This method allows for heating and cooling of the fuel but, more importantly, prevents local hot spots from evaporating fuel at a higher rate than in other locations. To seal the pocket, a bead of Red Permatex RTV Gasket Maker is laid down around the pocket and around the inner bore for the fuel port. The plates are held together with ¼”-20 and 10-32 fasteners. The bottom plate is also tapped to allow standoffs to be threaded in,

creating room for a fuel port and fuel line to thread in between the optic mounting table and the burner.

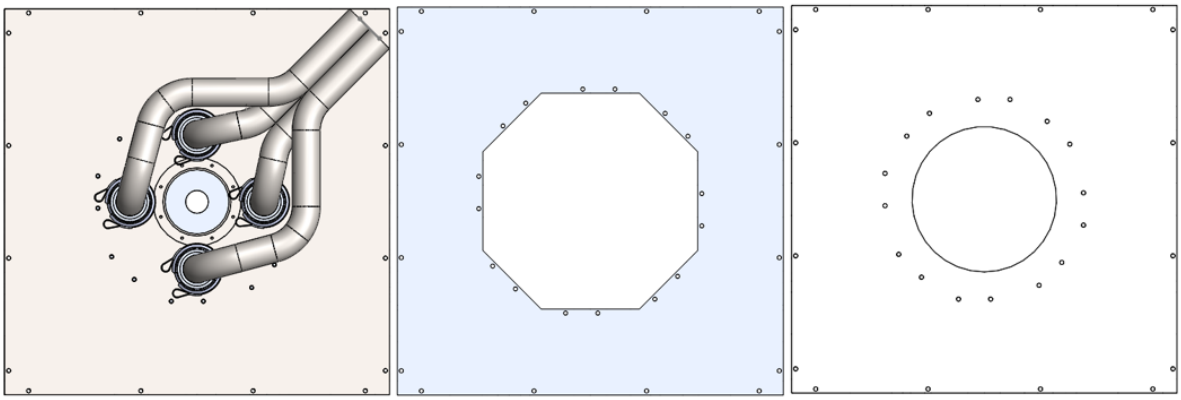

Figure 9: Three different top configurations for the advanced burner. From left to right: optical access port for top down imaging; hexagonal cutaway for plate insert, imposing upper boundary layer; and a circular vent to enable exhaust venting to atmosphere (replicates preliminary blue whirl apparatus).

Several burner tops have been designed. Depicted in Figure 9, from left to right, they are for PIV imaging, imposing an internal pressure gradient along the z axis, and running with an open exhaust configuration respectively. Because stereo PIV is not accessible with this burner (cannot orient two cameras 60 degrees offset from a laser plane), a view port with routed exhaust runners was designed to allow for top down imaging. With a laser plane oriented parallel to the XY plane, a camera can capture particle velocity looking down the Z axis. Super imposing images from the XY and YZ planes would produce a representative 3D velocity field. The other burner top method involves placing a plate inside of the inner Octagon. Doing so effectively modulates the height of the combustion chamber from its maximum of 30”, all the way down to 6”. This system broadens the potential for laser diagnostics and allots a wide range of geometric burner configurations. For burner operation

without an imposed top, the right most top depicted in Figure 9 retains the inner enclosure walls and vents to atmosphere.

3.1.3 Air Injection

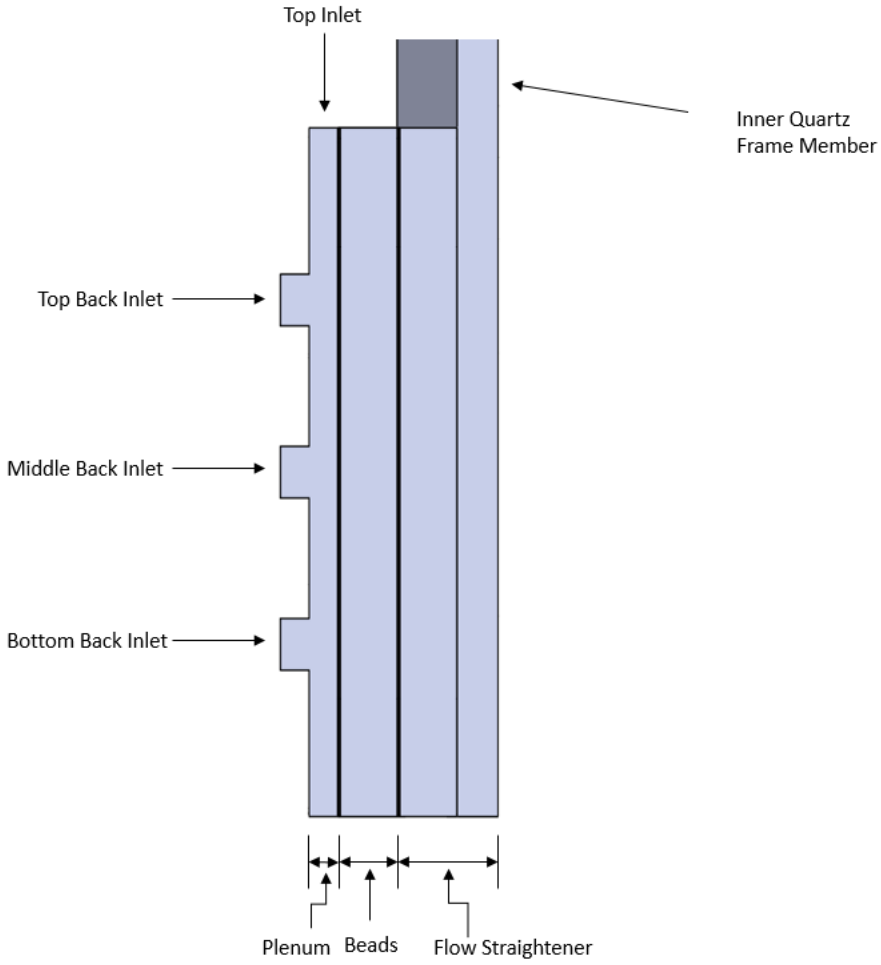

Figure 10: Diagram of circumferential airflow straightener system.

The circumferential airflow system is constructed of three sections: a rear plenum; a middle beaded section; and a forward air flow straightener. Each section is

separated with a mesh screen to retain the beads. These three sections ensure that air is supplied uniformly, diffused properly, and straightened before entering the inner enclosure. If flow profile adjustments are desired, four ports with independently controlled flow rates allow for finite incremental changes. Figure 11, depicting a cutaway and top down view of the burner, shows how air is introduced into the inner enclosure. For both the radial and tangential air inlet systems, compressed air, regulated by air flow controllers (Alicat MCR-2000SLPM), feed a small manifold.

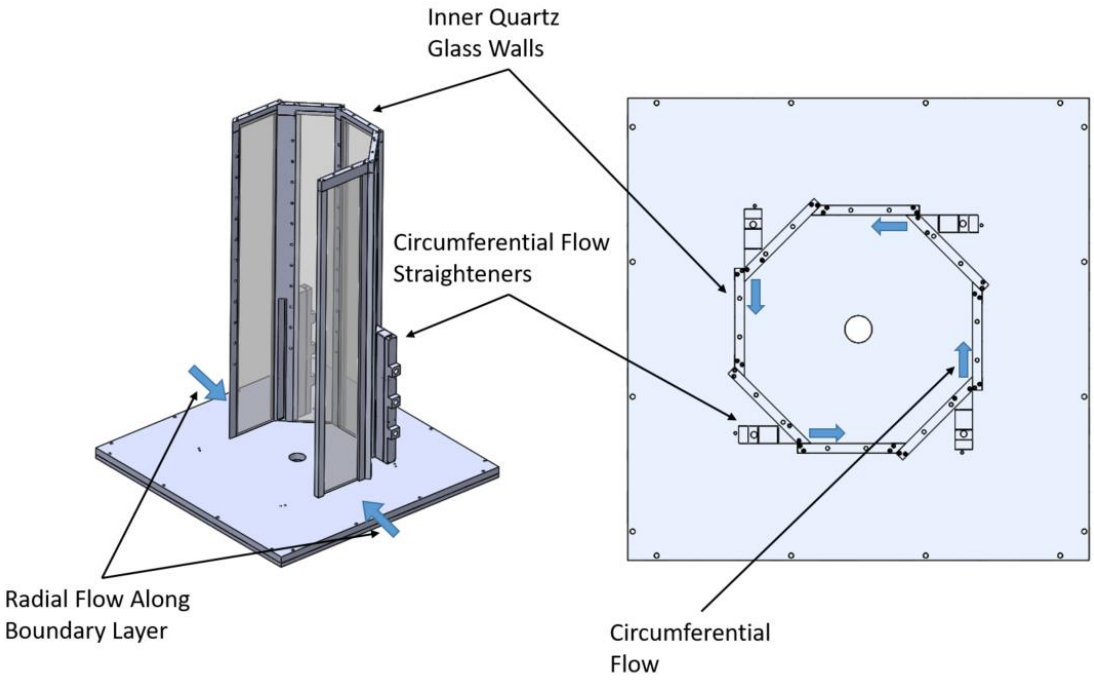

Figure 11: Cutaways of the advanced burner. Labeled are critical components to the airflow delivery mechanisms.

Radial air flow is delivered from the plenum created between the inner enclosure and outer enclosure. ¼" NPT fittings, threaded into the outer acrylic walls,

feed air to the plenum. The air, at a uniform pressure, is then pushed between a 3 mm gap between the bottom of the inner enclosure and the bottom boundary layer of the flow. Again, this air flow delivery method prevents optical obstruction by hardware. The entire flame is visible from a horizontal view.

3.1.4 Fuel Delivery

Fuel is pumped to the burning surface with a positive displacement pump (Vici M60LHS) through a threaded port. The fuel port is center drilled and tapped to accommodate a ¼" NPT fitting, allowing fuel to pass through the port, and lathed and threaded externally to secure the port to the bottom plate. Coupled with fuel resistant Teflon tape, these threads also prevent fuel from leaking between the two components. Because the port is threaded into the bottom plate instead of being machined in, different fuel port outlet sizes can be swapped in. Further, non-traditional ports, such as an annulus, can also be experimented with.

3.2 Flow Profiles

To measure the effect of the circumferential flow profile on blue whirl stability, three flow profiles were proposed. Depicted in Figure 12, Figure 13, and Figure 14, the profiles introduce large amounts of air at the bottom, middle, and top of the circumferential flow straighteners respectively. These profiles were selected based on buoyancy induced inlet airflow profiles measured by Hu et. al [25]. They observed a parabolic hump at the bottom, near the flame, and a flat, uniform flow, at higher z-axis positions. This profile is akin to that of the profile depicted in Figure 12.

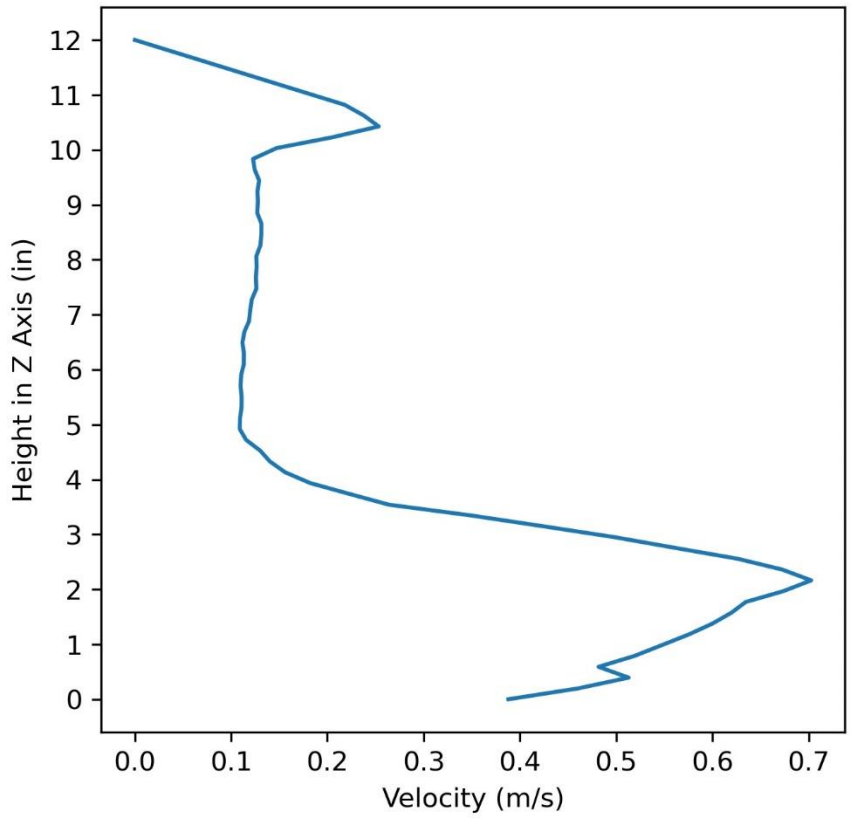

Figure 12: Flow profile for bottom port configuration.

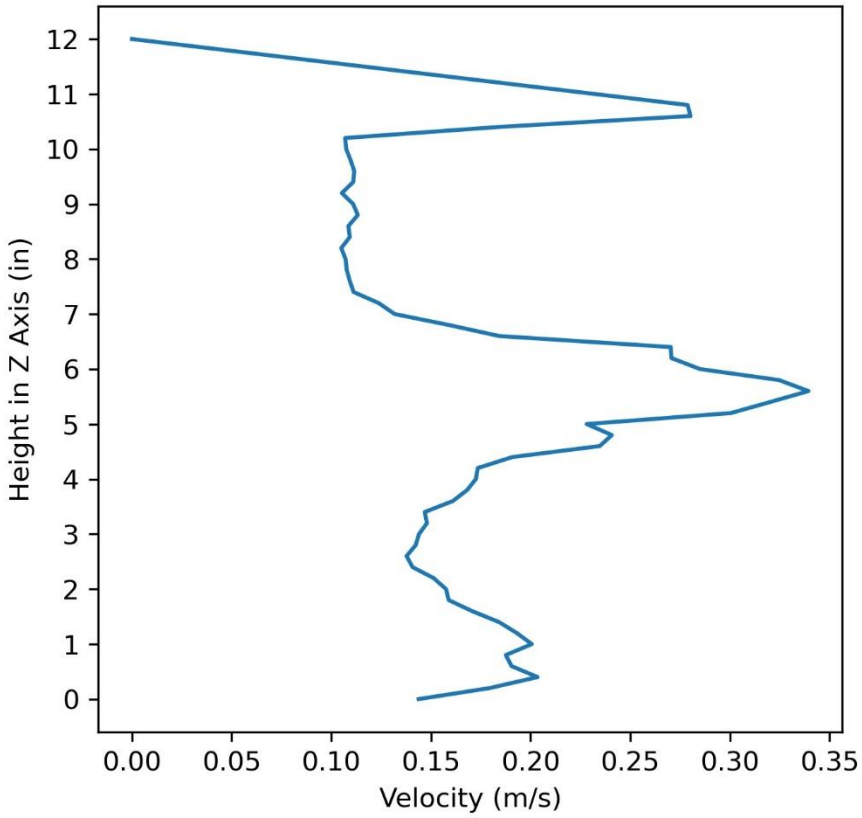

Figure 13: Flow profile for middle port configuration.

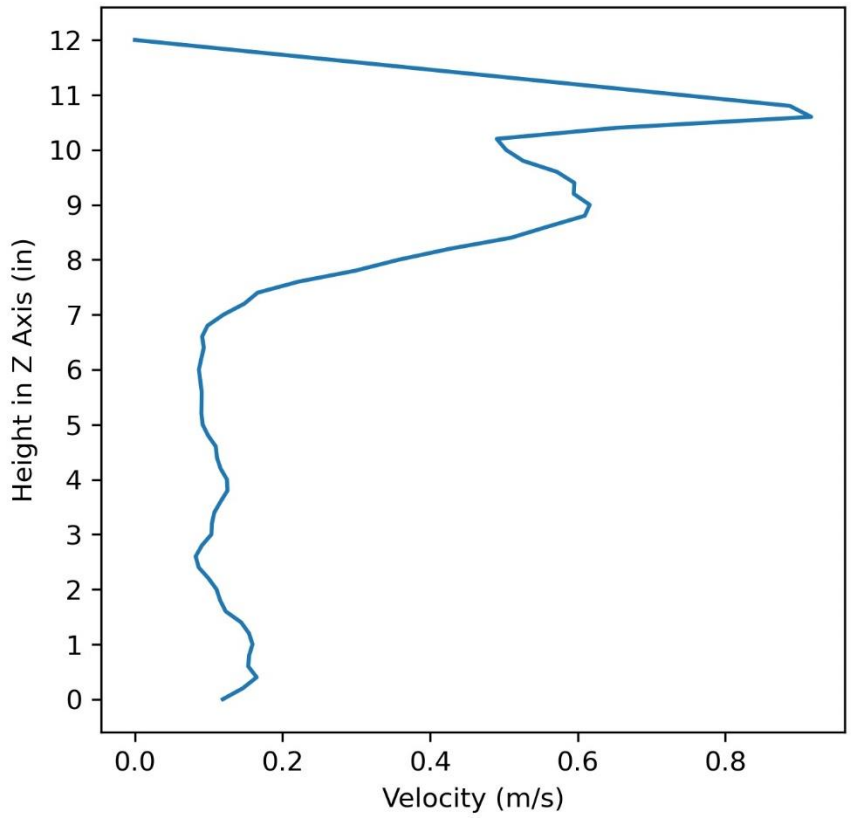

Figure 14: Flow profile for top port configuration

In order to measure these circumferential flow profiles, an external test rig was required because of the inaccessibility of the circumferential flow straighteners internal to the burner. A diagram of the air delivery system for the circumferential airflow can be seen in Figure 15. Switching air between the burner and test rig is done by moving the position of the three-way ball valves. Adjusting the percentage of flow through each port, similarly, is done by adjusting the opening of the inline needle valve. Measurements at the test rig, depicted side on in Figure 16, were taken with a hot wire anemometer probe (DantecMini CTA) translated vertically using a motor-driven linear translation stage constructed in-house. The probe was offset 25 mm

from the surface of the flow straightener. The motor was set to a speed that translates the 12” of the flow straightener in about 1 min. The output of the measurement is a representative velocity profile for the given conditions.

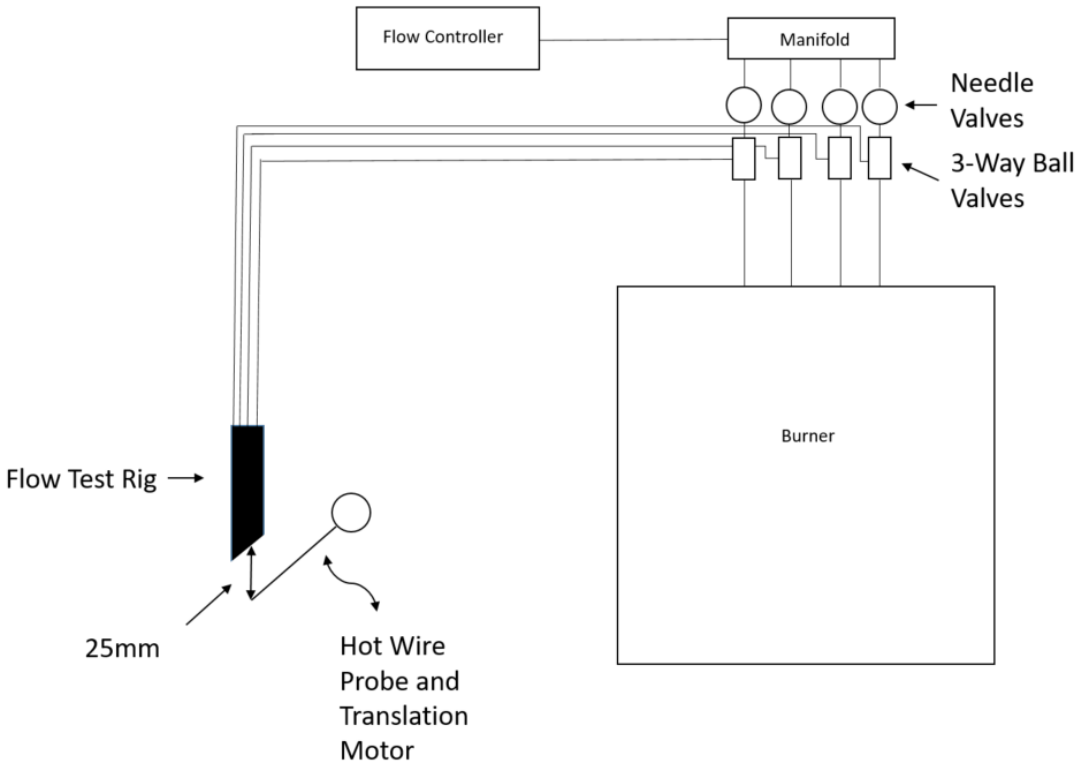

Figure 15: Diagram of the airflow delivery system for the advanced burner, including the flow profile measurement apparatus.

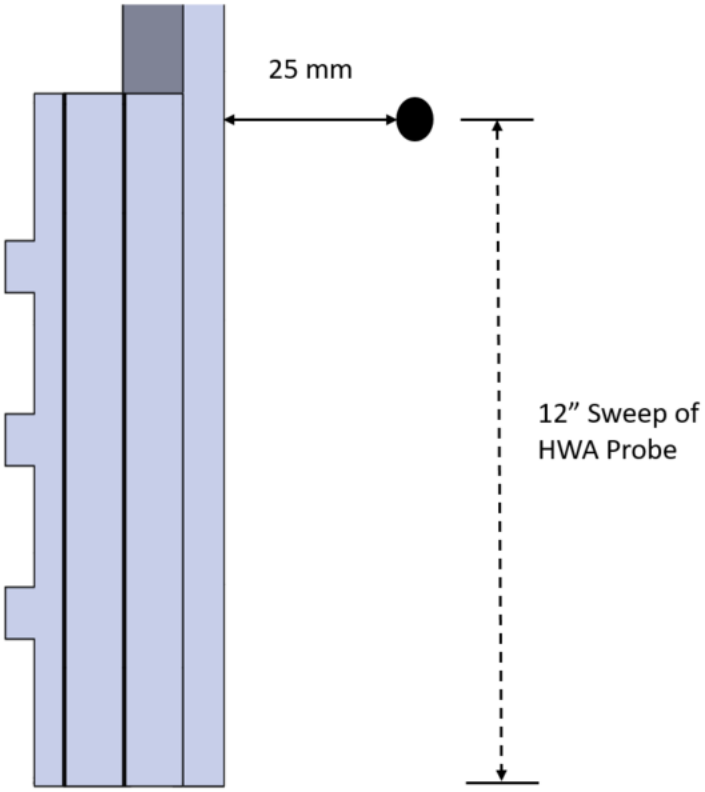

Figure 16: Diagram of circumferential flow profile measurement setup. The HWA probe, positioned 25mm off of the surface of the circumferential airflow straightener, is translated the length of the flow straightener to obtain the velocity profile.

3.3 Image Capture and Analysis

Video images were used to quantify blue whirl flame stability. The camera (Fastec IL5SC81TBD) was positioned perpendicular to the outer enclosure wall so that it had an unobstructed view to the flame. To focus the camera, a screw was placed central to the fuel port (depicted in Figure 17). When focused, this allowed for a resolution of 3.845 px/mm at the depth of the flame. The gain, frame rate, aspect ratio, and shutter speed were set to 1.0, 24, 800x450, and 20000 respectively.

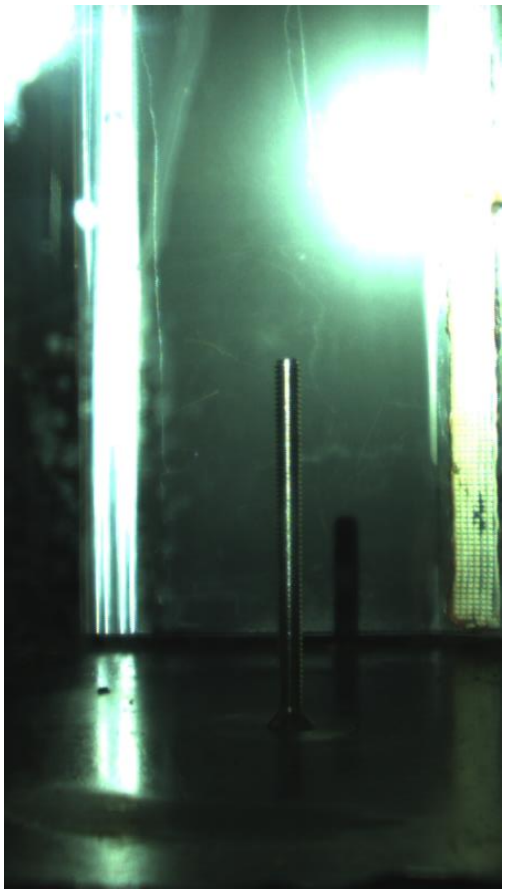

Figure 17: Image capture of a 1/4"-20 screw at the center of the burner for camera focusing and distance calibration.

Each condition was recorded for a total of 120s, allowing the flame to reach steady or quasi-steady state. When recording was complete, the video frames were exported as jpeg images and stored in a labeled folder for post-processing. The images were post-processed by:

1) Reading in the raw image
2) Cropping the image to the desired region of interest and identifying the vertical location of the burning surface in the image

    a. Capturing the average red channel intensity of the image for soot calculation

3) Masking the image, in grayscale, with a lower and upper bound
4) Running a canny edge detection algorithm
5) Dilating the canny edges to ensure continuity of edges
6) Drawing a bounding box around the longest continuous edge and evaluating flame shape and position.

Capturing the red channel average intensity of the unprocessed image provides a relative metric for comparing soot production between images. Although the intensity values are not calibrated to real soot production, they provide a method for determining what conditions produce more soot. A step by step example of image analysis is shown in Figure 18.

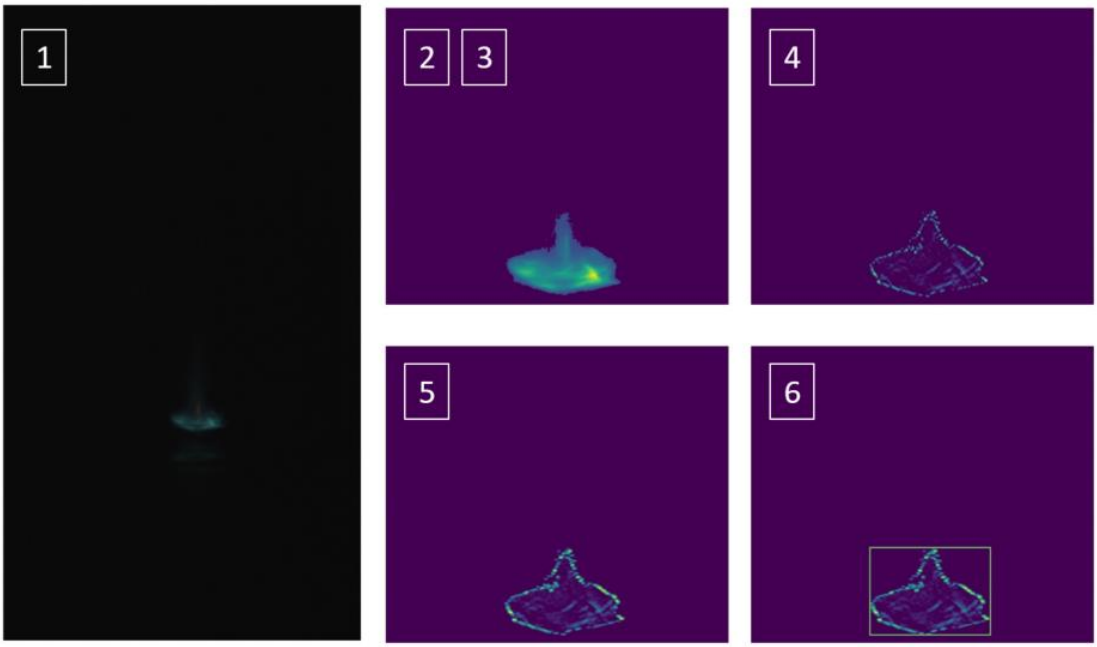

Figure 18: Example images of post processing steps for image analysis. The images correspond to the following image states: (1) Raw image; (2, 3) Cropped and grayscale; (4) Canny edge detection; (5) Dilated canny edge detection; and (6) Bounded canny edges.

The meat of the image analysis, however, comes from the mask, canny edge detection, and bounding box. The mask serves to remove any low level light intensity from around the flame. It reduces slight reflections from the background and burning surface and cleans up the base of the flame. Further, it attenuates extremely bright regions, say from a sooting flame, that may create too much noise for the edge detection. Once masked, a canny edge detection is applied and dilated. The dilation ensures that regions that may have been disconnected are rejoined, keeping the flame shape whole. Lastly, a bounding box encapsulates the entirety of the edge detection, capturing the flame. Since the signature characteristic of a blue whirl flame is its lifted blue rim [2], the location of the bounding box is the key metric for detecting images with blue whirls. If the bounding box extends to the burning surface, then the

flame is not lifted and is therefore not labeled a blue whirl. Conversely, if the bounding box does not extend to the burning surface, the flame is not labeled a blue whirl. Figure 19 depicts a typical transition from a sooting transition whirl to a blue whirl. Note the bounding box's lower position. It's not until the flame becomes fully lifted that the bounding box leaves the bottom index of the image, indicating the presence of a blue whirl.

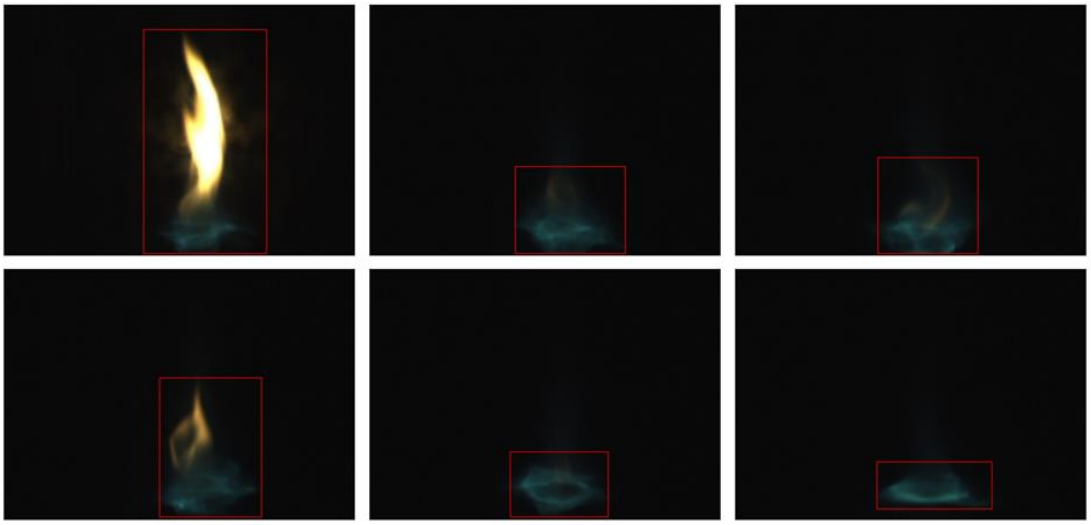

Figure 19: Transition from a sooting transition whirl (top left) to a blue whirl (bottom right). The bottom location of the bounding box determines the flame type observed (blue whirl or non-blue whirl).

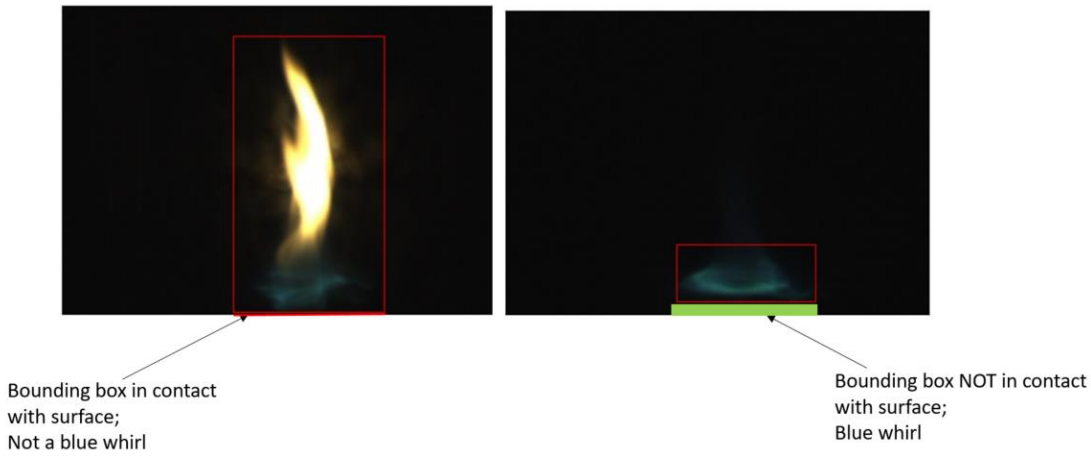

Figure 20: Note the change in location of the bounding box compared to the left and right frame. In the left frame, the bounding box is still incident with the bottom of the image. In the right frame, the bounding box has risen above the bottom of the image. This space or rise is denoted by the green rectangle. It is this space, defining the "lifted flame criteria," that the post processor keys off of to determine if a blue whirl is present in the frame of interest.

For this post processing method to be effective, the optimal mask values need to be determined via a test script. The mask values are determined by casting in a set of images that have a known flame type (blue whirl or not). For each image, the test script will run a pair of lower and upper limit mask values and compare the predicted flame type with the training set. The score for each set of mask values is calculated by an accuracy measurement. Both a raw accuracy score and a weighted accuracy score, biased to eliminate false positives, are recorded.

3.4 Procedure

To begin experimentation, the chiller controlling plate temperature is powered on and allowed to circulate water long enough to reach a uniform plate temperature. The fuel system is primed by pumping fuel through the fuel port until air bubbles are no longer visible in the line. If a different fuel is being tested, air bubbles are

intentionally introduced to ensure that the previous fuel has been entirely pushed through the system. The air flow system, both circumferential and radial, is checked and verified to be operational. Further, the ball and needle valves are checked to ensure they are in the proper configuration. A fuel program is run, set to pump 0.5 mL of fuel to the burning surface, pause for 2 s, and then continue pumping at the desired steady state fuel flow rate. The fuel is ignited manually with a butane lighter during the fuel program's pause. Once ignition has occurred, air flow is introduced.

To capture image data, the camera is armed, displaying live images the camera's aperture is seeing. Once the flow rates have been set to the first condition of interest in the flowrate sweep and the flame has reached steady-state, the camera is triggered. The camera is triggered off once the time window reaches 120 s. This process is repeated until flame extinction or until all values in the sweep of airflow rates have been tested. Then fuel and airflow are cut and the camera is triggered off.

Chapter 4: Results

4.1 Effect of Circumferential Flow Profile on Flame Stability and Soot Production

To measure the impact of circumferential flow profile on flame stability, three profiles of interest were tested. These profiles are depicted in Figure 12, Figure 13, and Figure 14. Each profile is generated by injecting air at one of three ports: the uppermost along the back side of the plenum (back-top); the middle port along the back side of the plenum (back-mid); and the bottommost along the back side of the plenum (back-bot). These profiles entrain air with local concentrations along varying locations in the z axis.

For each profile of interest, an upper and lower limit circumferential flowrate were determined to create the sweep range. This range was established in order to capture meaningful change in blue whirl behavior and eliminate excessive data collection where minimal changes to flame stability or soot production would be observed. These limits were determined by visual inspection. When the flame exhibited soot production in the purple haze region and no longer stayed in a continuous lifted state, the upper limit was determined to have been reached. Similarly, when the flame transitioned from a whirling flame to a transitional state between pool fire and fire whirl, the lower limit was determined to have been reached.

Upper and lower limits were also determined for the range of radial flowrates. Zero, the natural lower limit, was set to examine system performance when the only

air being entrained was tangential air flow. The upper limit of 75 slpm was determined because, once past 75 slpm, no significant system changes were observed. For each flow configuration, 100-110 slpm of radial flow made the system unstable.

Each flow condition was tested for 120 s and images were sampled at a framerate of 24 hz. The entrained air temperature for the radial and circumferential air flow was that of ambient, nominally 25 ˚C. The plate temperature was fixed at 25 ˚C.

Once all images were captured and stored, they were post-processed according to the procedure detailed in section 3.3. The outputs of the post-processor are 2D plots, depicting flame stability for a given radial flowrate and range of circumferential flowrates, in addition to 2.5D contour plots, depicting flame stability and soot production for the entire range of radial and circumferential flowrates. Figure 228 - 23show the 2.5D contour plots for the stability and soot production of n-heptane.

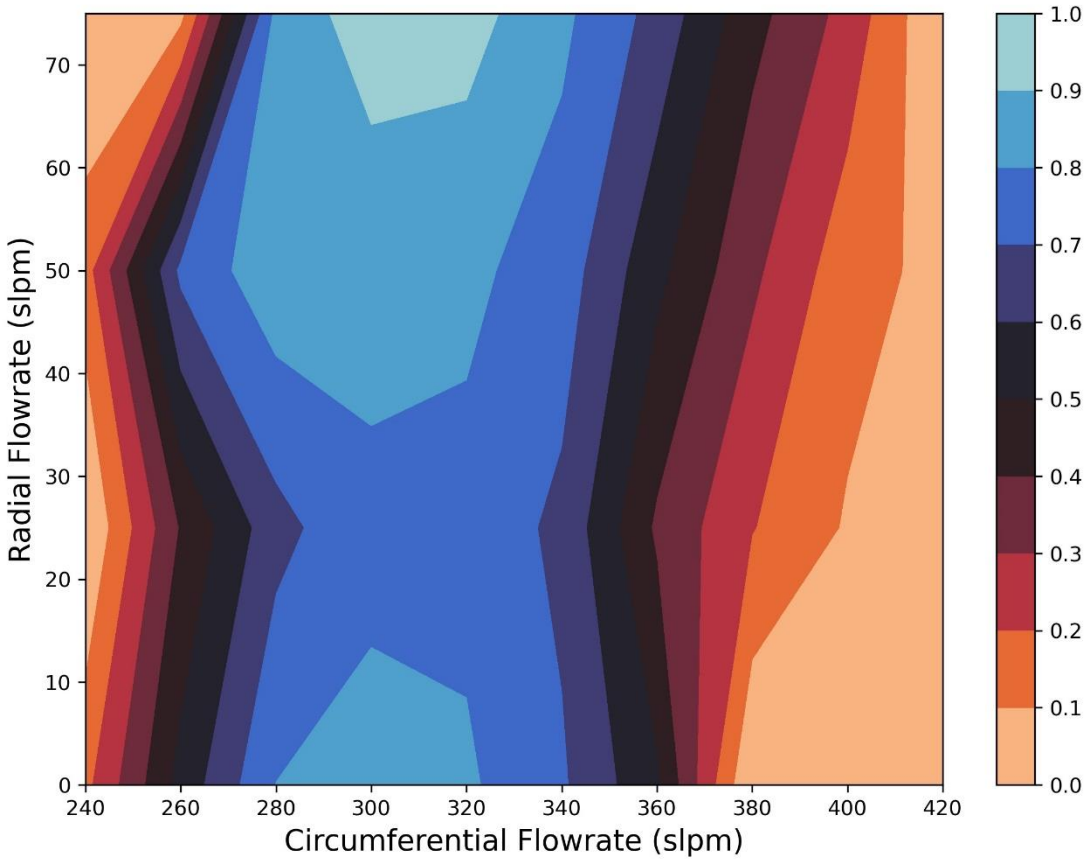

Figure 21: Flame stability of n-heptane for bottom flow profile configuration as a function of radial and circumferential flowrate.

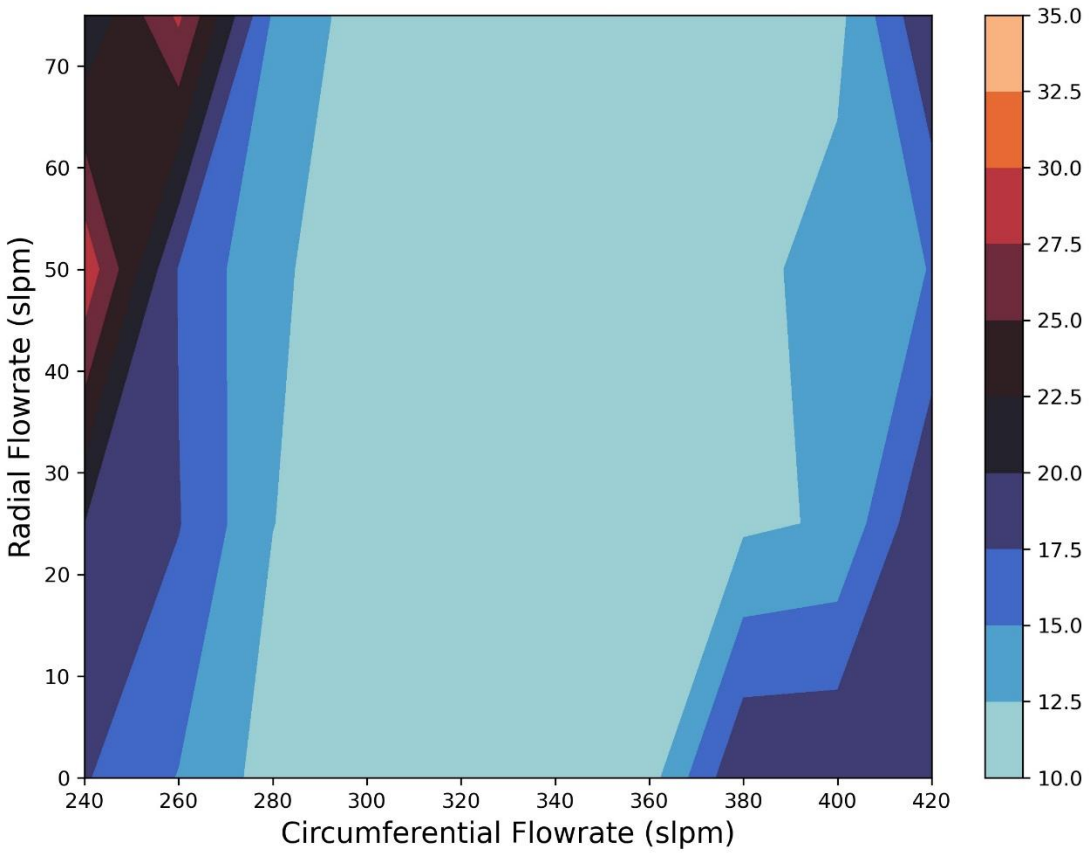

Figure 22: Soot production of n-heptane for bottom flow profile configuration as a function of radial and circumferential flowrate.

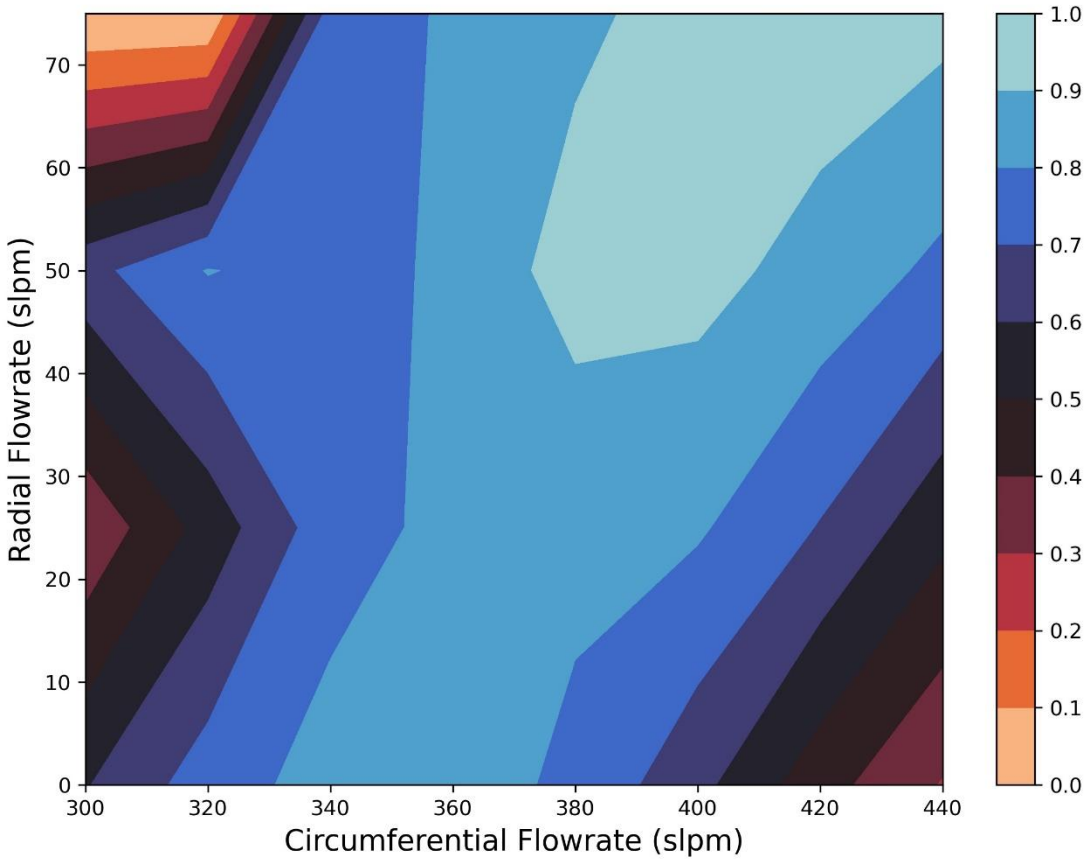

Figure 23: Flame stability of n-heptane for middle flow profile configuration as a function of radial and circumferential flowrate.

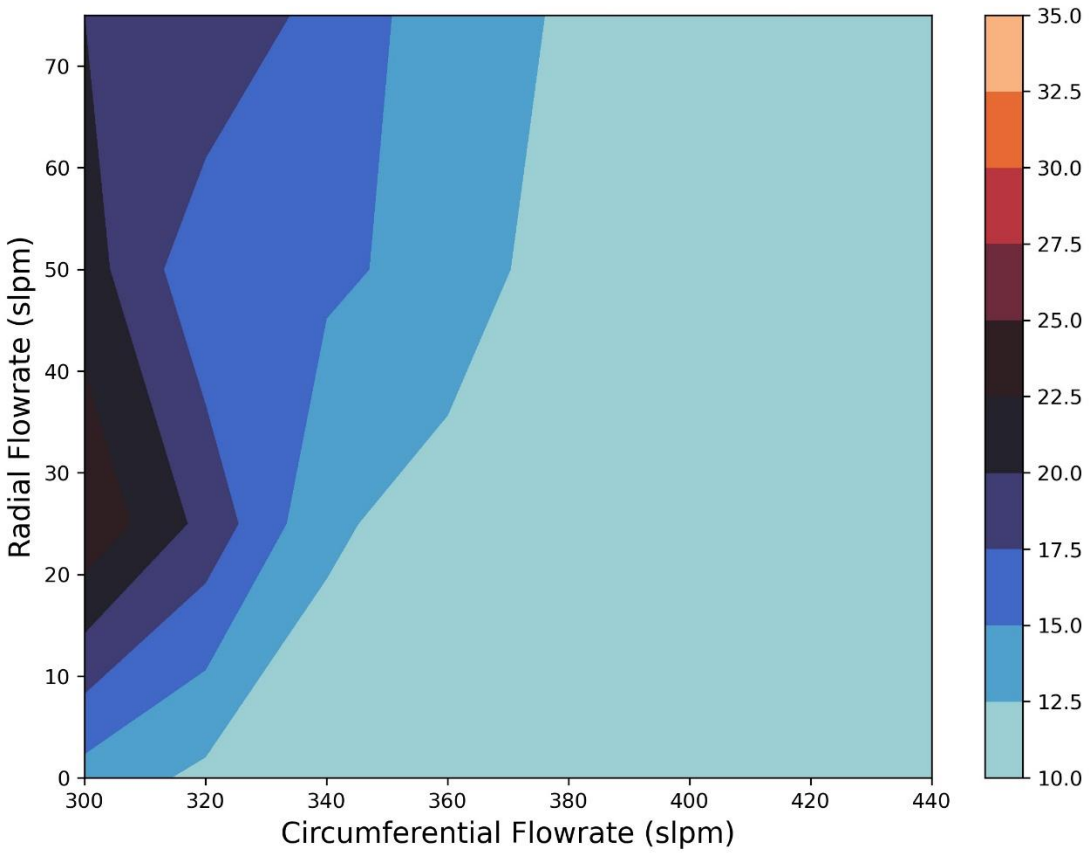

Figure 24: Soot production of n-heptane for middle flow profile configuration as a function of radial and circumferential flowrate.

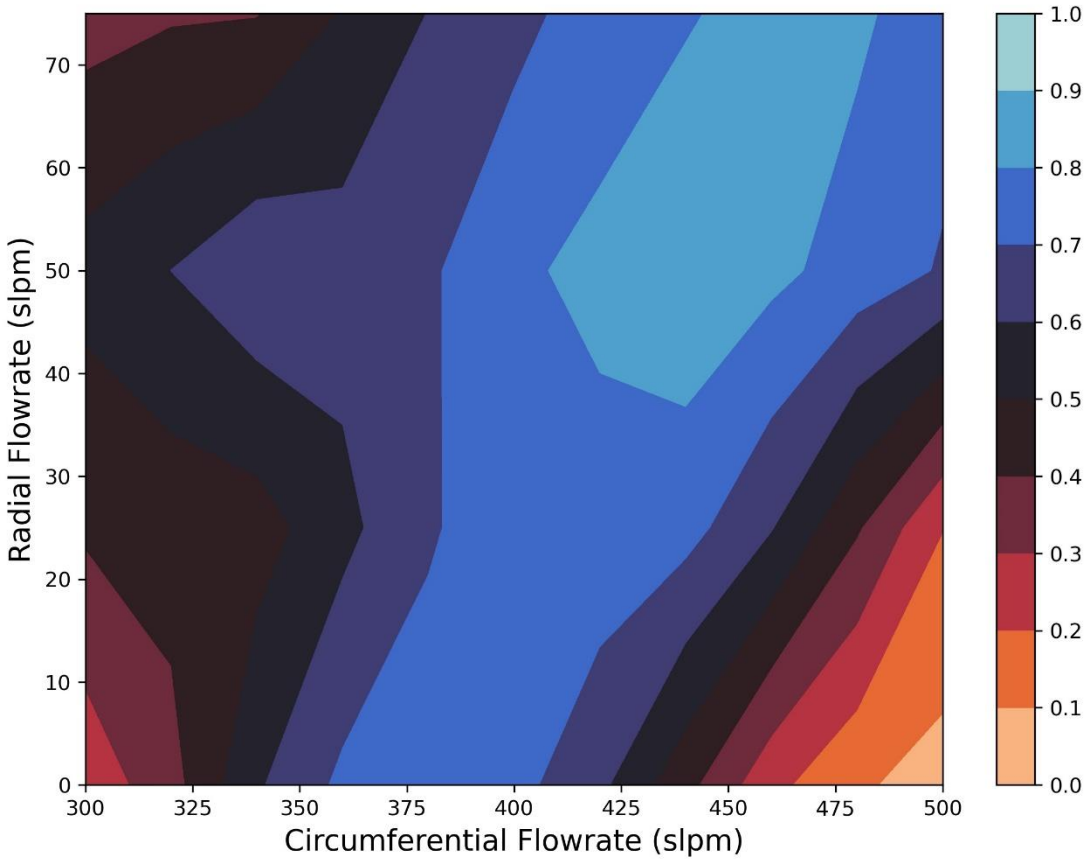

Figure 25: Flame stability of n-heptane for top flow profile configuration as a function of radial and circumferential flowrate.

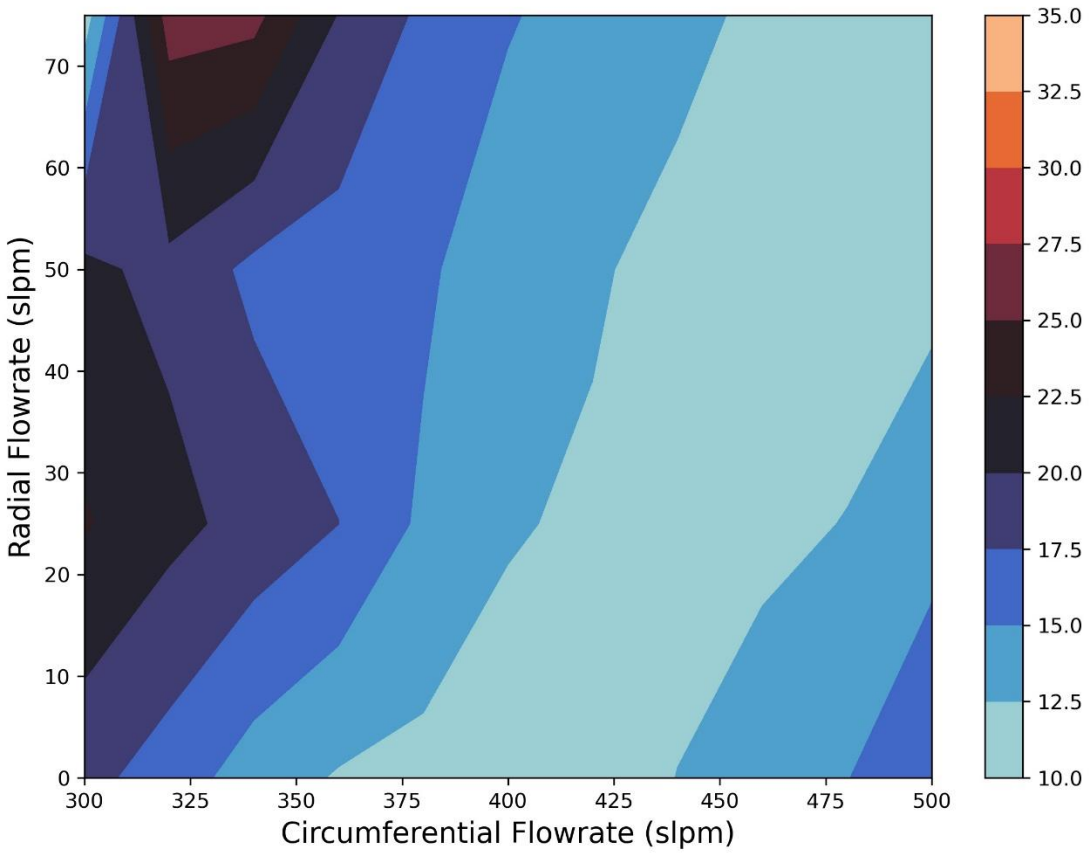

Figure 26: Soot production of n-heptane for top flow profile configuration as a function of radial and circumferential flowrate.

The contour plots, labeled “Flame Stability,” show the percentage of time the flame is in a blue whirl state for the duration of the run, 120 s. The color scale ranges from 0.0 to 1.0. A value of 0.0 would indicate that the flame was never in a blue whirl state at the given flow conditions. A value of 1.0 would indicate that the flame was always in a blue whirl state under the given conditions.

The contour plot labeled “Soot Production,” shows values of the averaged red channel pixel intensity for the frames at the given flowrate ranges. Although there is no calibration for these values, they provide a relative metric for which to compare

stability ranges. It also provides a visual that helps relate increasing blue whirl flame stability to lower soot production values. Of note is the absence of zero soot production as indicated by the scale of the contour plot. This is explained by the measurement technique. This method implements a relative comparison between frames to help quantify which frame may contain a flame producing more soot. Regardless of the flame captured in a frame, there are red channel elements in the image captured inherent to the composition of the pixels in the image – this is to say that even an all-black image with some background light would have an average red channel intensity value greater than zero. Regions of light blue do, however, indicate soot free combustion and conquer with the soot-free combustion observed and presented in [28].

Of interest is that each flow profile was capable of generating a stable blue whirl. Although each flow configuration formed a blue whirl flame at different circumferential flow rates and responded differently to the introduction of radial flow, blue whirl formation was observed for each.

Also of note is the effect of the introduction of higher radial flowrates. In each case, the addition of radial airflow widens the region of stability, expanding the stable operating conditions for the circumferential flow profile. Interestingly, the way in which it expands is not uniform to a given flow profile. For the back-bot generated flow profile, radial flow seems to stabilize the flame vertically, growing around the stable region determined at 0 slpm of radial flow. For the flow profiles generated with the back-mid and back-top, however, the flame seems to find more stability at higher

circumferential flowrates. The back-mid test, for example, is most stable between about 330-370 slpm of circumferential flowrate for 0 slpm of radial flowrate. At 75 slpm of radial flowrate, the stable region is pushed entirely past 370 slpm, beginning almost at 390 slpm. The effect of radial flow also pushes flame stability to a higher value, to about 0.9 or 90%. The trend of the back-top and back-mid flow profiles would agree with Hariharan et. al's findings of critical values for R^*, or the non-dimensionalized ratio between circulation and heat release, $\Gamma^*/\dot{Q}^*$ [26]. Assuming that the radial flow is converted to axial flow, adding to the buoyant term measured by $\dot{Q}$, higher circumferential flow rates, subsequently higher circulation values, Γ, are required to maintain the blue whirl flame regime.

To aid in visualization, the individual plots that contain flame stability and soot production for each of the flow conditions depicted in Figure 21 - 23, are shown below in Figure 27.

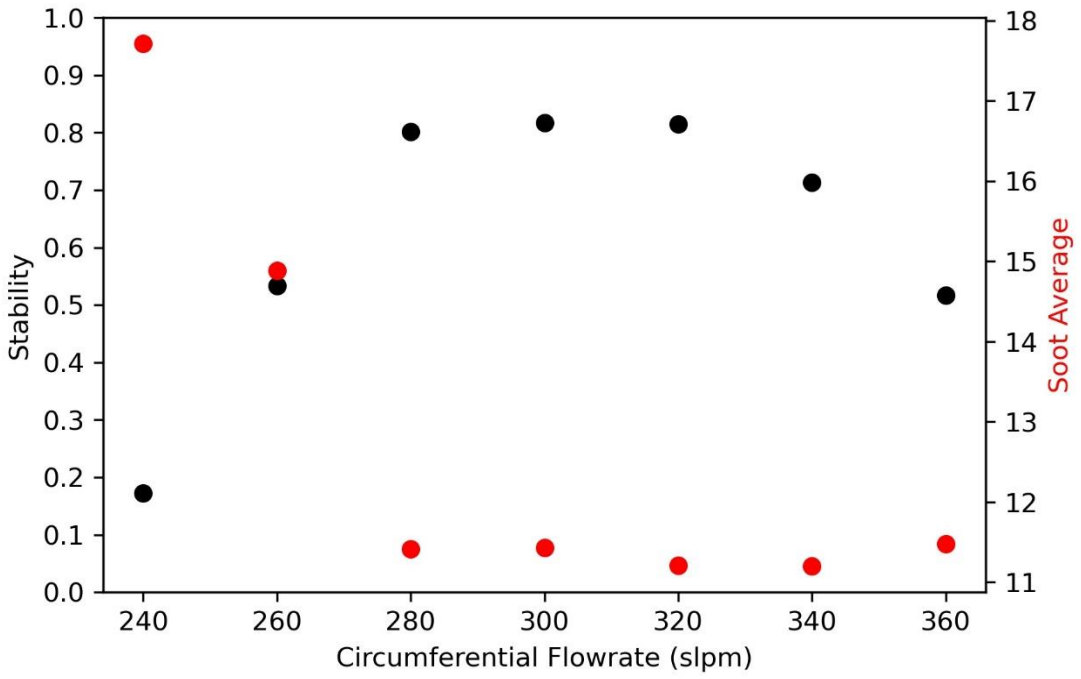

Figure 27: Flame stability and soot production for n-heptane under back-bot circumferential flow profile for radial flowrate = 0 slpm.

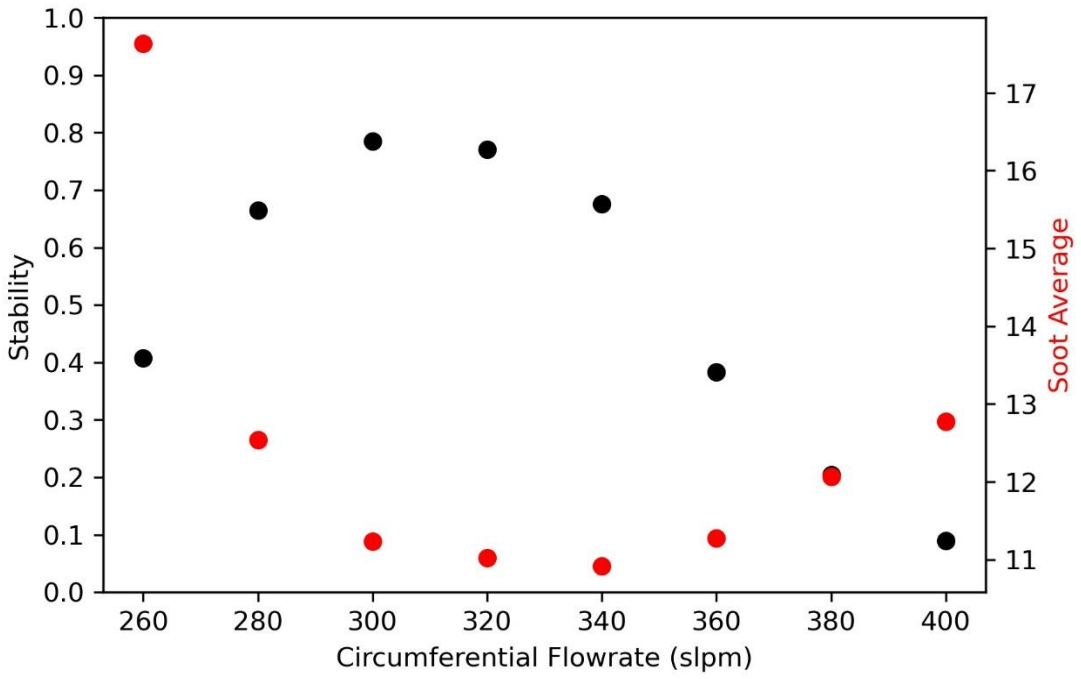

Figure 28: Flame stability and soot production for n-heptane under back-bot circumferential flow profile for radial flowrate = 25 slpm.

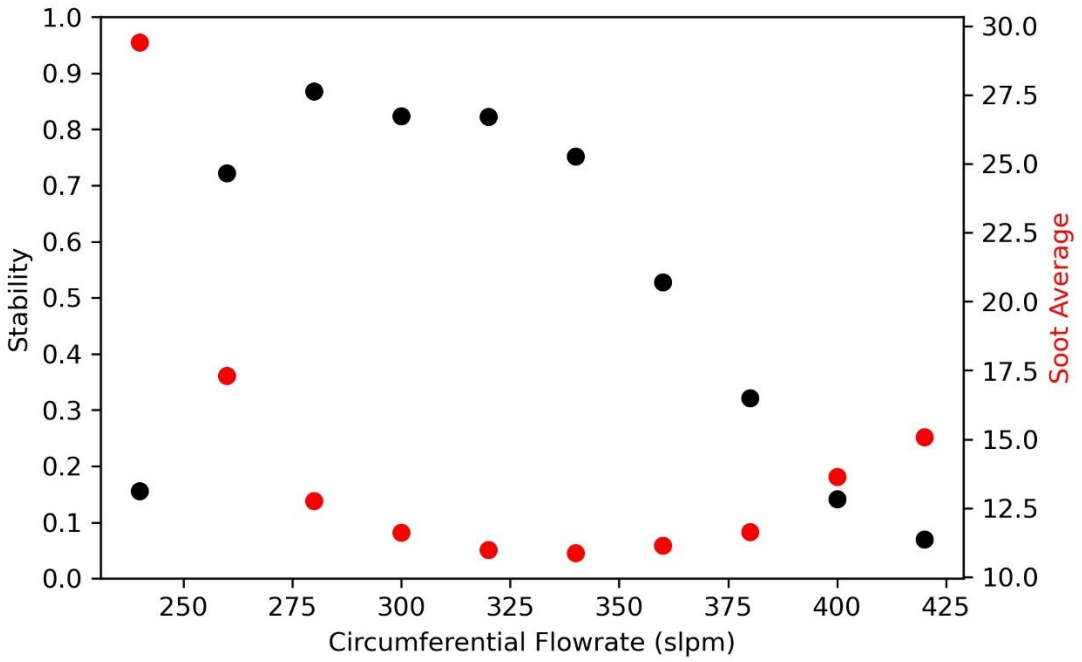

Figure 29: Flame stability and soot production for n-heptane under back-bot circumferential flow profile for radial flowrate = 50 slpm.

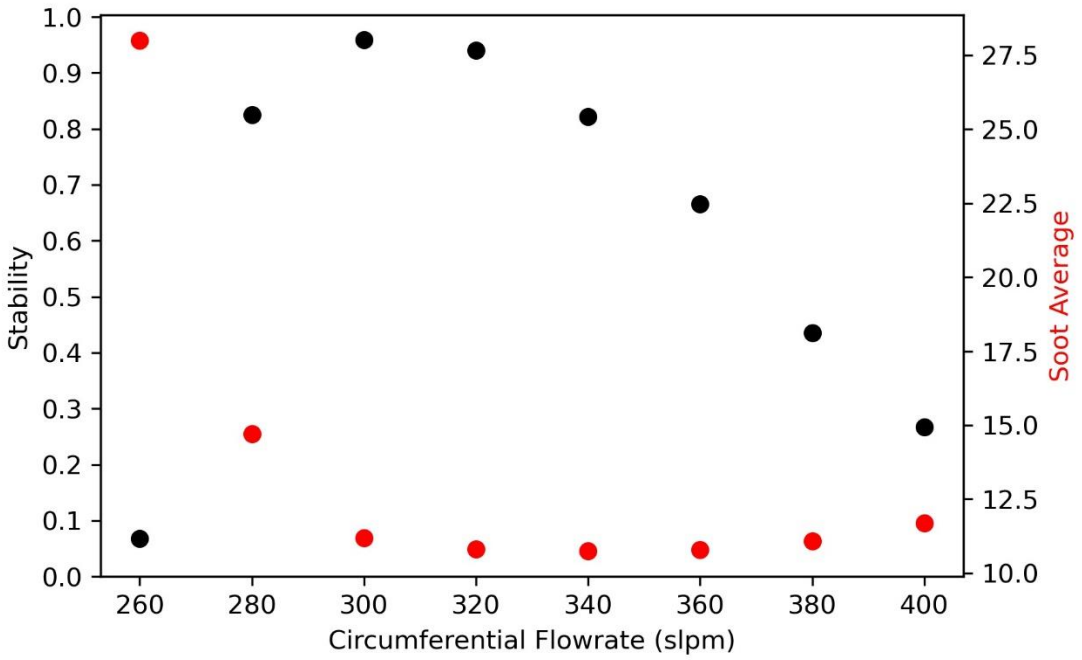

Figure 30: Flame stability and soot production for n-heptane under back-bot circumferential flow profile for radial flowrate = 75 slpm.

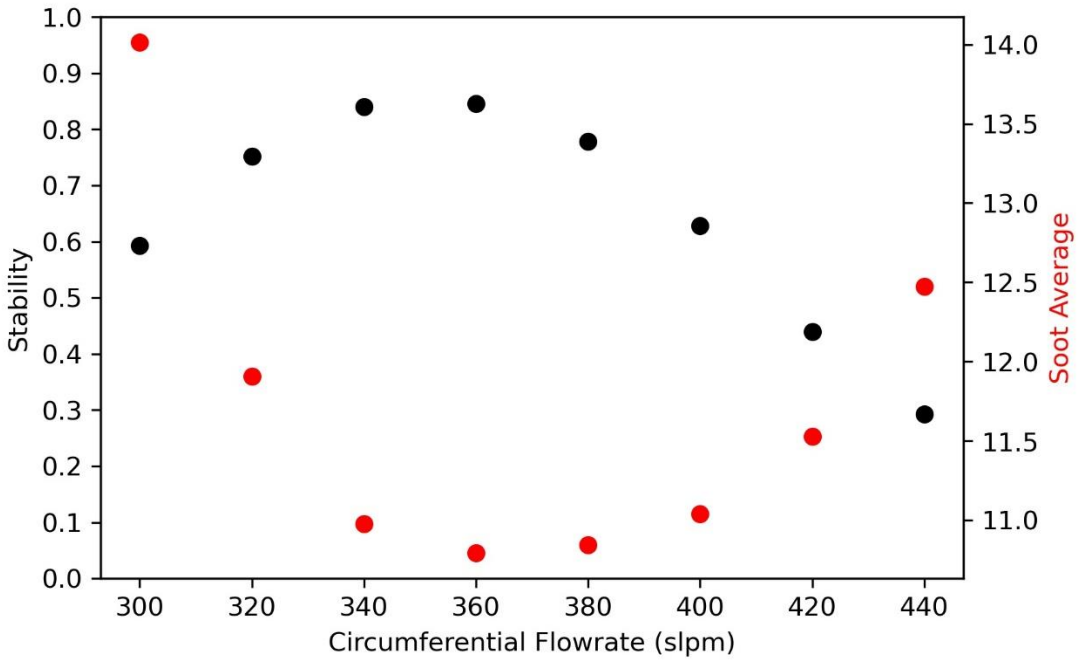

Figure 31: Flame stability and soot production for n-heptane under back-mid circumferential flow profile for radial flowrate = 0 slpm.

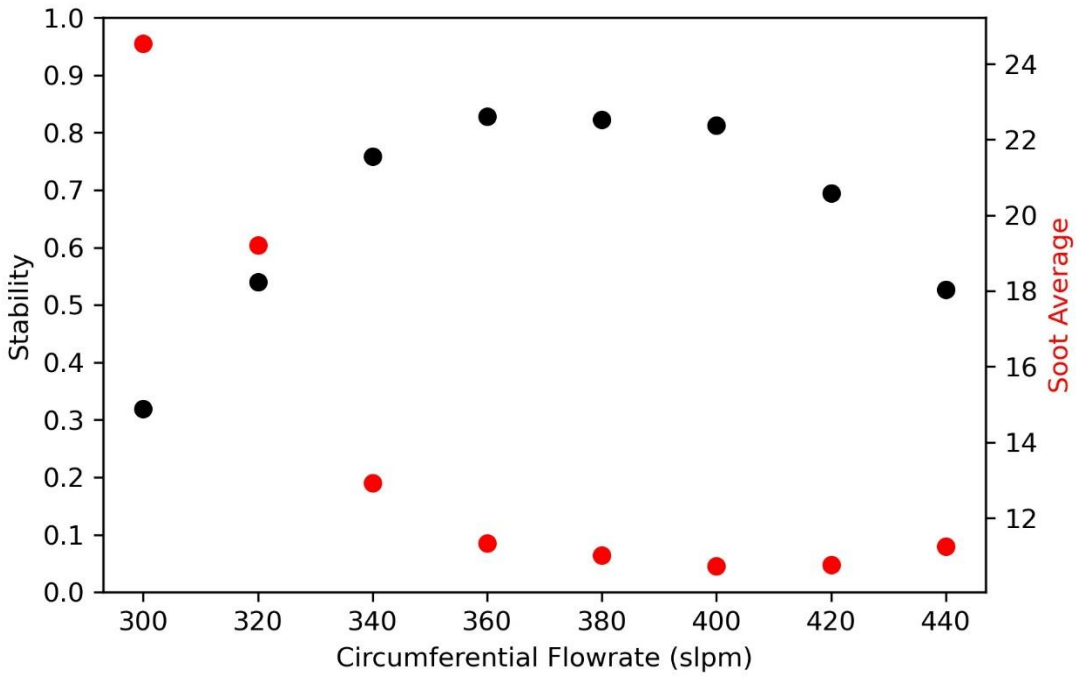

Figure 32: Flame stability and soot production for n-heptane under back-mid circumferential flow profile for radial flowrate = 25 slpm.

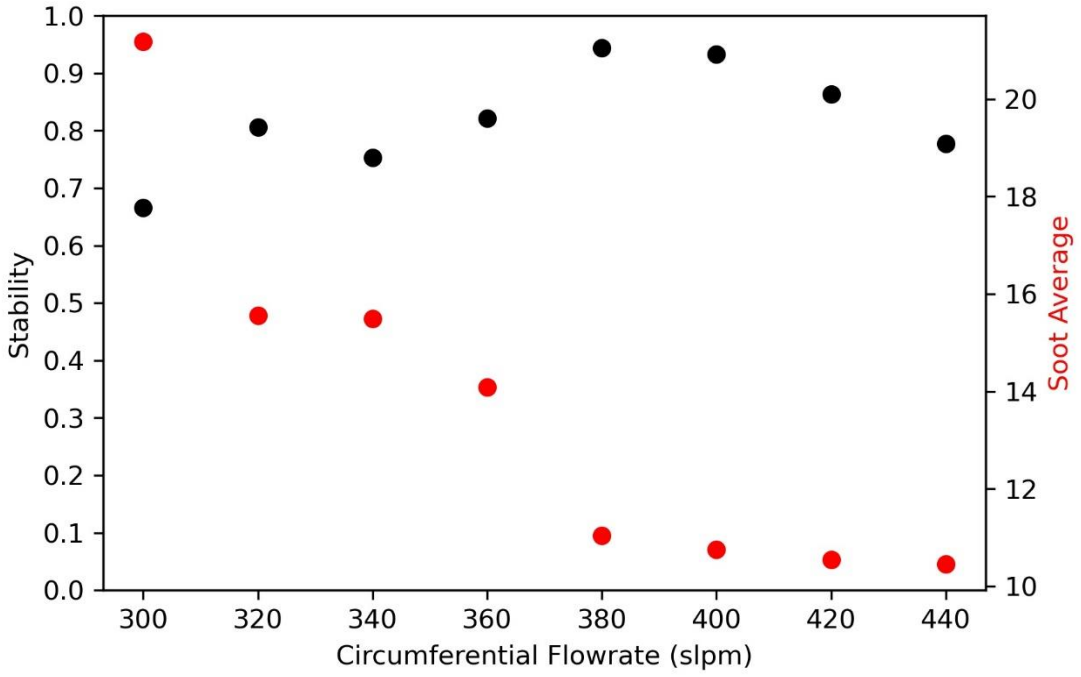

Figure 33: Flame stability and soot production for n-heptane under back-mid circumferential flow profile for radial flowrate = 50 slpm.

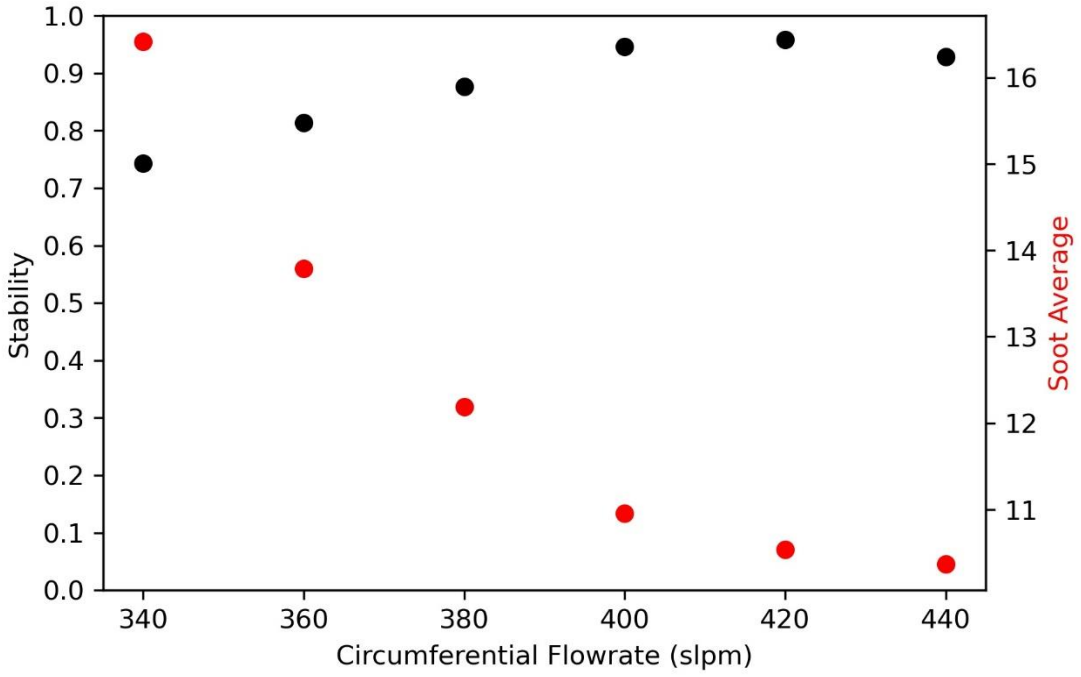

Figure 34: Flame stability and soot production for n-heptane under back-mid circumferential flow profile for radial flowrate = 75 slpm.

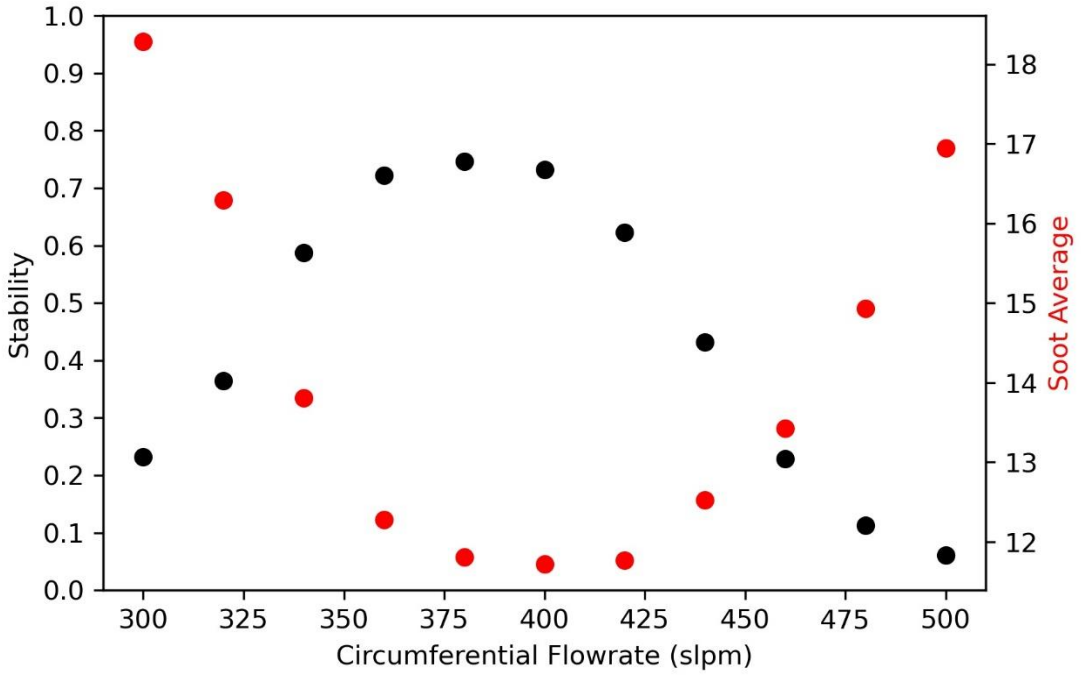

Figure 35: Flame stability and soot production for n-heptane under back-top circumferential flow profile for radial flowrate = 0 slpm.

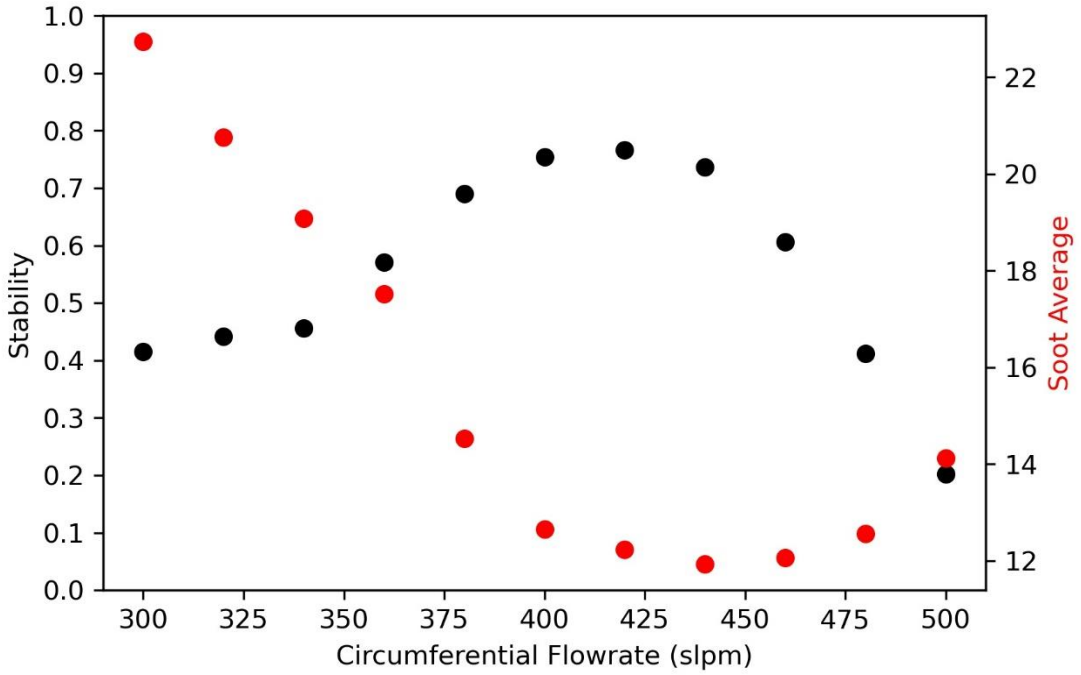

Figure 36: Flame stability and soot production for n-heptane under back-top circumferential flow profile for radial flowrate = 25 slpm.

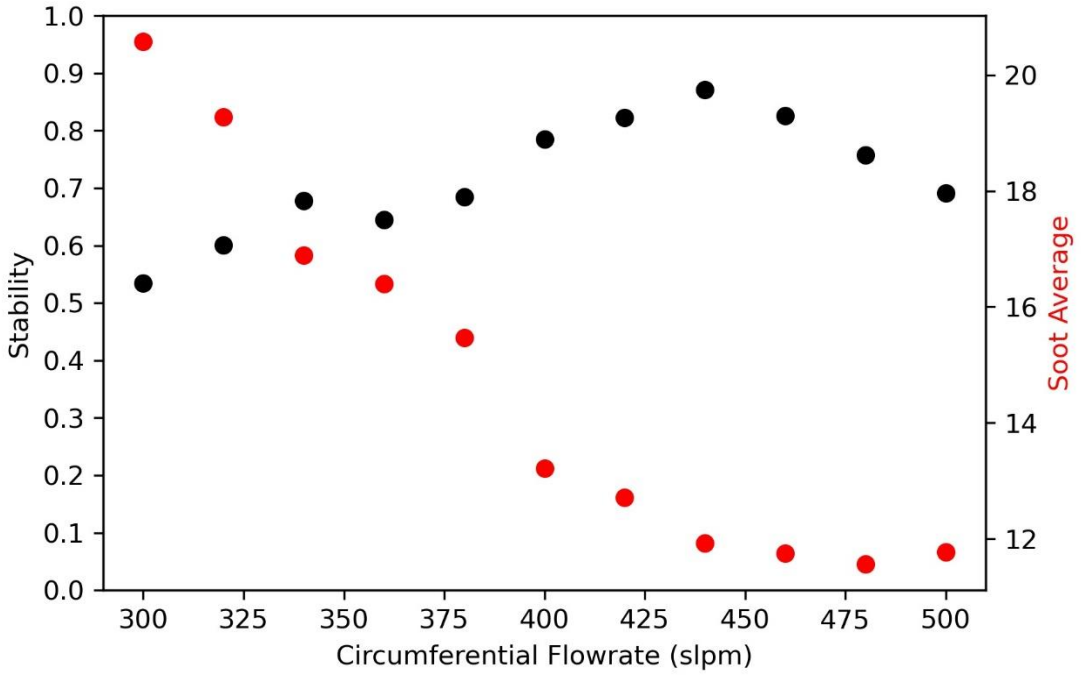

Figure 37: Flame stability and soot production for n-heptane under back-top circumferential flow profile for radial flowrate = 50 slpm.

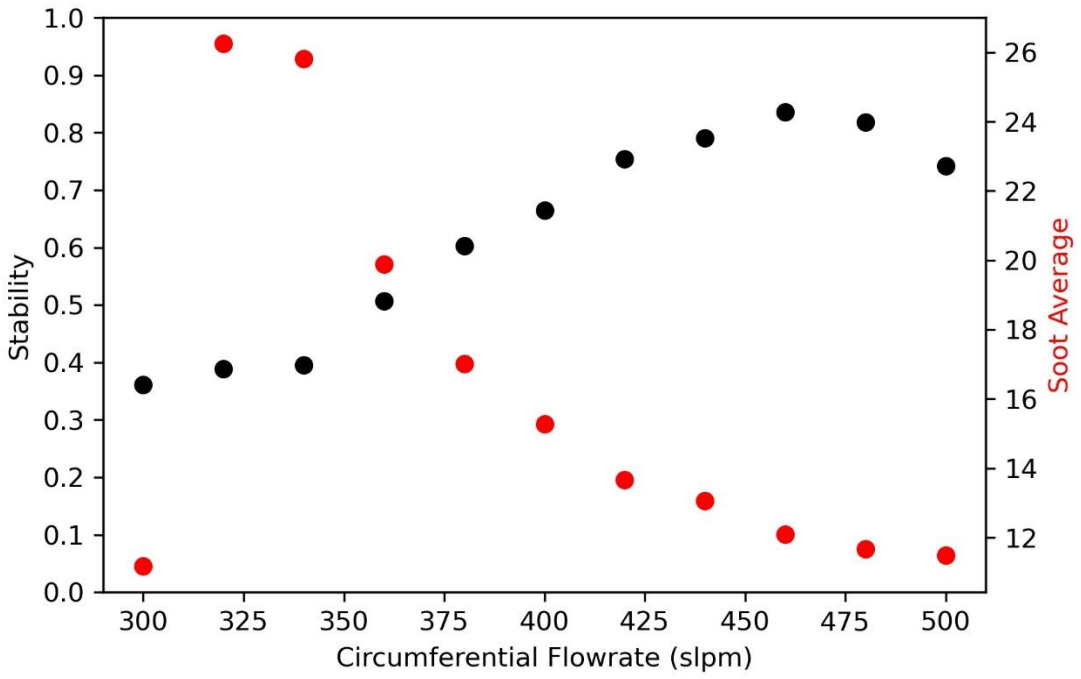

Figure 38: Flame stability and soot production for n-heptane under back-top circumferential flow profile for radial flowrate = 75 slpm.

4.2 Hysteresis Testing with Airflow

An additional piece of interest with stability measurements is blue whirl formation. Previous experimentation has only yielded blue whirl formation when transitioning from a fire whirl [26]. First, a pool fire is ignited, air is entrained circumferentially from the offset between the two quartz half shells, and the fire whirl forms. As fuel the fuel is consumed, the flame transitions to the blue whirl.

To test the effect of transitioning from a low circumferential flow rate to a high flow rate, an airflow sweep was repeated for n-heptane with two initial conditions: (1) starting the sweep with a pool fire; (2) starting the sweep with a

whirling flame, formed prior to setting the system to a lower circumferential flowrate. These measurements were performed with a radial flowrate of 0 slpm with the back-bot circumferential flow profile. If no hysteresis effects for blue whirl formation exist, the circumferential flowrate ranges of stability should be identical to the prior measurements at 0 slpm radial flow with the back-bot circumferential flow profile. The results of each test are depicted in Figure 39 and Figure 40.

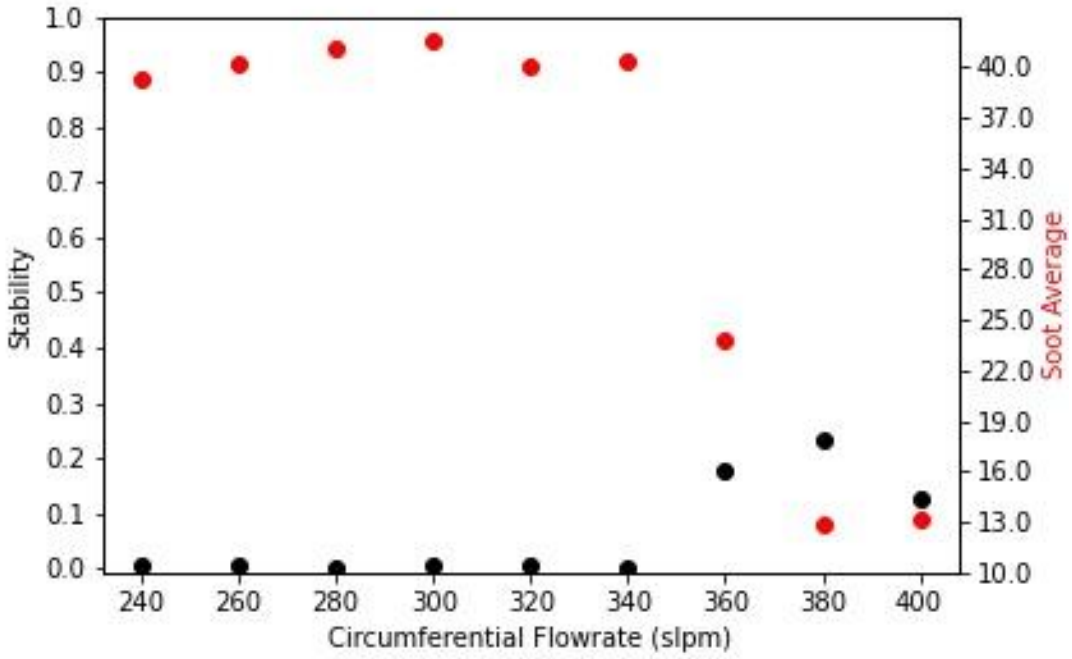

Figure 39: Flame stability and soot production of n-heptane for hysteresis measurements taken at 0 slpm radial flow. Measurement taken sweeping from a low (240 slpm) to a high (420 slpm) circumferential flowrate. Testing began without an existing whirling flame.

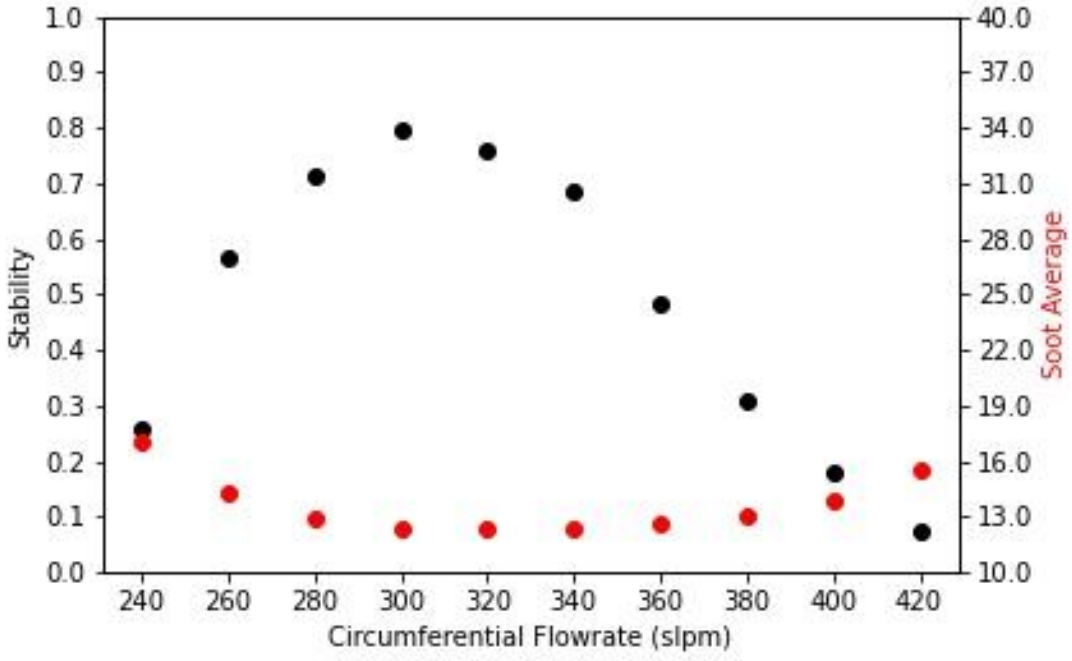

Figure 40: Flame stability and soot production of n-heptane for hysteresis measurements taken at 0 slpm radial flow. Measurement taken sweeping from a low (240 slpm) to a high (420 slpm) circumferential flowrate. Testing began with an existing whirling flame.

Comparing Figure 39 and Figure 40, it is clear that system response is different. For the sweep beginning with a pool fire (Figure 39), blue whirl formation does not begin to take place until about 360 slpm. Further, the system only reaches a maximum stability value of 0.26 or 26%. For the sweep beginning with a whirling flame, the blue whirl is already present for a portion of the time at the lower limit flowrate. Sweeping to the higher values, we see an expected stability peak of around 0.8 or 80%, and a similar trend in stability drop off as the system is pushed to higher and higher flowrates. This second measurement (Figure 40) is very similar to the measurements taken previously, sweeping from a high to low circumferential flowrate, shown in Figure 41.

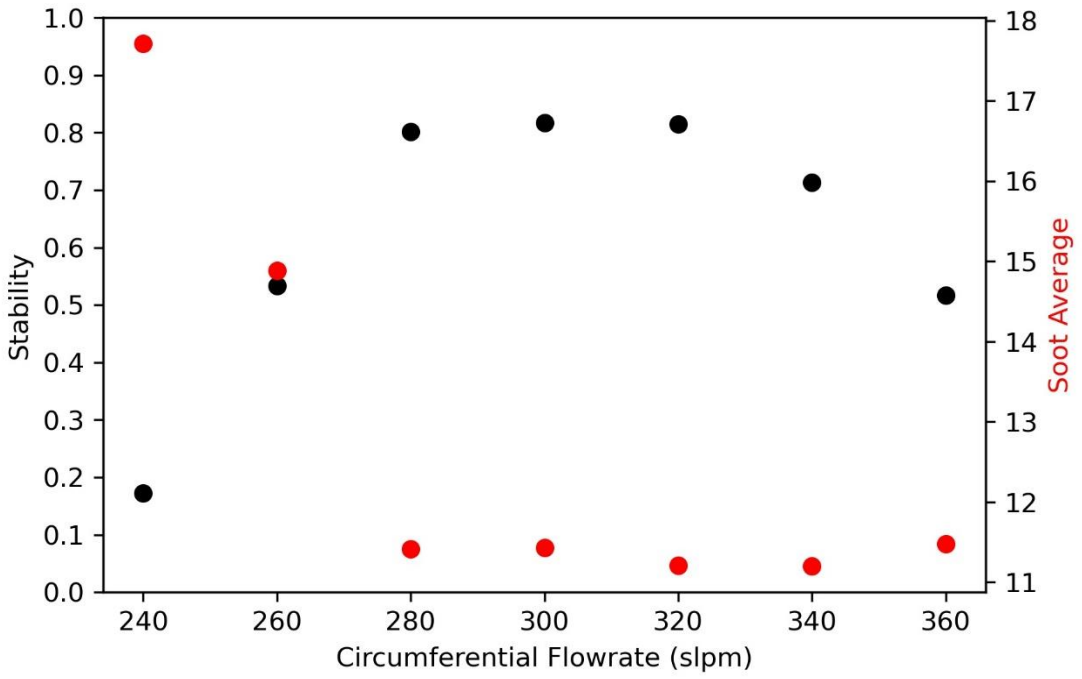

Figure 41: Flame stability and soot production of n-heptane taken at 0 slpm radial flow. Measurement taken sweeping from a high (360 slpm) to low (240 slpm) circumferential flowrate.

Although not identical, the general trend in soot production and flame stability agree for both measurements taken in Figure 40 and Figure 41. Because the first sweep's results are so different, we can infer that the mechanism for formation of the blue whirl is critical. This inference suggests a similar phenomenon to that of the results discussed in [42], [43]. Further investigation into hysteresis of vortex formation is needed to identify the precise workings of the mechanism at play.

4.3 Impact of Fuel Type on Stability Ranges as a Function of Circumferential and Radial Flowrate

To test the effect of fuel type on the flame stability ranges, two other fuels, n-octane and methyl acetate, were run at approximately the same heat release rate

(HRR) that was used for n-heptane. We hypothesized that the stability range, as a function of radial and circumferential flow rate, would remain the same for any fuel given a fixed HRR. N-octane and methyl acetate were selected as the other two model fuels. N-octane is a gasoline surrogate and methyl acetate, a member of the methyl ester family (commonly used as bio diesel surrogate). The test conditions, with the exception of the fuel flow rate, were held the same for n-heptane. To crop the data to a region of interest, n-octane and methyl acetate were only run from 400 slpm to 260 slpm, removing the larger instability regions found for n-heptane. These tests were only run in the back-bot circumferential flow profile configuration. The measured stability plots are depicted in Figure 42 and Figure 43. Table 1 details the fuel flow rates and heat release rates used for each fuel tested. Again, note the relatively small fire size, less than 400 W. When looking towards a fuel flexible technology, it is clear that a scale up of energy produced from the blue whirl will be required.

Fuel Type	Fuel Flow Rate* (ml/min)	HRR (kW)
n-heptane	.752	.376
n-octane	.752	.387
methyl acetate	1.10	.336

Table 1: Calibrated fuel flow rates (ml/min) and heat release rates (HRR) for each fuel tested

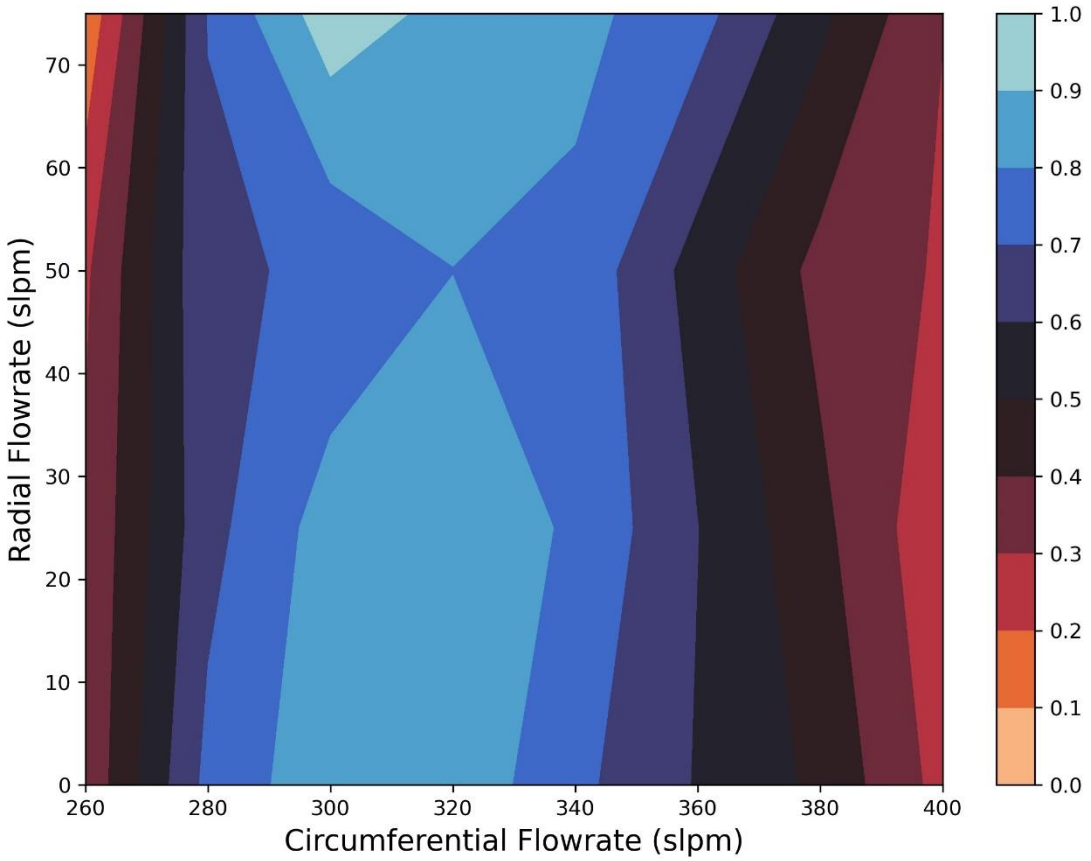

Figure 42: Flame stability of n-octane for bottom flow profile configuration as a function of radial and circumferential flowrate.

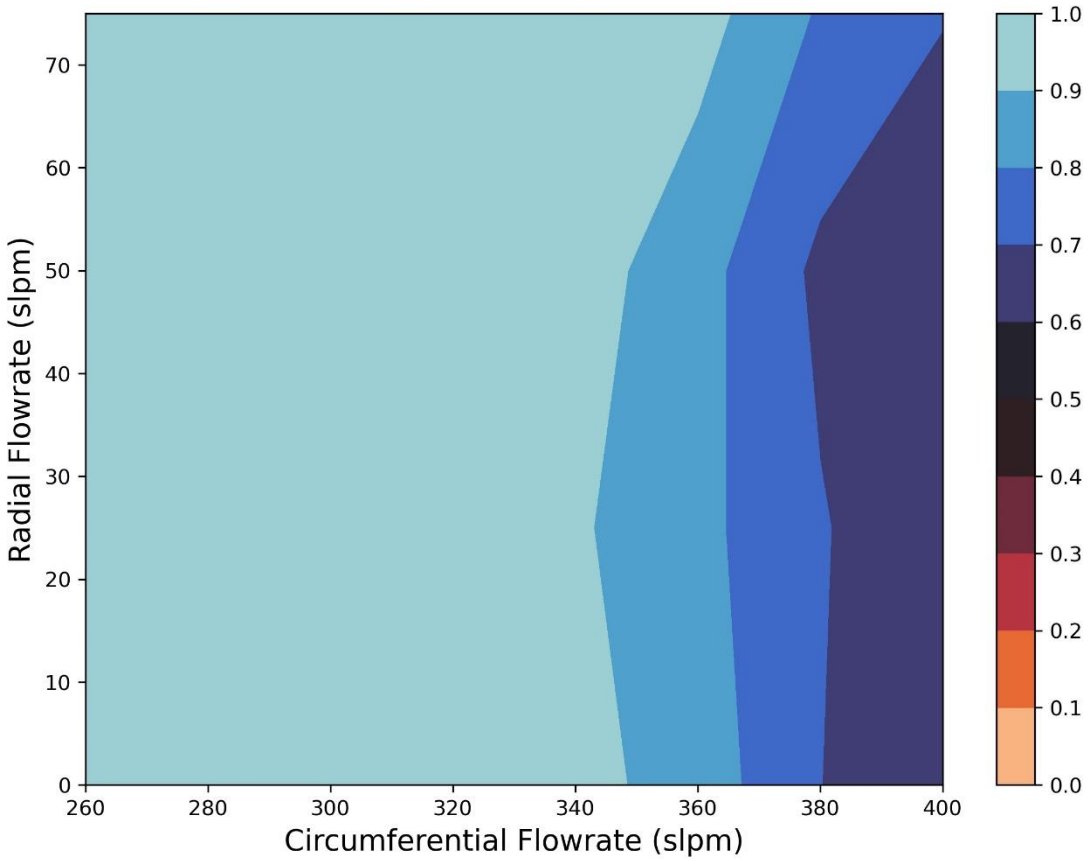

Figure 43: Flame stability of methyl acetate for bottom flow profile configuration as a function of radial and circumferential flowrate.

N-octane presents a comparable stability plot to that of n-heptane. The 280-340 slpm region at zero radial flow is the region of highest stability, and a peak in stability is seen at 300 and 75 slpm for circumferential and radial flow respectively. The stability plot for methyl acetate, however, tells a very different story to that of n-heptane and n-octane. The regions and general trend of instability agree with that of n-heptane and n-octane for the higher circumferential flow rates (>360 slpm). Although the trend is similar, the stability is actually much higher, almost 0.4 higher at the extreme. Further, highlighting the stability differences between the fuel types is

the lower circumferential flow rates. Methyl acetate is able to operate above 0.9 stability for all radial flow rates once lower than 340 slpm. No performance decrease is seen sweeping down to 260 slpm. This is in stark contrast to n-heptane and n-octane because the stability region is significantly larger. Additionally, radial flowrates between 0 and 75 slpm appear to have no effect on flame stability.

A hypothesis for the difference in stability limits due to the different fuel types is the change in mass flux of each fuel. Although not directly applicable, the Stefan problem, which describes the diffusion of a liquid fuel to a flowing mixture of gas across the top of a cylinder, may lend some insight. If the flowing mixture of gas A and gas B contains a concentration of A less than the concentration of gas A at the liquid-vapor interface inside the tube, species A will diffuse into the flowing mixture of gases. The equation for the mass flux of liquid A is given by [45], and can be calculated by:

$$m_A{}'' = \frac{\rho D_{AB}}{L} \ln\left(\frac{1 - Y_{A\infty}}{1 - Y_{Ai}}\right) \quad (1)$$

In (1), D_{AB} represents the diffusion constant between the liquid species A and gas B. Here, A represents the fuel species and B represents Air. The diffusion coefficient in air for methyl acetate and n-octane are .000005 m/s^2 and .000009 m/s^2 respectively. Further, the density of n-octane and methyl acetate are 703 kg/m^3 and 932 kg/m^3 respectively. The mass flux of fuel, $\dot{m}_A{}''$, is directly proportional to both the density of the fuel and diffusion coefficient of the fuel and air mixture. These intrinsic properties of the fuel may lead to critical differences in fuel and oxidizer

mixing, allowing methyl acetate to remain a blue whirl for a wider range of flow rates. This hypothesis echoes the hypothesis of Tummers et. al for their hysteretic changes in transition points between flame regimes [43]. Most importantly, however, these experiments indicate that there is more to blue whirl formation and stability than the relationship between circulation and buoyancy of the system.

The 2D individual plots for flame stability and soot production of n-octane and methyl acetate are shown in Figure 44 - Figure 51.

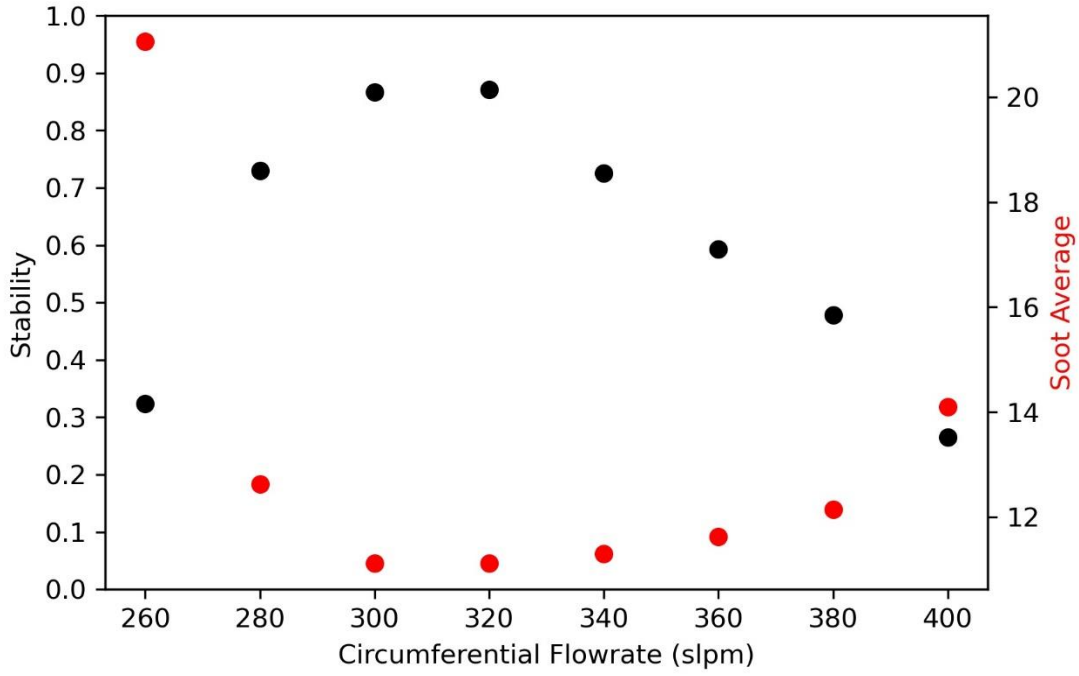

Figure 44: Flame stability and soot production for n-octane under back-bot circumferential flow profile for radial flowrate = 0 slpm.

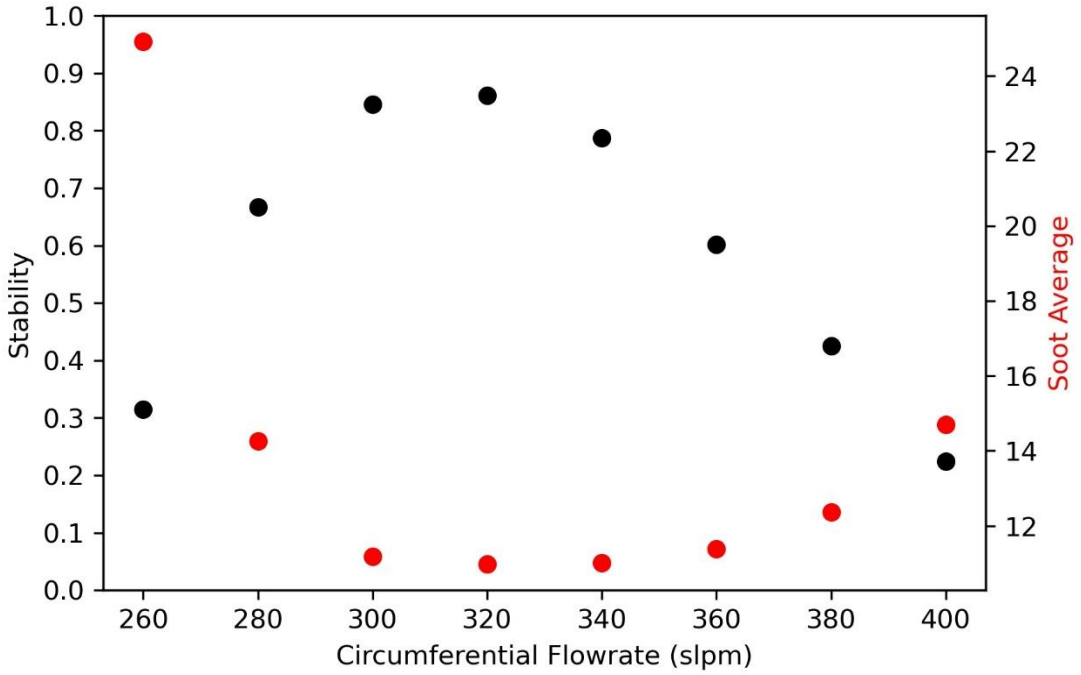

Figure 45: Flame stability and soot production for n-octane under back-bot circumferential flow profile for radial flowrate = 25 slpm.

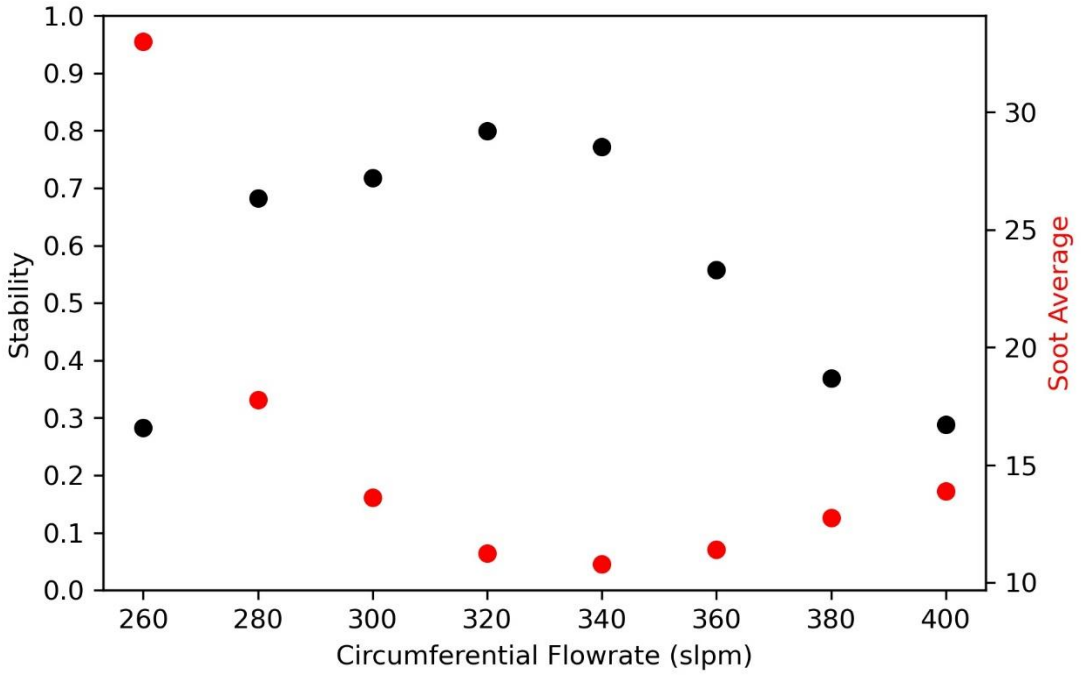

Figure 46: Flame stability and soot production for n-octane under back-bot circumferential flow profile for radial flowrate = 50 slpm.

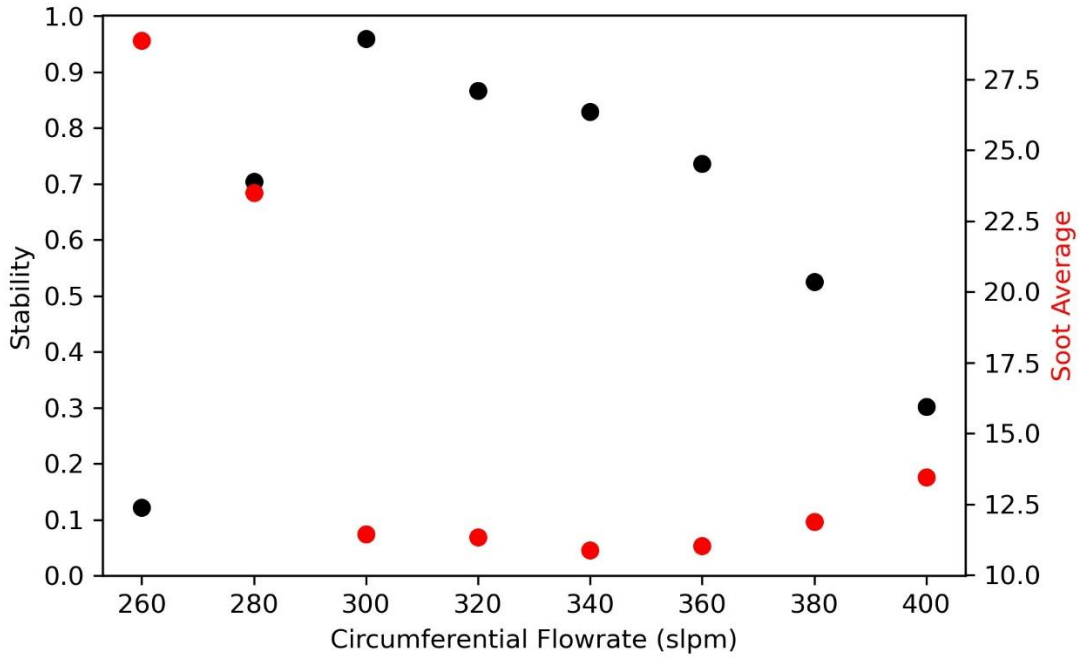

Figure 47: Flame stability and soot production for n-octane under back-bot circumferential flow profile for radial flowrate = 75 slpm.

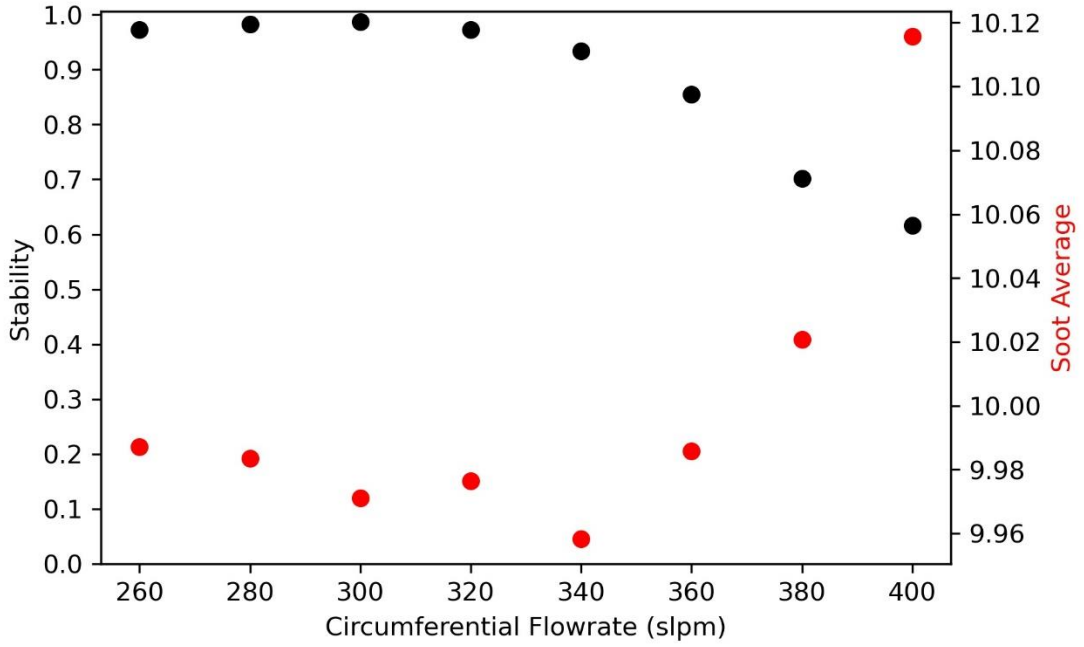

Figure 48: Flame stability and soot production for methyl acetate under back-bot circumferential flow profile for radial flowrate = 0 slpm.

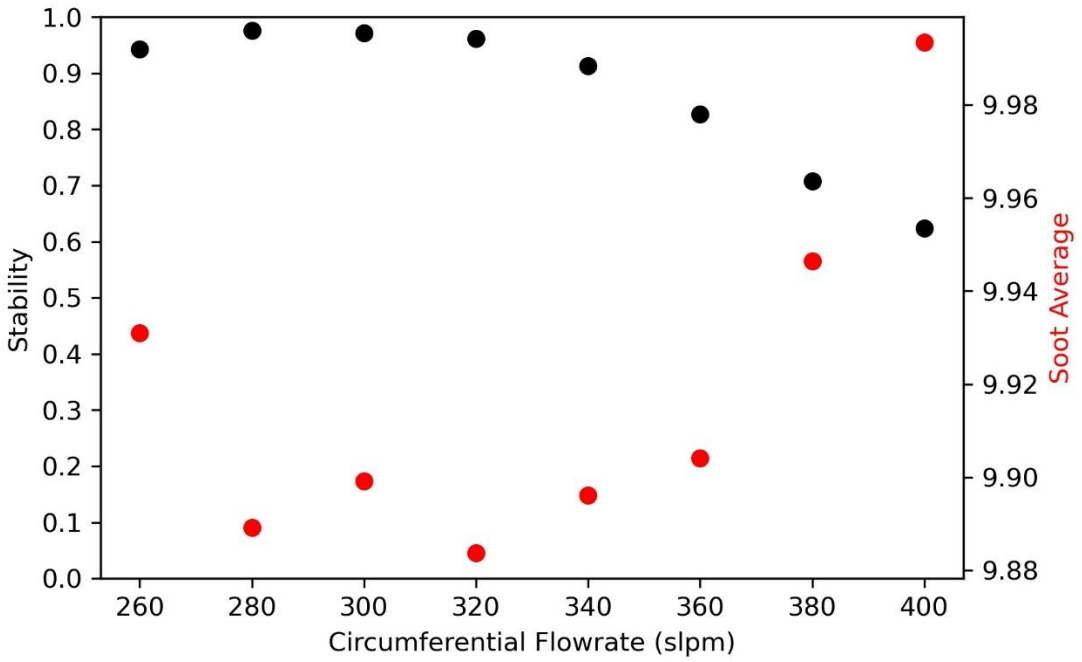

Figure 49: Flame stability and soot production for methyl acetate under back-bot circumferential flow profile for radial flowrate = 25 slpm.

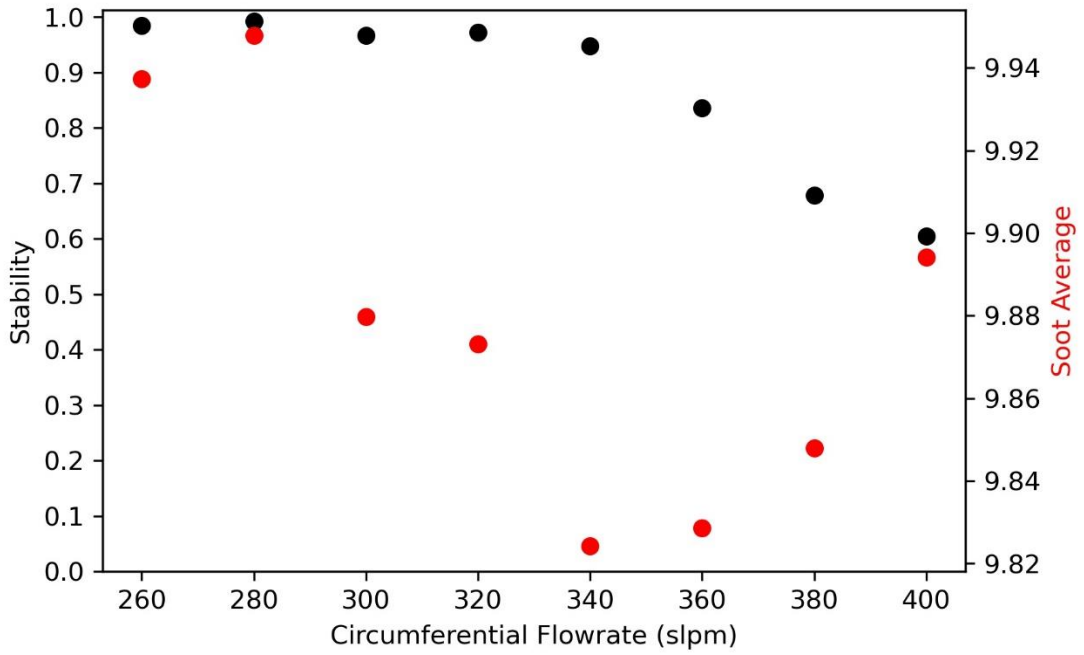

Figure 50: Flame stability and soot production for methyl acetate under back-bot circumferential flow profile for radial flowrate = 50 slpm.

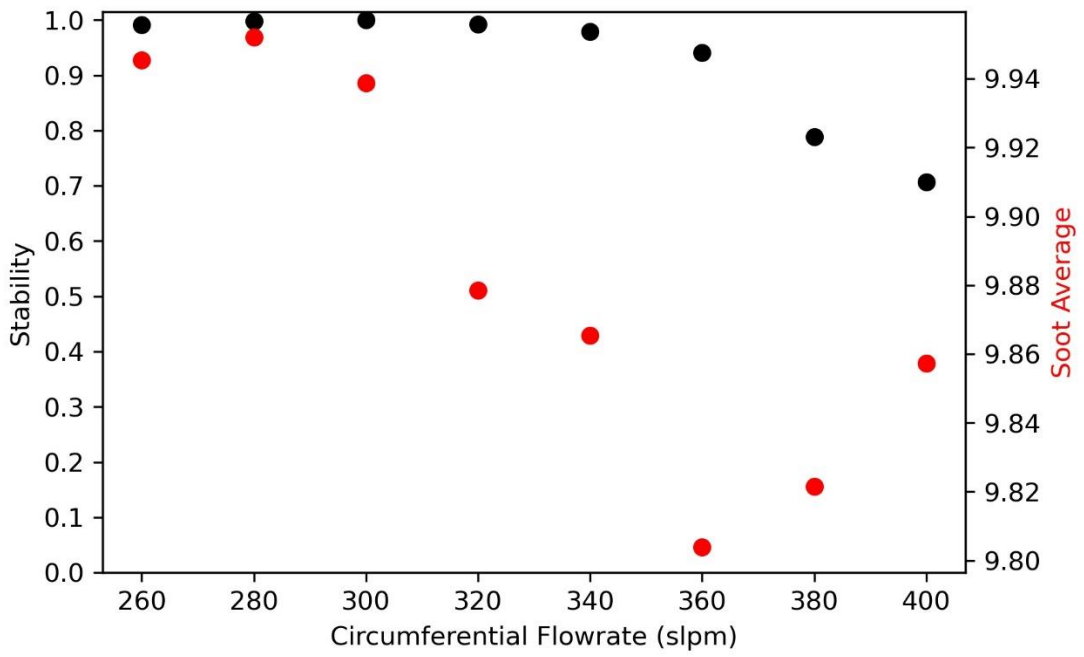

Figure 51: Flame stability and soot production for methyl acetate under back-bot circumferential flow profile for radial flowrate = 75 slpm.

4.4 Hysteresis Testing with Fuel Flow

Hysteresis testing as a function of fuel flow rate was also performed. For this measurement, the standard procedure of fire whirl to blue whirl formation was performed by beginning with a large pool fire. Circumferential air was injected with the back-bot profile. Circumferential and radial air were then injected at 300 slpm and 75 slpm, respectively, and fuel was pumped to the surface at each given rate for the measurement. Images were collected for 120 s once steady state was reached. The fuel rate was first swept from low (0.2 ml/min) to high (1.3 ml/min) and then from

high to low. The results of flame stability and soot production are depicted in Figure 52 and Figure 53.

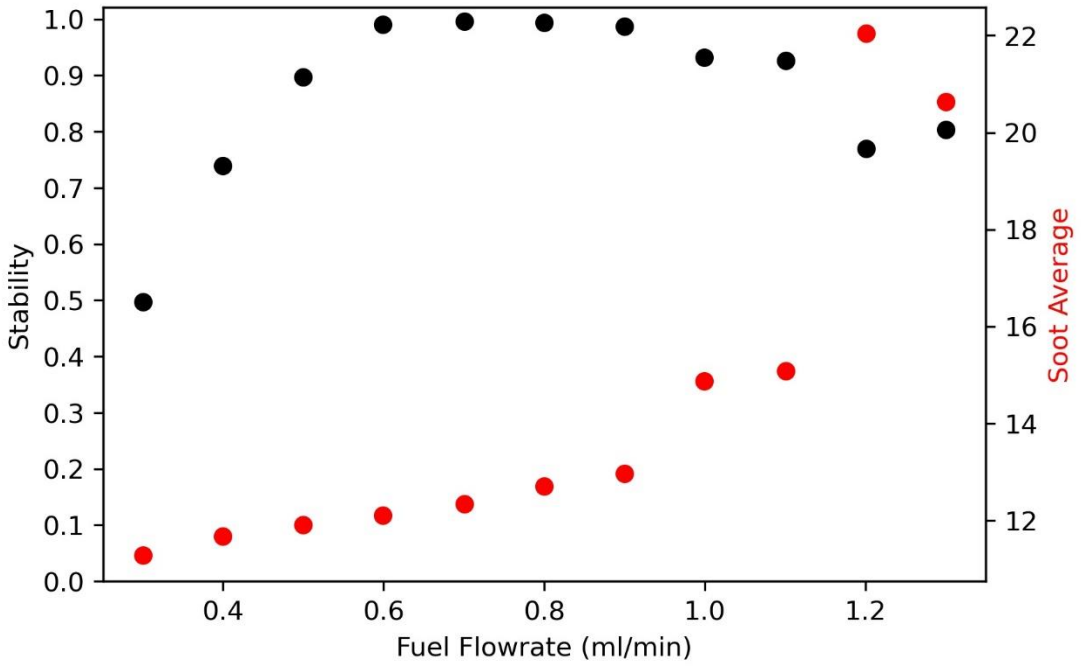

Figure 52: Flame stability and soot production of n-heptane, sweeping the fuel flowrate from high (1.3 ml/min) to low (0.2 ml/min).

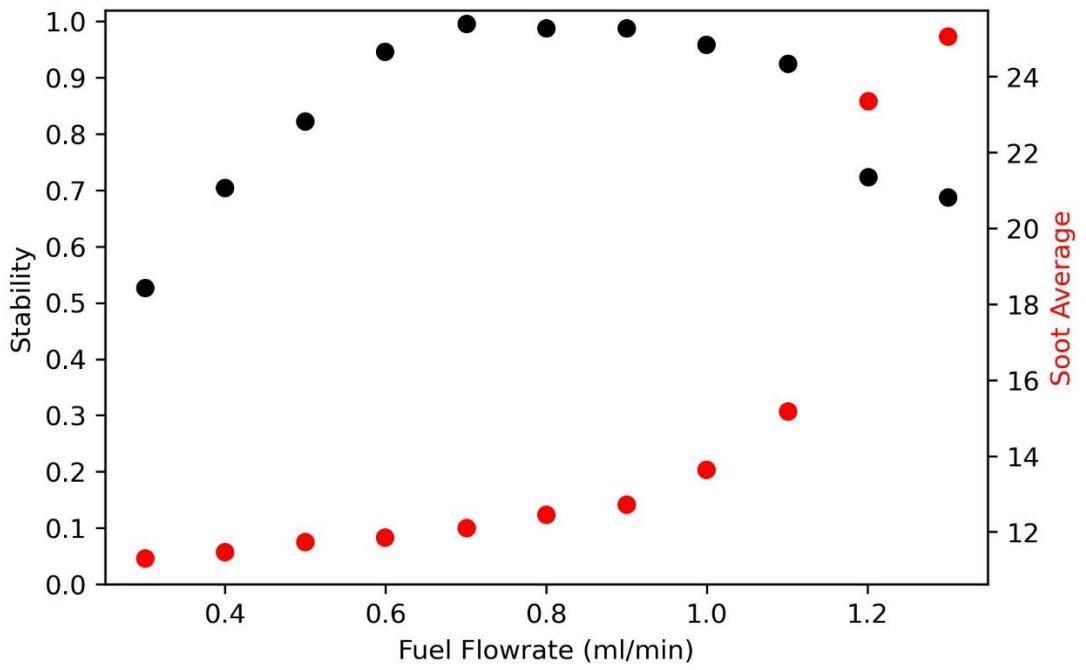

Figure 53: Flame stability and soot production of n-heptane, sweeping the fuel flowrate from low (0.2 ml/min) to high (1.3 ml/min).

The results suggest there are no hysteresis effects of fuel flow rate. We hypothesize that this is in large part due to the conditions required for blue whirl formation and stability. The upper limit for the fuel flowrate is dictated by the requirements described by [26]. Once the flow transitions from the circulation dominated regime, impacted by the higher axial flow due to excessive fueling and subsequently higher buoyancy, blue whirl stability suffers. The lower limit appears to be dictated by extinction. Once the flow becomes overly circulation dominated, extinction due to blowout occurs. The results are not surprising and agree with the previous hysteresis tests. They reinforce that the blue whirl regime is dominated by fluid mechanics; so long as the correct circulation to buoyancy ratio can be achieved, a stable blue whirl will form. Thus, as long as the fuel flow rate meets the required

ratio, the blue whirl will form. Small changes then, say from 0.6 ml/min to 0.75 ml/min, will not perturb blue whirl stability because the circulation to axial flowrate ratio is still within the appropriate range.

4.5 Results Presented as a Function of Circulation

To provide a comparable set of data for other literature regarding fire whirls and blue whirls, the results were re-analyzed, replacing the circumferential flow rate with circulation. The circulation was calculated according to $\Gamma = \pi U_\theta D_c$, where U_θ is the tangential velocity, and D_c is the diameter of the enclosure, or 12". To determine circulation, a height needed to be selected at which to measure velocity. Unlike fire whirls, where U_θ can be approximated as constant along the z axis [25], the imposed circumferential flow profiles tested vary significantly with a change in Z. To determine an appropriate height, 50 images containing blue whirl flames were analyzed for each flow profile. The average blue whirl rim height was measured. The chosen rim height for analysis was 0.5" above the burning surface. Velocity data, used for calculating U_θ, can be seen in appendix A.1.

4.5.1 N-heptane Blue Whirl Stability as a Function of Radial Flowrate and Circulation

Figure 54-56 show the stability contour plots as a function of circulation and radial flow rate. Figure 57 shows the 2D stability and soot production behavior for n-heptane as a function of circulation and radial flowrate. There are some interesting changes in data visualization that are present because of the switch to circulation. Most notably, perhaps, is the further refinement of stability range. These contours

plots suggest specific circulation values at which the whirling flame begins to transition to a blue whirl and at which the blue whirl begins to transition to a non-whirling flame. This phenomenon may perhaps be explained by the location measurement for velocity. Inspecting the velocity measurement plots, it can be seen that the velocity, at a height of 0.5" above the burning surface, does not increase linearly with flowrate. The result is non-linearly varying circulation values. Subsequently, the flowrate values of 240 and 260 slpm lend a significantly lower change in circulation. This relationship, however, does not hold true for all measurements, and further refinement will be required to reinforce these findings.

Of the three contour plots, Figure 55 shows behavior that is significantly different from its circumferential flow counterpart. This significant change is largely due to the velocity. The velocity profile, shown in A.1 and in Figure 13, has its largest peak in the center of the flow straightener, around 6" above the burning surface, and two smaller peaks above and below the middle mark. Both of the smaller peaks experience large fluctuations in velocity as the flowrate increases and decreases. Most importantly, at several higher circumferential flowrates, the local velocity, U_θ, decreased. The result is stability data that has been shifted when plotted as a function of circulation. Although the plot becomes more convoluted, it does indicate a few possibilities: (1) circulation is not the only driving factor impacting blue whirl formation and stability; (2) circulation at the blue whirl's vortex rim may not be as important as other locations for the flame; or (3) circulation at several locations, not just the vortex rim, is important for blue whirl formation and stability.

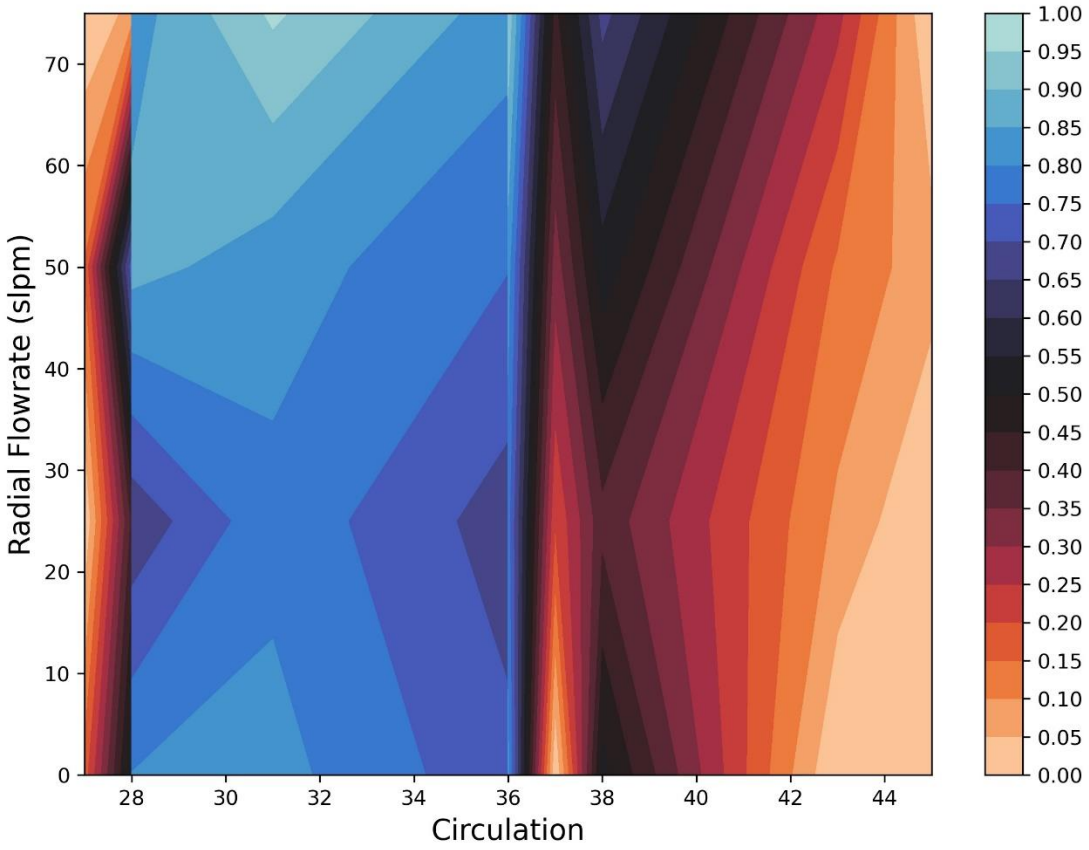

Figure 54: Flame stability of n-heptane for the bottom flow profile configuration as a function of radial flowrate and circulation.

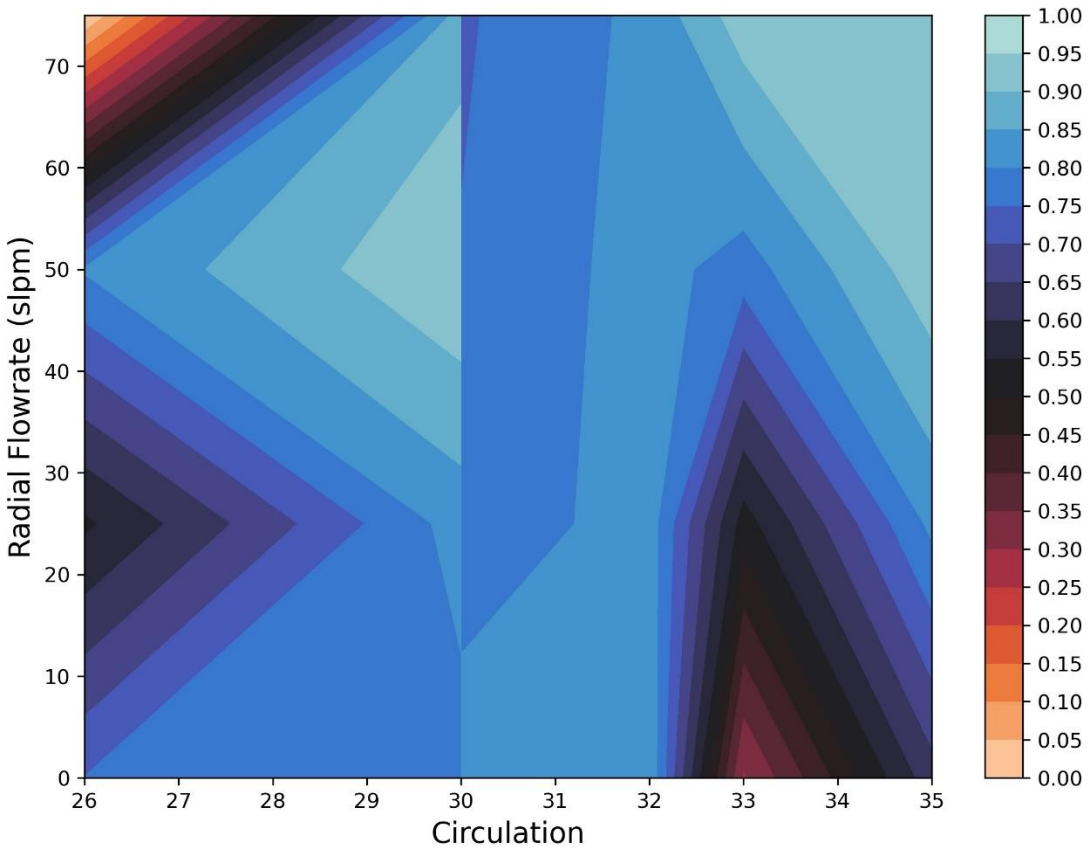

Figure 55: Flame stability of n-heptane for the middle flow profile configuration as a function of radial flowrate and circulation.

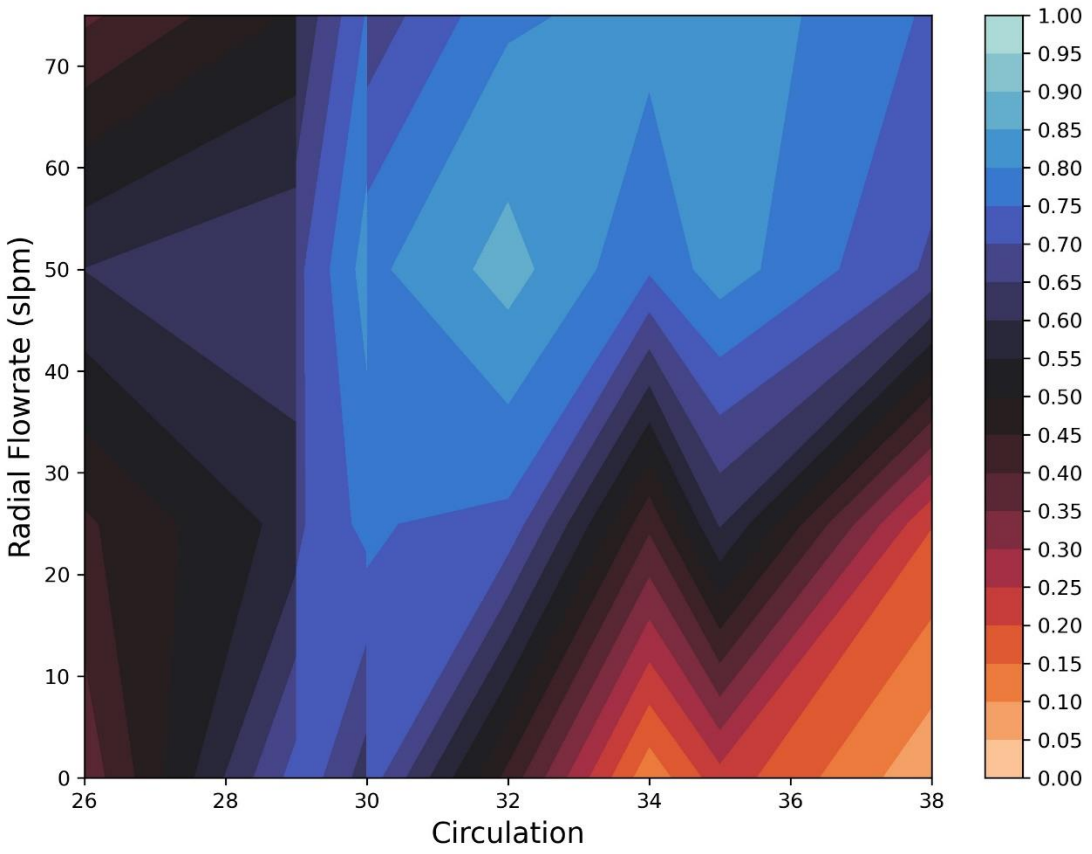

Figure 56: Flame stability of n-heptane for the top flow profile configuration as a function of radial flowrate and circulation.

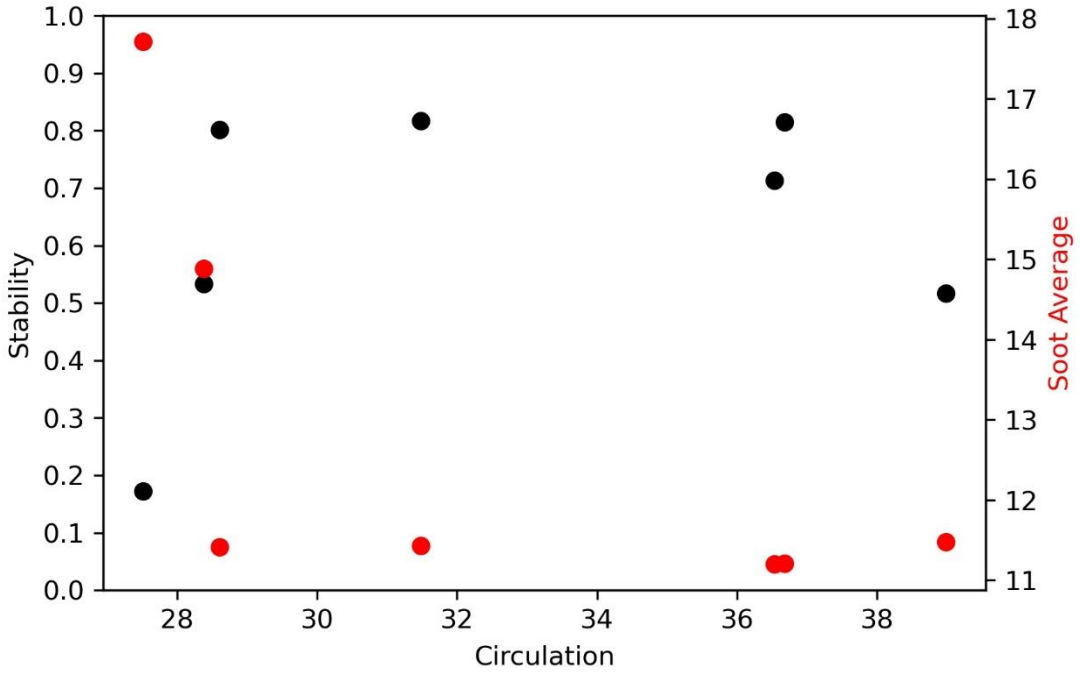

Figure 57: Flame stability and soot production as a function of circulation for n-heptane under back-bot circumferential flow profile conditions with a radial flowrate of 0 slpm.

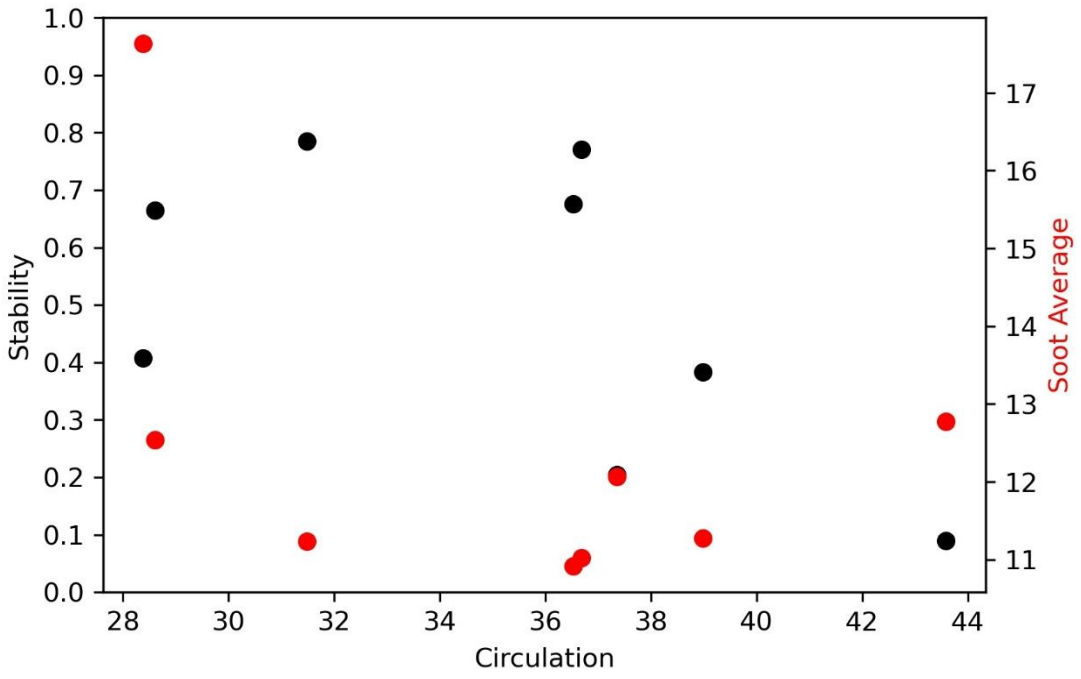

Figure 58: Flame stability and soot production as a function of circulation for n-heptane under back-bot circumferential flow profile conditions with a radial flowrate of 25 slpm.

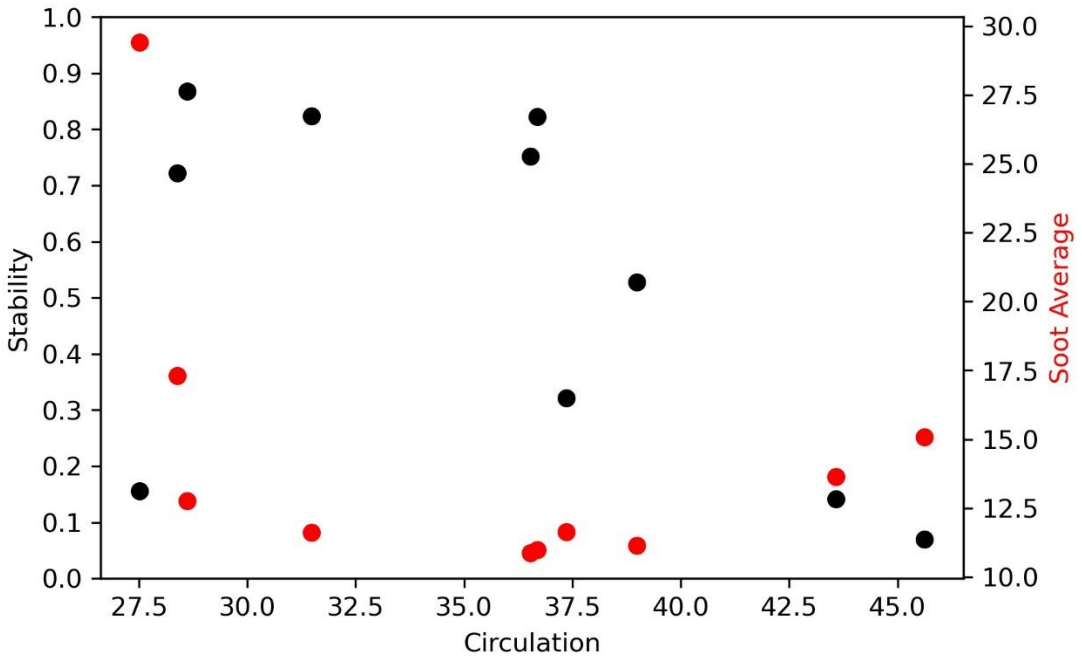

Figure 59: Flame stability and soot production as a function of circulation for n-heptane under back-bot circumferential flow profile conditions with a radial flowrate of 50 slpm.

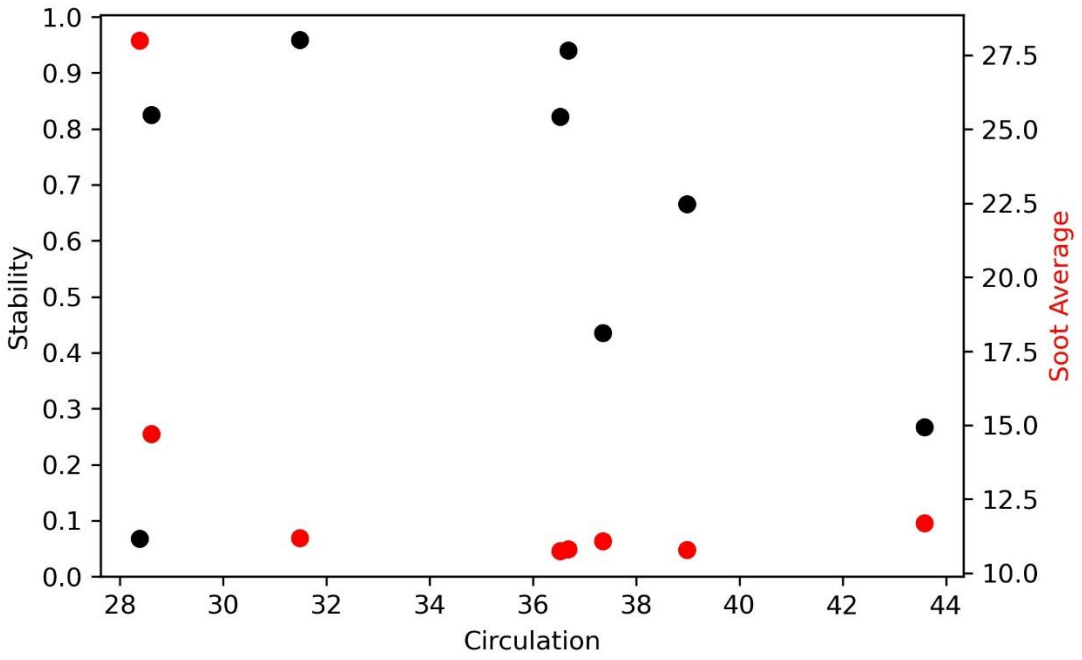

Figure 60: Flame stability and soot production as a function of circulation for n-heptane under back-bot circumferential flow profile conditions with a radial flowrate of 75 slpm.

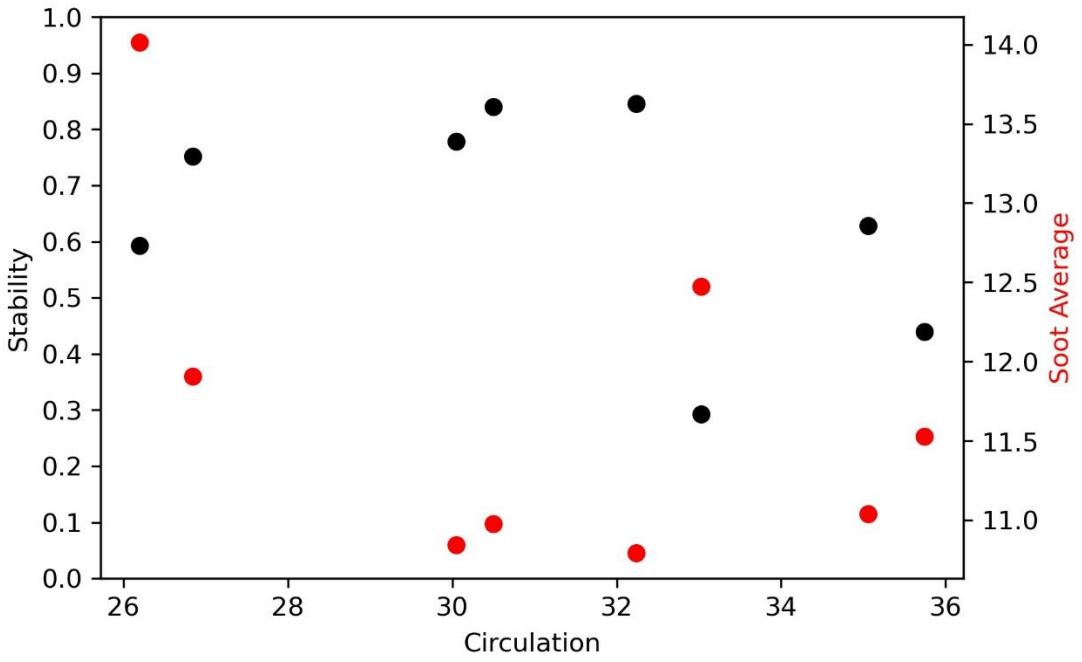

Figure 61: Flame stability and soot production as a function of circulation for n-heptane under back-mid circumferential flow profile conditions with a radial flowrate of 0 slpm.

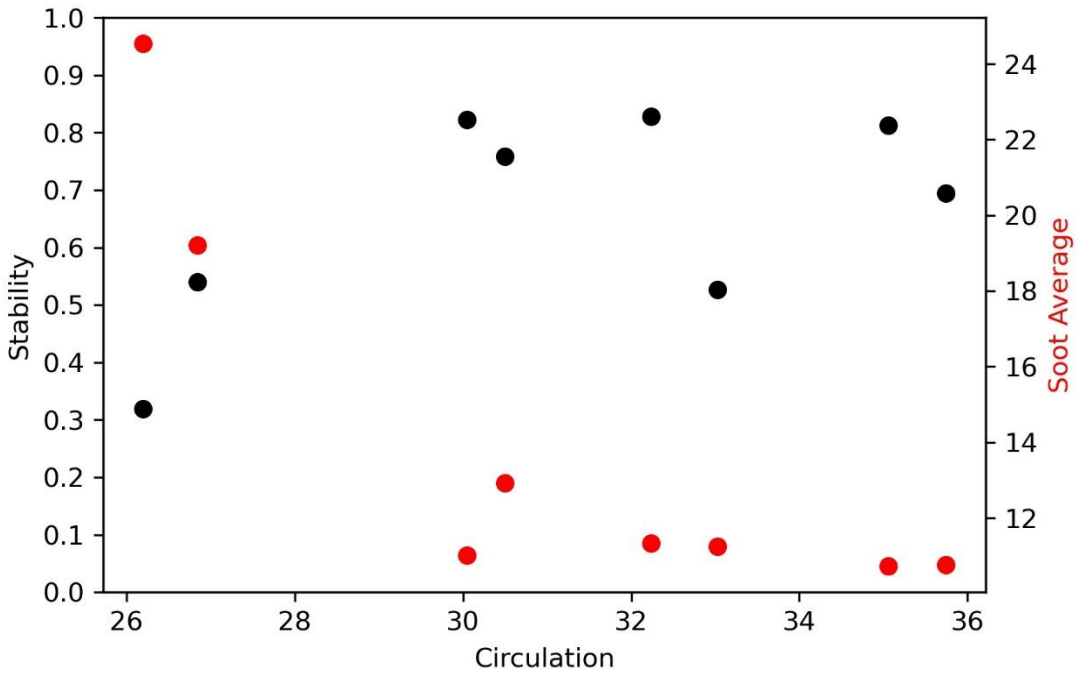

Figure 62: Flame stability and soot production as a function of circulation for n-heptane under back-mid circumferential flow profile conditions with a radial flowrate of 25 slpm.

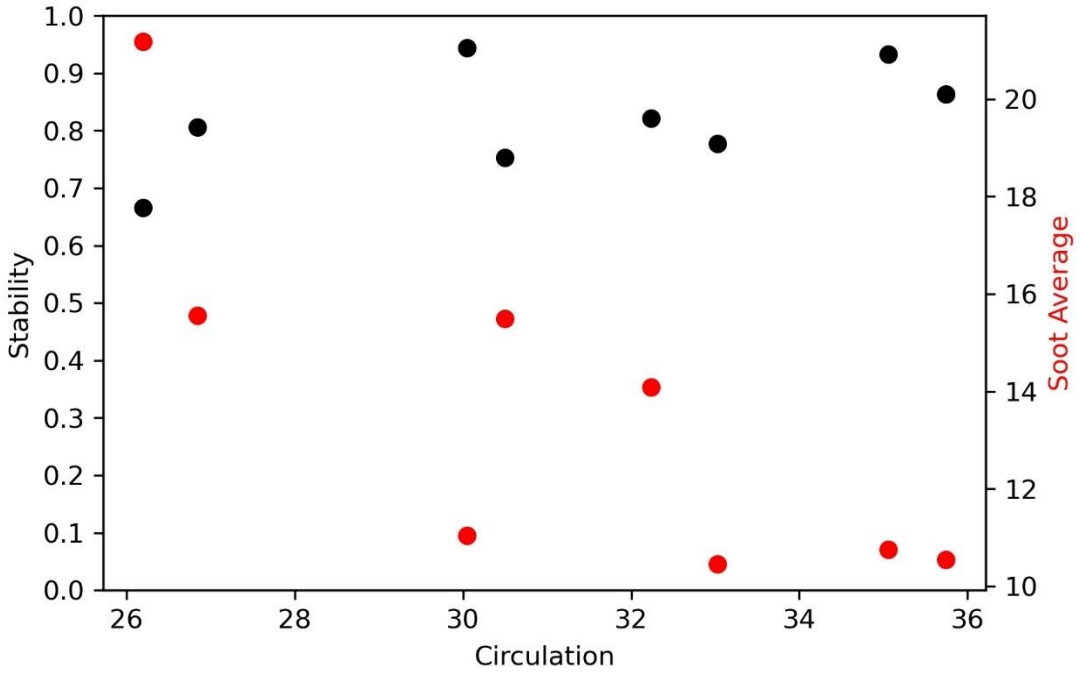

Figure 63: Flame stability and soot production as a function of circulation for n-heptane under back-mid circumferential flow profile conditions with a radial flowrate of 50 slpm.

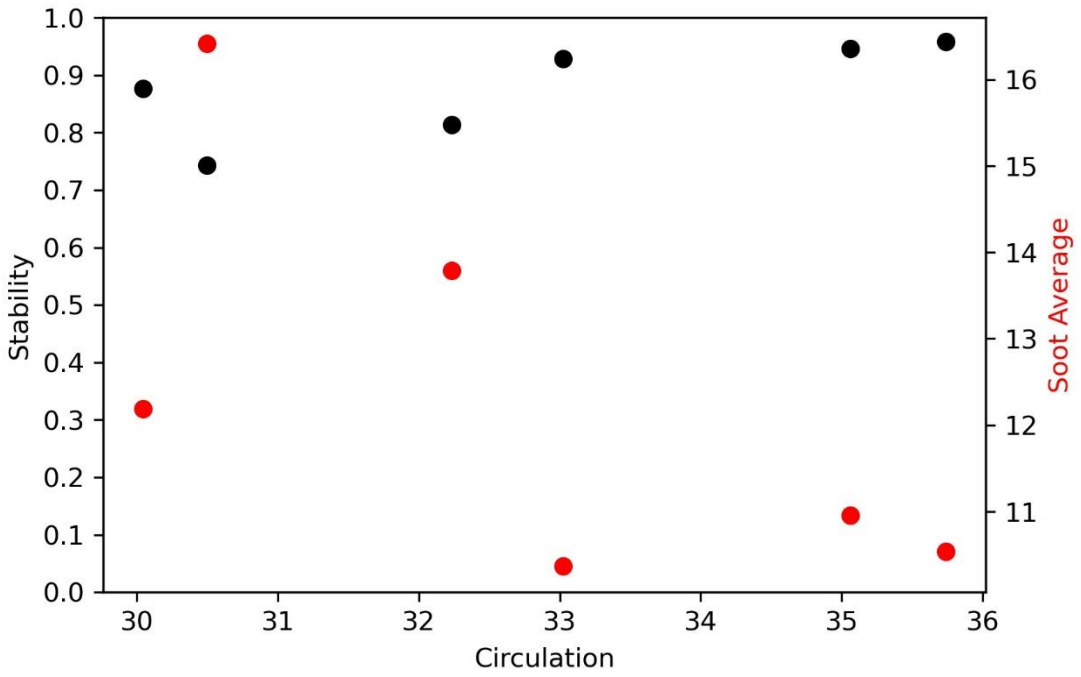

Figure 64: Flame stability and soot production as a function of circulation for n-heptane under back-mid circumferential flow profile conditions with a radial flowrate of 75 slpm.

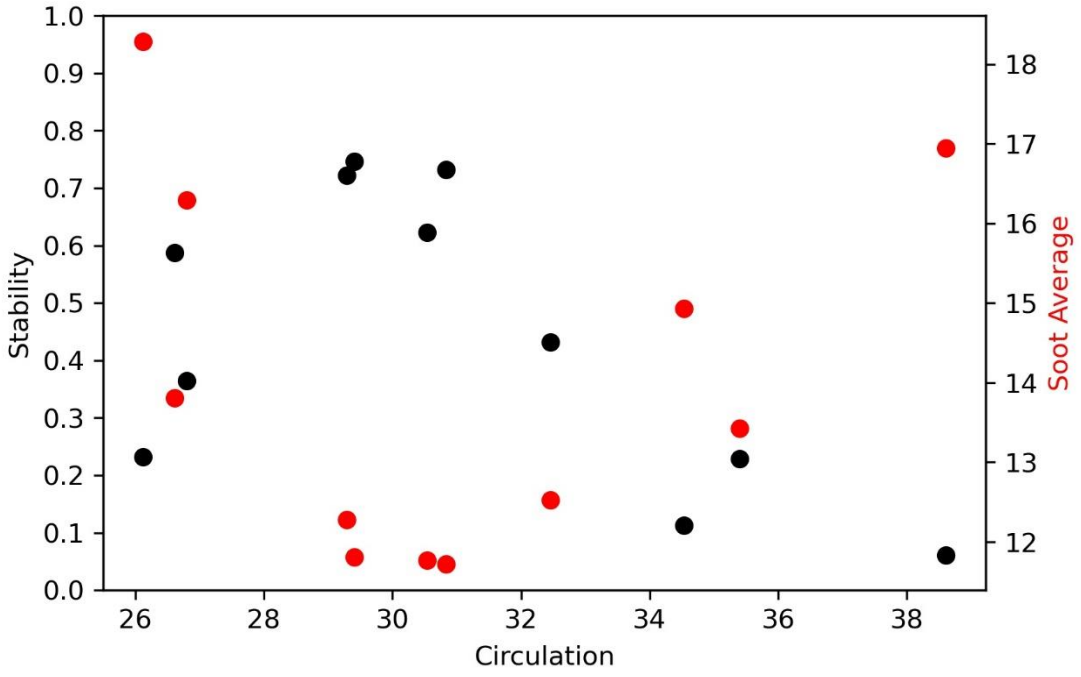

Figure 65: Flame stability and soot production as a function of circulation for n-heptane under back-top circumferential flow profile conditions with a radial flowrate of 0 slpm.

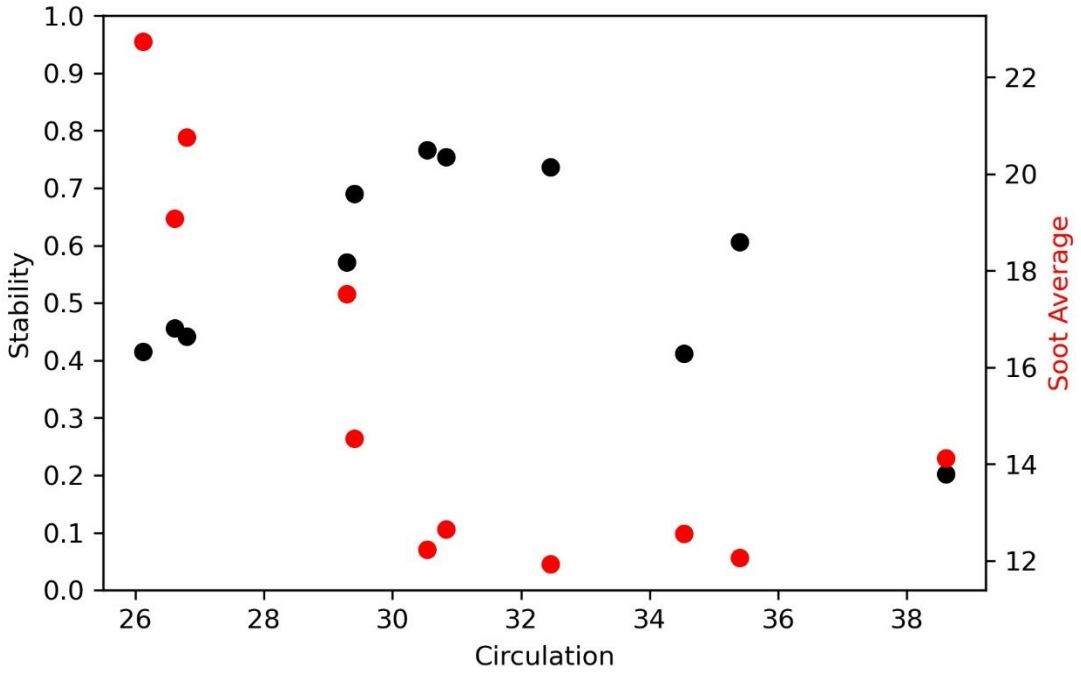

Figure 66: Flame stability and soot production as a function of circulation for n-heptane under back-top circumferential flow profile conditions with a radial flowrate of 25 slpm.

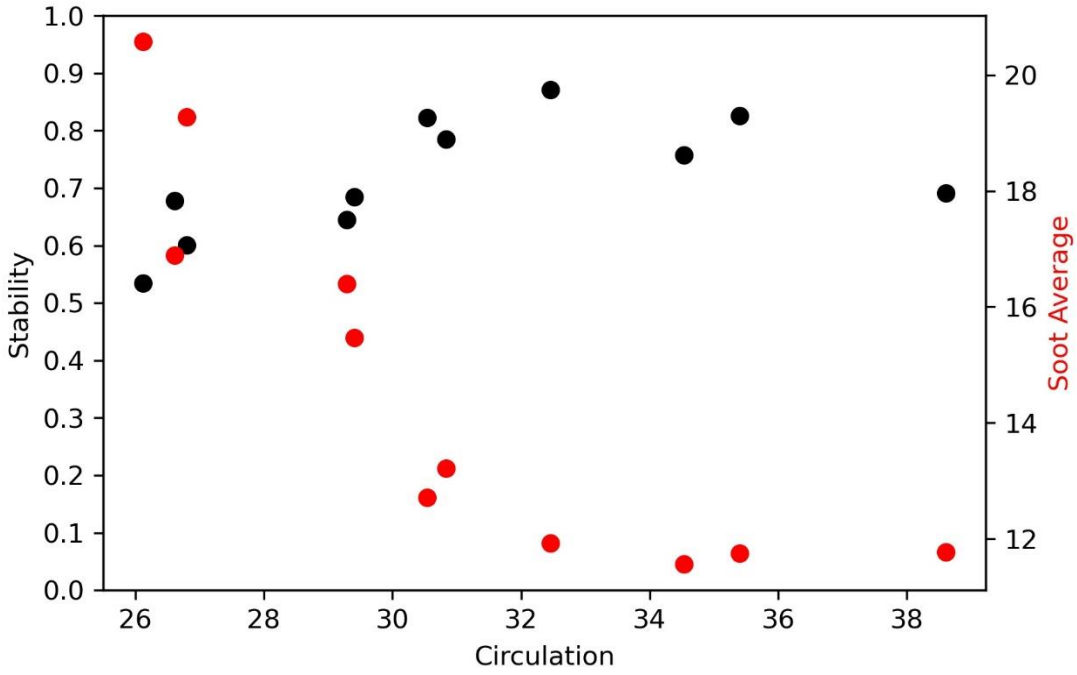

Figure 67: Flame stability and soot production as a function of circulation for n-heptane under back-top circumferential flow profile conditions with a radial flowrate of 50 slpm.

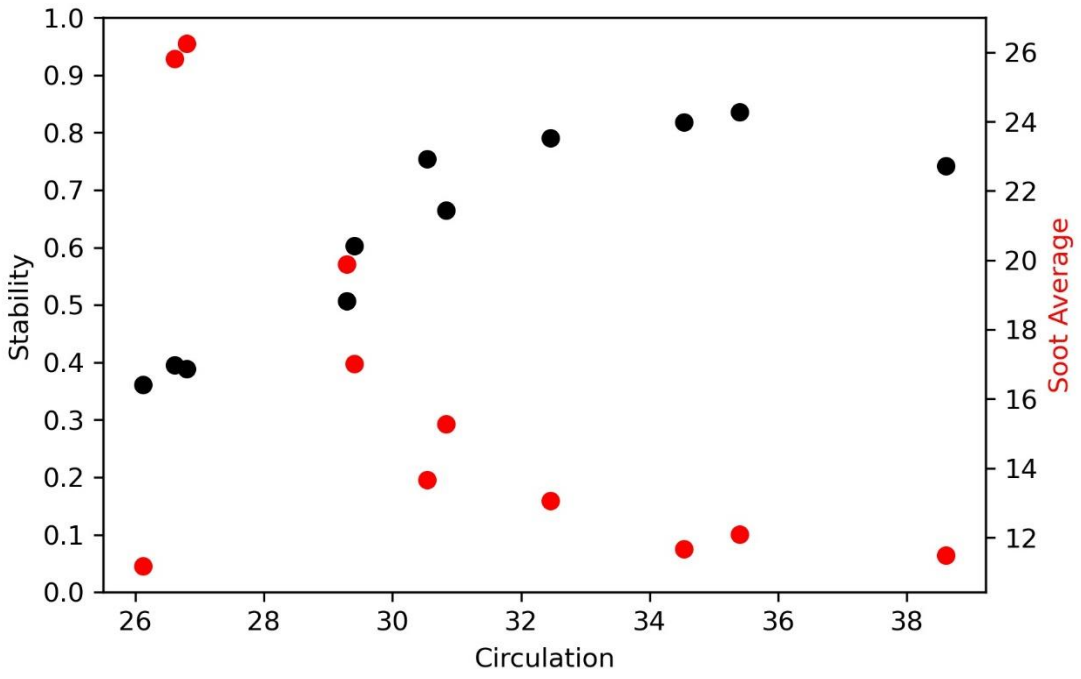

Figure 68: Flame stability and soot production as a function of circulation for n-heptane under back-top circumferential flow profile conditions with a radial flowrate of 75 slpm.

4.5.2 Blue Whirl Stability Hysteresis as a Function of Radial Flowrate and Circulation

Figure 69 and Figure 70 depict blue whirl flame stability and soot production of n-heptane as a function of radial flowrate and circulation for hysteresis testing beginning without and with a whirling flame respectively. These plots illustrate virtually the same result as observed from their circumferential counterparts. Easily notable is the poor flame stability for the hysteresis test beginning with a non-whirling flame. Further, the stability plot for the hysteresis test beginning with a whirling flame indicates similar stability regions and values to that of the measurements taken sweeping from a high to low circulation.

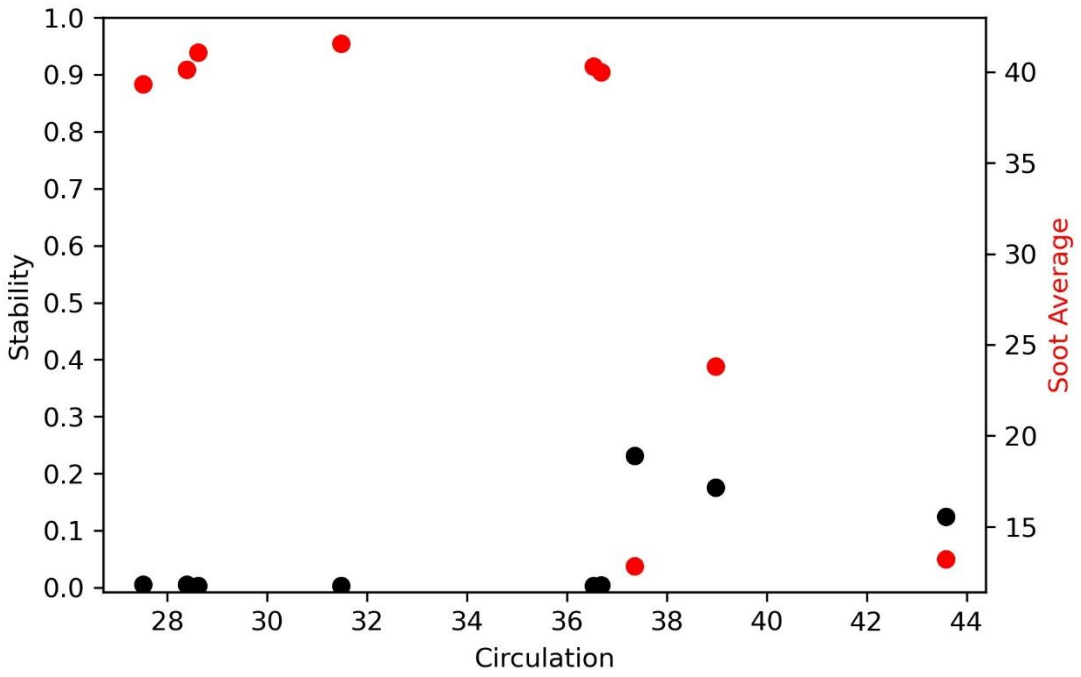

Figure 69: Flame stability and soot production of n-heptane for hysteresis measurements taken at 0 slpm radial flow. Measurement taken sweeping from a low to high circulation. Testing began without an existing whirling flame.

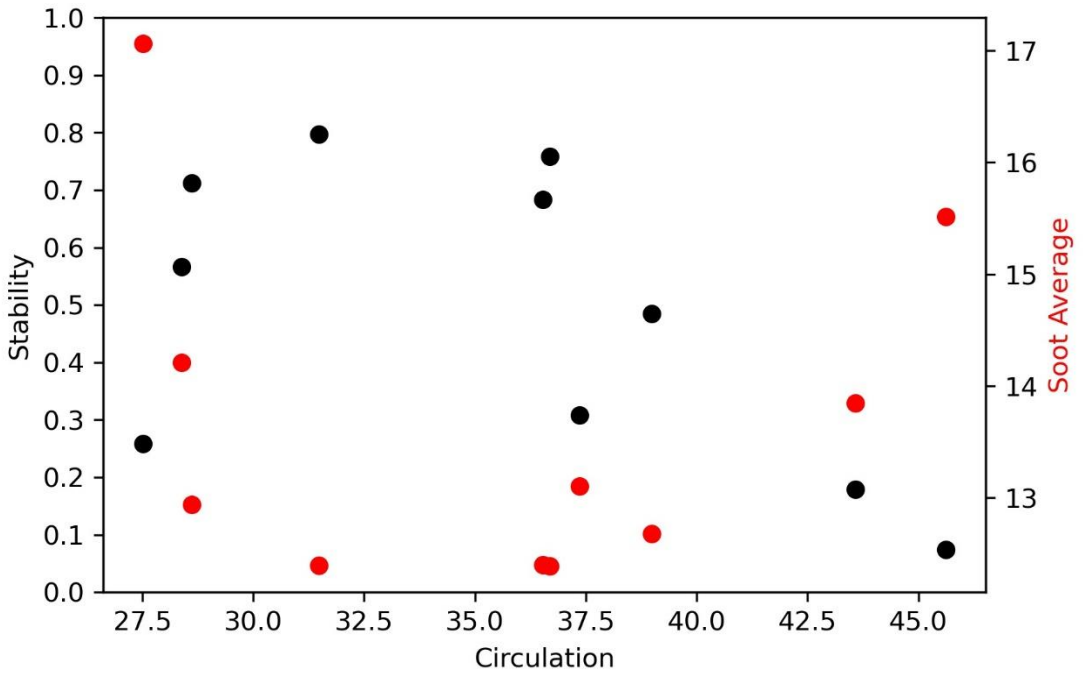

Figure 70: Flame stability and soot production of n-heptane for hysteresis measurements taken at 0 slpm radial flow. Measurement taken sweeping from a low to high circulation. Testing began with an existing whirling flame.

4.5.3 N-Octane and Methyl Acetate Blue Whirl Stability as a Function of Radial Flowrate and Circulation

Figure 71 and Figure 72 show the stability contour plots as a function of circulation and radial flow rate for n-octane and methyl acetate respectively. Figure 73-80 show the 2D stability and soot production behavior for n-octane and methyl acetate as a function of circulation and radial flowrate. These plots illustrate similar behavior to their circumferential counterparts. Akin to the circulation plots for n-heptane, they hint at a specific cutoff point for circulation that, once reached,

transitions the whirling flame into a blue whirl. Again, further refinement will be required to verify these findings.

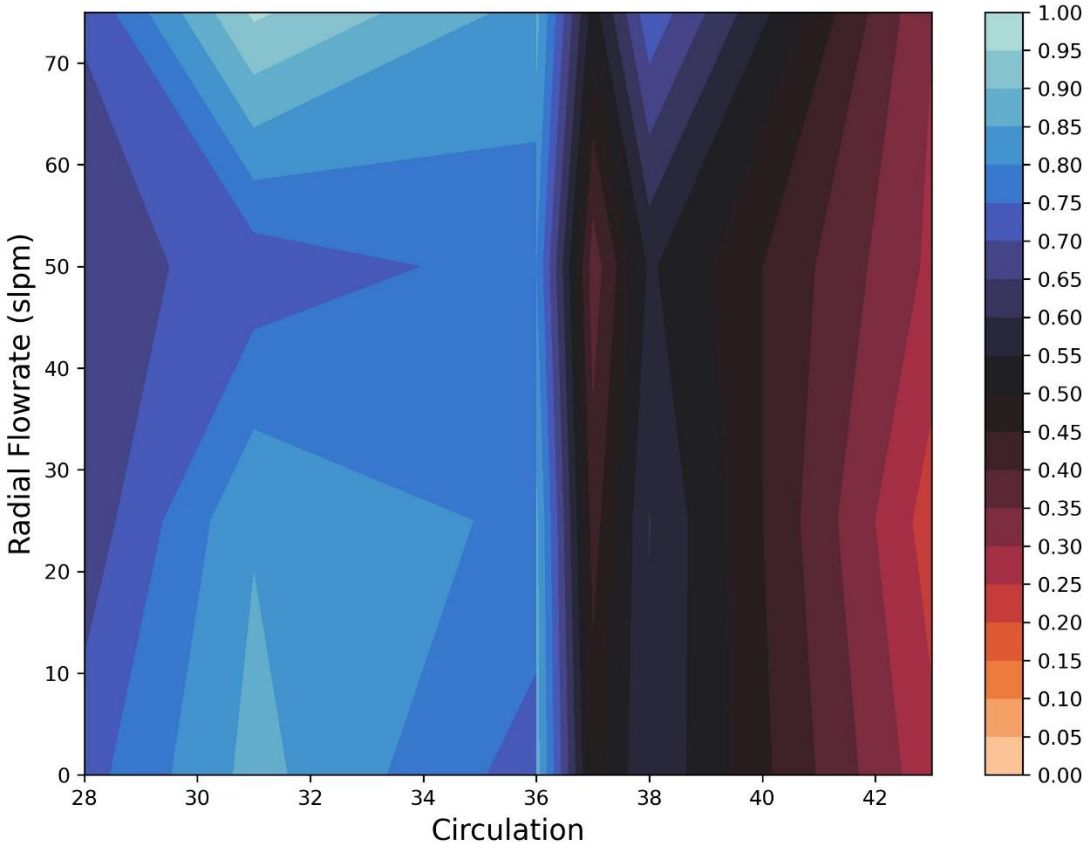

Figure 71: Flame stability of n-octane for back-bot flow profile configuration as a function of radial flowrate and circulation.

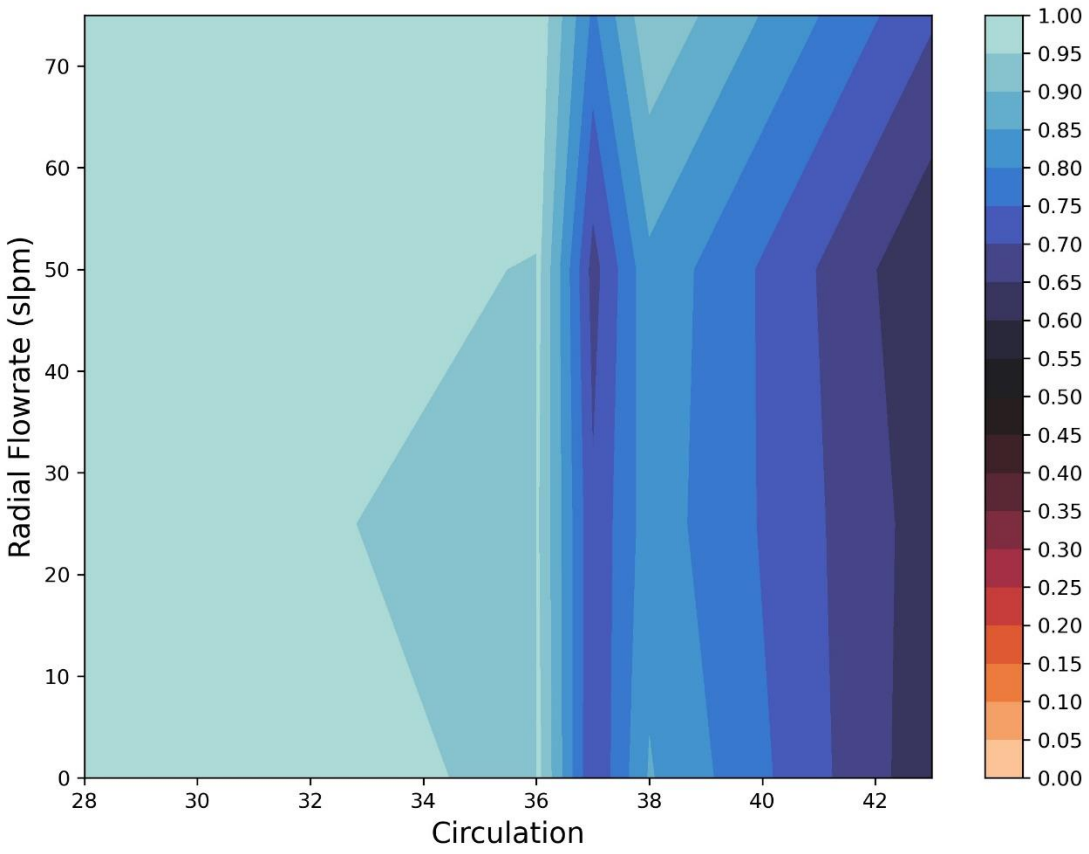

Figure 72: Flame stability of methyl acetate for back-bot flow profile configuration as a function of radial flowrate and circulation.

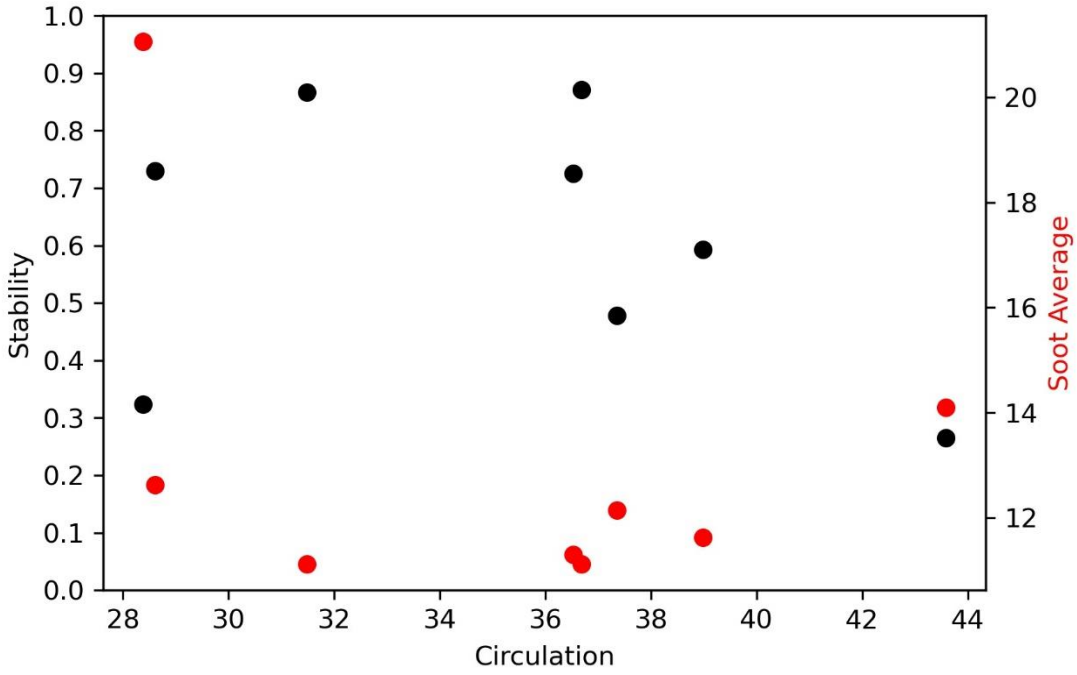

Figure 73: Flame stability and soot production as a function of circulation for n-octane under back-bot circumferential flow profile with a radial flowrate of 0 slpm.

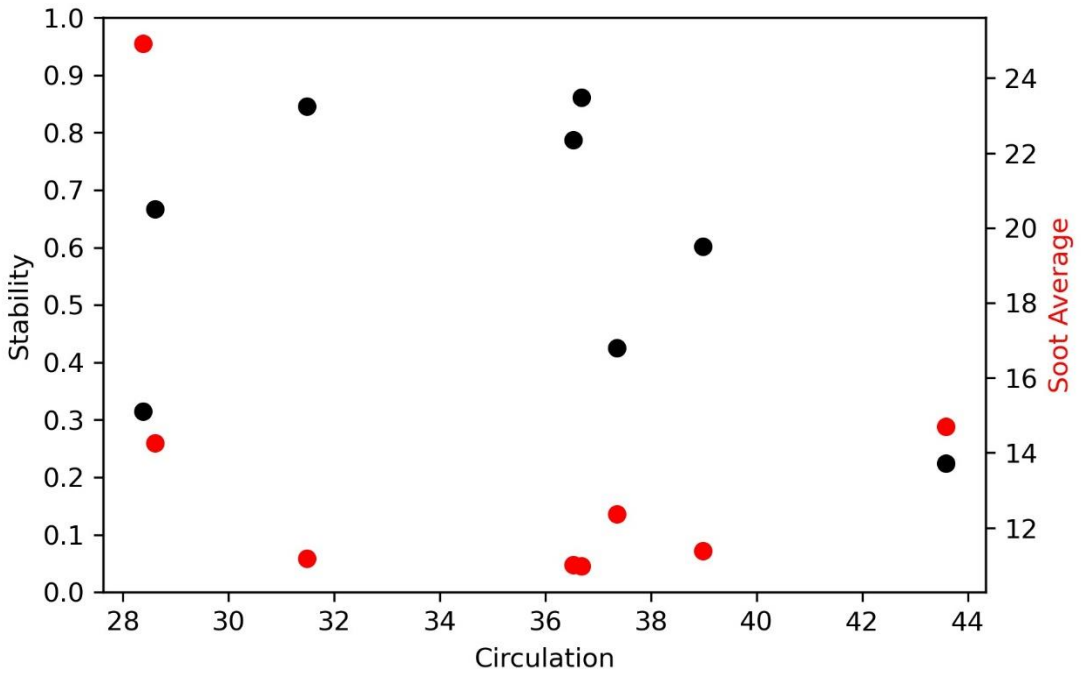

Figure 74: Flame stability and soot production as a function of circulation for n-octane under back-bot circumferential flow profile with a radial flowrate of 25 slpm.

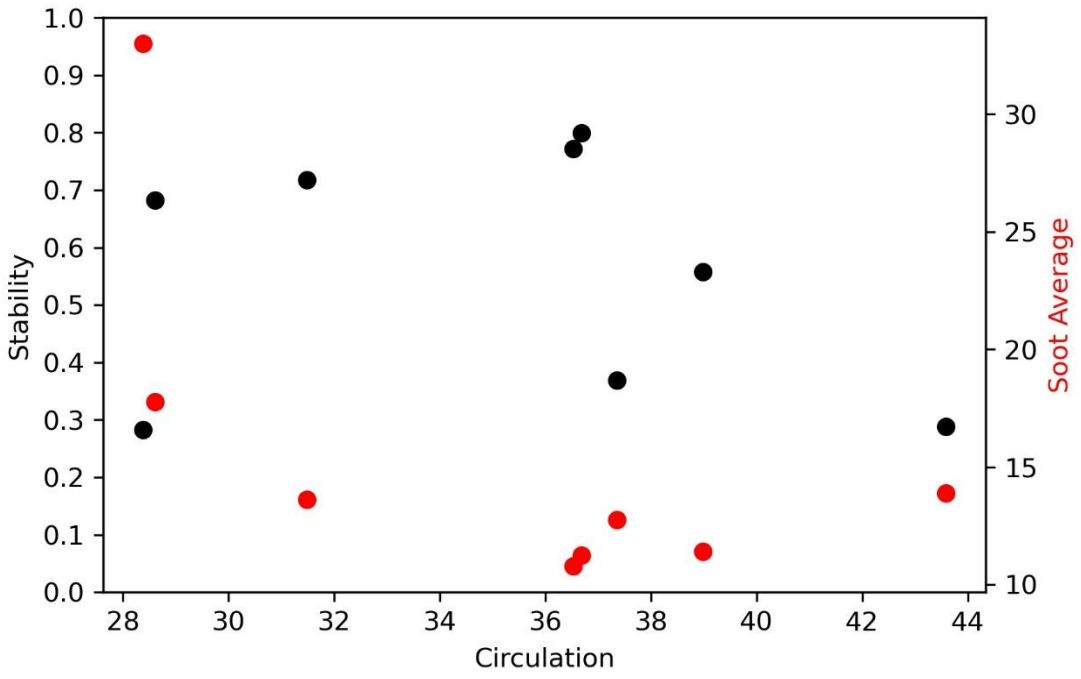

Figure 75: Flame stability and soot production as a function of circulation for n-octane under back-bot circumferential flow profile with a radial flowrate of 50 slpm.

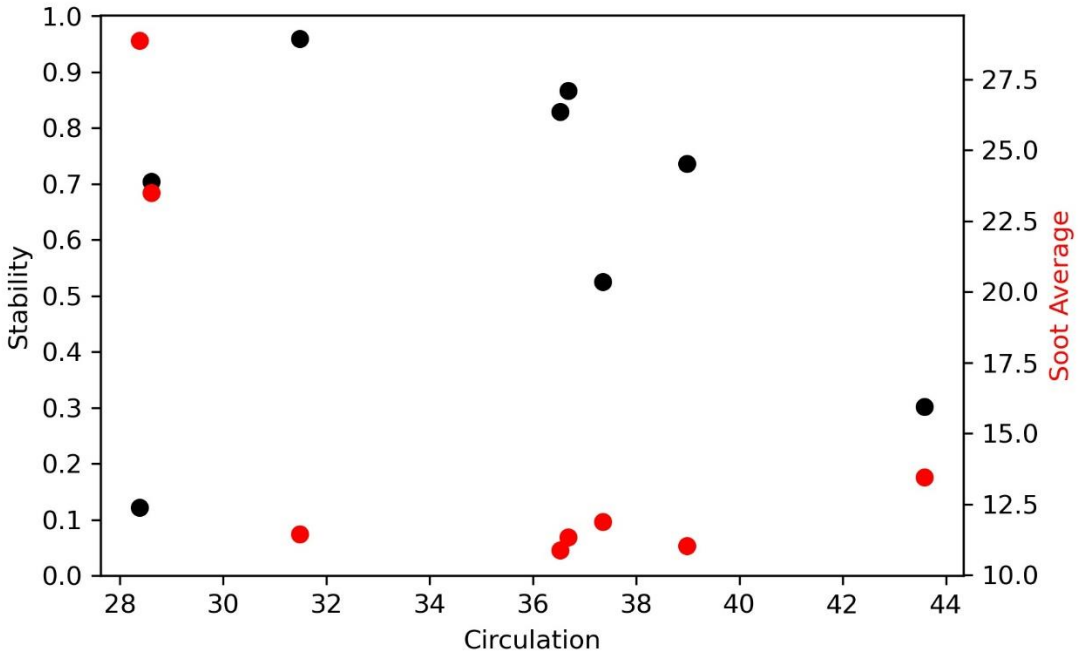

Figure 76: Flame stability and soot production as a function of circulation for n-octane under back-bot circumferential flow profile with a radial flowrate of 75 slpm.

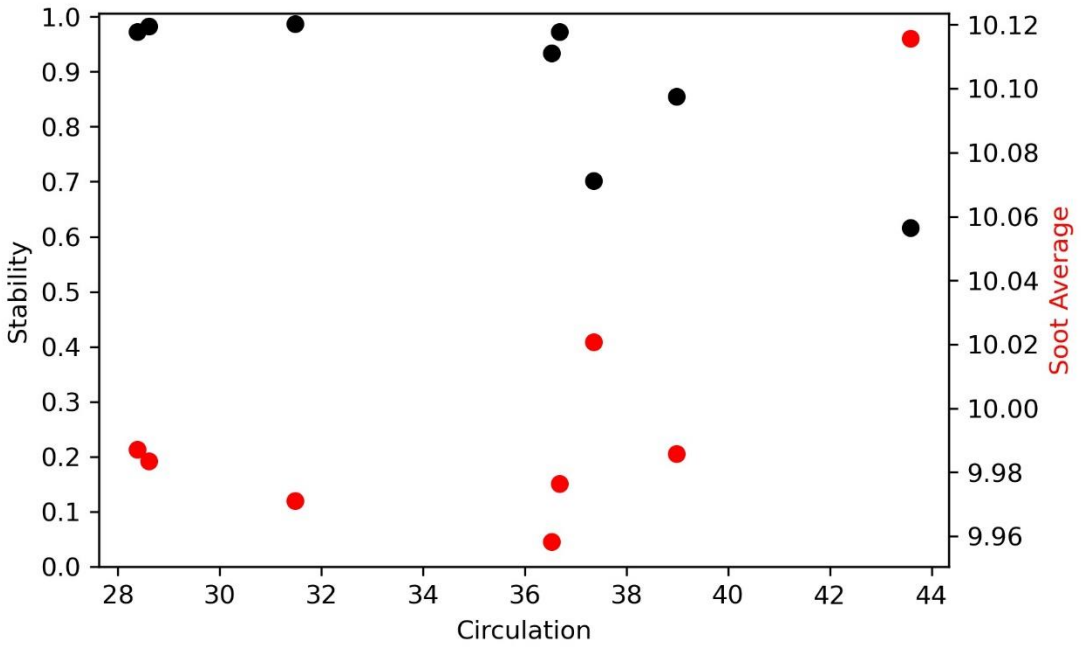

Figure 77: Flame stability and soot production as a function of circulation for methyl acetate under back-bot circumferential flow profile with a radial flowrate of 0 slpm.

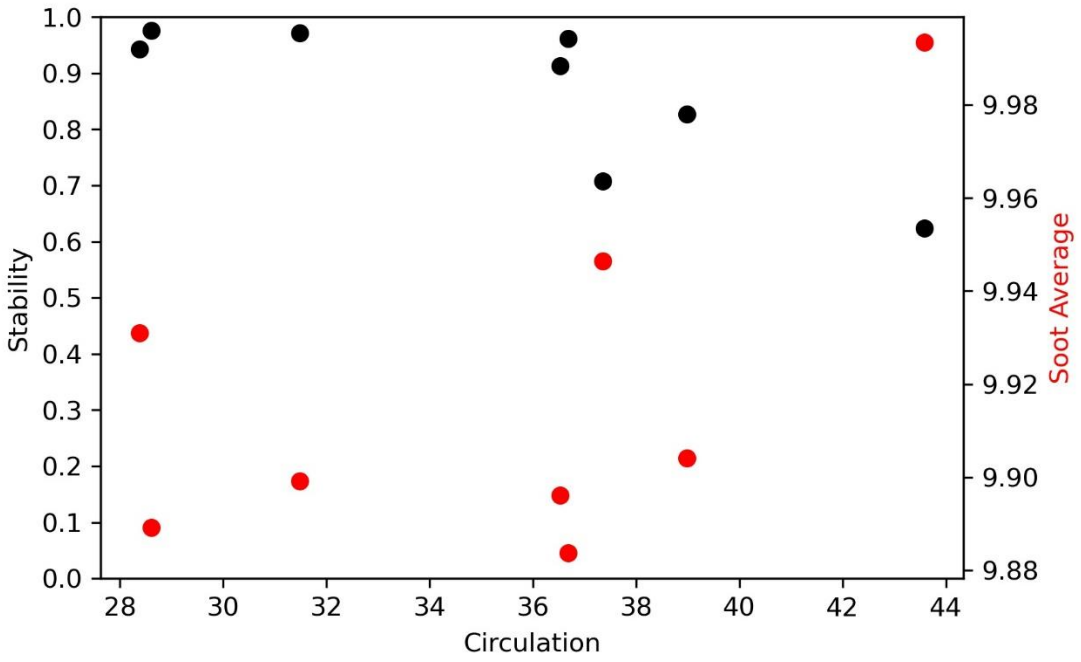

Figure 78: Flame stability and soot production as a function of circulation for methyl acetate under back-bot circumferential flow profile with a radial flowrate of 25 slpm.

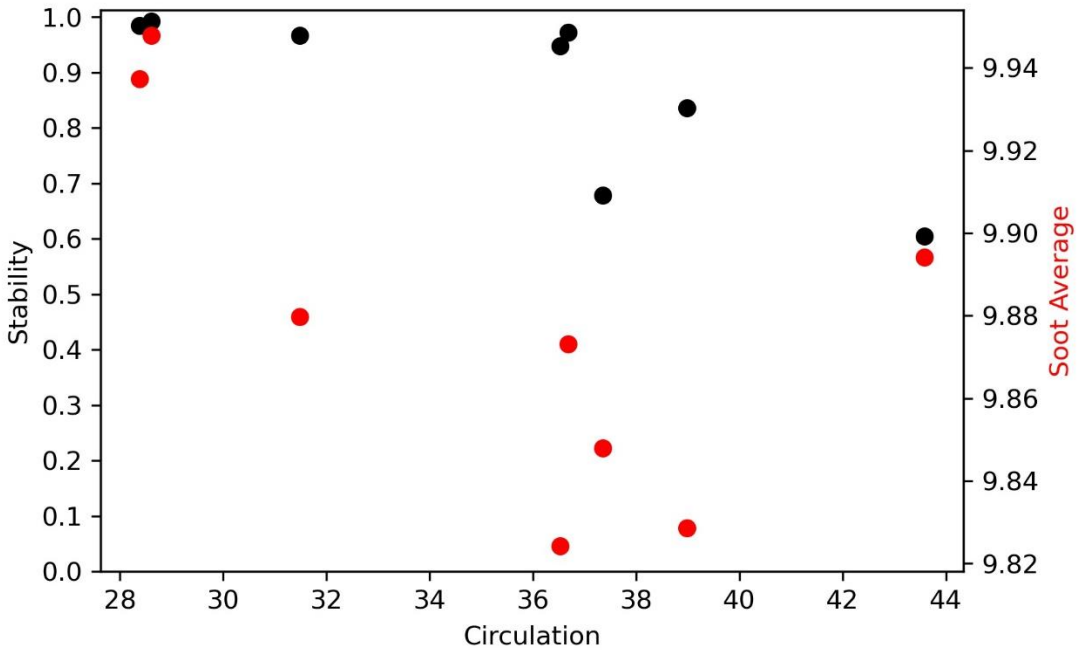

Figure 79: Flame stability and soot production as a function of circulation for methyl acetate under back-bot circumferential flow profile with a radial flowrate of 50 slpm.

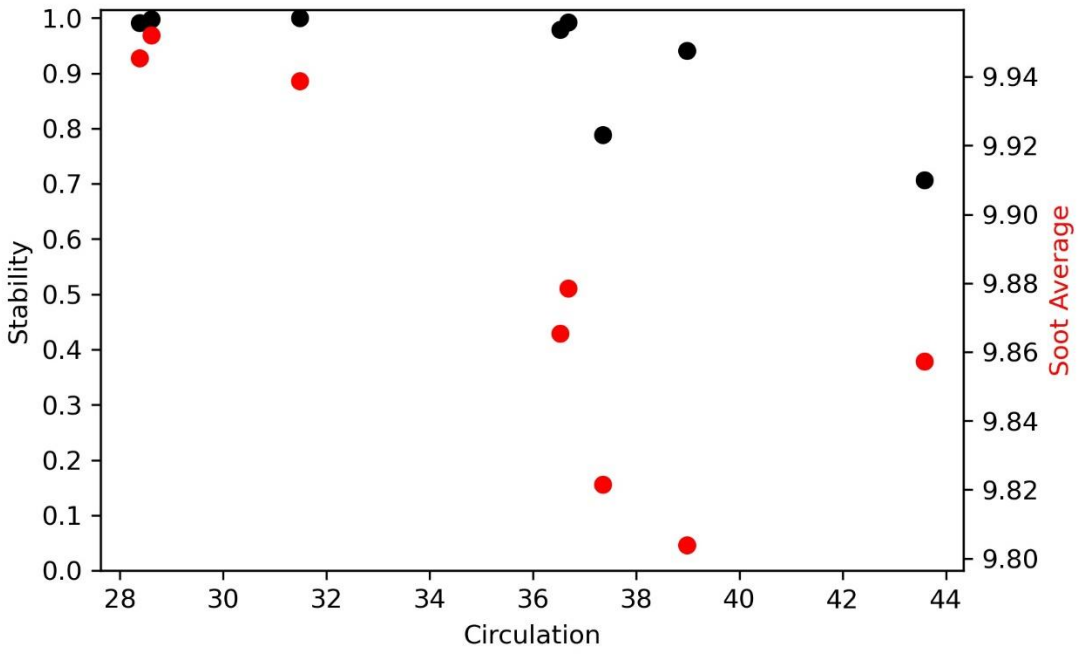

Figure 80: Flame stability and soot production as a function of circulation for methyl acetate under back-bot circumferential flow profile with a radial flowrate of 75 slpm.

Chapter 5: Conclusion

5.1 Summarized Results

5.1.1 Advanced Experimental Apparatus

In order to experiment with more finite control over independent variables, an advanced experimental apparatus was designed and fabricated. Independent variables that were designed for included:

- Fuel type
- Fuel flow rate
- Burner size
- Radial flowrate
- Circumferential flowrate
- Circumferential flow profile
- Burning surface or baseplate temperature
- Air temperature

Although not all independent variables were explored in this study, designing for each of them ensures that the burner will be sufficient for future studies interested in measuring the effect of the these variables. In particular, the advanced experimental apparatus offers a significant advantage over the previous buoyancy induced flow burner. With forced air induction, an experimentalists can observe changes to the flame with small incremental flow adjustments. Additionally, these

flowrates can be set indefinitely and independent of flame regime (no shift in circumferential flowrate due to transition from a fire whirl to blue whirl, for example). Further, the design is readily modifiable. Standard materials, with the exception of the custom quartz glass, were used to keep cost of material and manufacturing low. By nature of the design, the experimental apparatus can be scaled to larger and smaller sizes according to laboratory requirements and material constraints.

The incorporation of optical access also allows for ease of use and measurement. With parallel outer and inner enclosure viewing windows, post-processing data for measurement systems that rely on lasers and optics such as PLIF and PIV is made significantly easier compared to the curved optical access to that of the preliminary burner and work done in [19].

5.1.2 Image Processor

The image processor, scripted in Python, provides a fast and effective means of analyzing captured images. The post-processor keys on the signature characteristic of the blue whirl, the lifted blue rim [2]. The post-processor interacts with the images in six steps. It performs each step by:

1) Reading in the raw image
2) Cropping the image to the desired region of interest and identifying the vertical location of the burning surface in the image

a. Capturing the average red channel intensity of the image for soot calculation

3) Masking the image, in grayscale, with a lower and upper bound
4) Running a canny edge detection algorithm
5) Dilating the canny edges to ensure continuity of edges
6) Drawing a bounding box around the longest continuous edge and evaluating flame shape and position.

The post-processor uses the lifted blue rim for flame identification by drawing the bounding box around the flame. If the box extends to the burning surface, enough light must be present at the burning surface, indicating combustion on the burning surface. This would indicate a non-lifted flame or, in other words, a non-blue whirl. Conversely, if the bounding box does not extend to the burning surface, the flame must be lifted and is identified as a blue whirl accordingly. The post-processor outputs the results of each image, storing a CSV file that retains the image name, flame size, and flame state (blue whirl or not blue whirl). For the given conditions (flow profile configuration, burning surface temperature, radial flowrate, circumferential flowrate, etc.), a stability value and soot production value are calculated and stored.

5.1.3 Experimental Results

This study presents the results of four experiments: (1) effect of circumferential flow profile on blue whirl flame stability and soot production; (2)

effect of flame state (whirling flame, or non-whirling flame) on blue whirl formation; (3) effect of fuel type on blue whirl flame stability and soot production; and (4) effect of fuel flow on flame stability and soot production.

To test (1), n-heptane was run for a range of radial and circumferential flowrates against three different flow profiles depicted in Figure 12, Figure 13, and Figure 14. The results are presented in the form of 2.5D contour plots and individual 2D plots, showing the relationship of flame stability and soot production to radial and circumferential flow. These results present two key findings: (1) all tested flow profiles were able to produce a blue whirl, albeit at different circumferential flowrate ranges – this hints that there is a critical height at which the circumferential flow impacts the flame; and (2) the trend of stability as a function of circumferential and radial flowrate seems to agree with the findings of [26] – as radial flow, assumed to convert into axial flow at the flame, increases, to maintain the circulation dominated flow, circumferential flowrate must increase. This trend is extremely evident for both the back-mid and back-top flow profile configurations.

To test (2), blue whirl stability and soot production were measured while sweeping circumferential airflow from low to high (240 -400 slpm). The experiment was performed twice with two different initial conditions. For the first sweep, the flame began as a pool fire. For the second sweep, the flame began as a whirling flame. The two initial conditions presented vastly different results. The sweep beginning with a pool fire did not begin to transition to a blue whirl until a much higher circumferential flowrate. The sweep beginning with a whirling flame produced

results that were very similar to the previous measurements taken sweeping from a high to a low circumferential flowrate. This hysteresis is very similar to the hysteresis seen in [42], [43]. Further, this hysteresis in formation may be why the blue whirl has only been formed after transitioning from a fire whirl.

To test (3), the stability sweep for the back-bot flow profile configuration was performed again for n-octane and methyl acetate. N-octane presented results akin to the results found for n-heptane in Section 4.1. This supported the hypothesis that stability ranges, as a function of radial and circumferential flowrate, would remain the same for any fuel given a fixed HRR. Methyl actetate, however, showed significantly different results and presented a more stable blue whirl across a wider range of circumferential and radial flowrates. A potential explanation for the change in results is mass flux into the flame, explained via the Stefan problem. Most notably, these results indicate that there is more to blue whirl formation and stability than the non-dimensionalized ratio of circulation to buoyancy.

To test (4), the blue whirl was formed using the standard procedure detailed in Section 3.4. Fuel flow rates between 0.2 ml/min and 1.3 ml/min were tested. These limits were chosen because below 0.2 ml/min, flame extinction was observed. Above 1.3 ml/min, a very sooty and unstable transition whirl was observed. First, the fuel flow rate was increased from 0.2 ml/min to 1.3 ml/min. Then, the fuel was flow rate was decreased from 1.3 ml/min to 0.2 ml/min. Both flame stability and soot production were measured. Results shown in Figure 52 and Figure 53 indicate no

hysteresis effects in blue whirl stability or soot production as a function of fuel flow rate.

Lastly, to visualize the data as a function of radial flowrate and circulation, all figures were reproduced. By and large, the circulation plots reinforced the findings described for experiments (1)-(4). Critical points for blue whirl formation and stability were observed, and the sharp drop off in blue whirl stability at a low circulation value was repeated. This dramatic shift may be explained by the non-linearly varying velocity at the selected height of 0.5" above the burning surface. Further refinement will be required to verify these findings and observed locations of instability.

5.2 Future Work

Although several fundamental questions have been addressed regarding the blue whirl, further work is needed to understand the core mechanisms of the flame. A study that includes higher resolution of circulation would provide data that is more comparable to existing literature, particularly that of the results presented in [26]. There are also many more of experiments that the advanced burner, detailed in 3.1, is capable of performing. These include:

- Effect of a smaller burner diameter (impact of boundary layer presence near flame)
- Effect of imposed internal pressure to the combustion chamber
- Effect of air temperature

- PIV measurements of the flow field

These measurements would aid in experimental validation of numerical simulations, such as those presented in [20], [24]. Further, these results may aid in the production practical energy conversion system. With increasing efficiency of Stirling engines and thermal electric devices, an efficient, fuel flexible technology that produces significantly lower noise pollution may be useful for changing emissions and energy constraints.

Appendices

A.1 Velocity Plots for the Three Circumferential Flow Profile Configurations at Given Flowrates

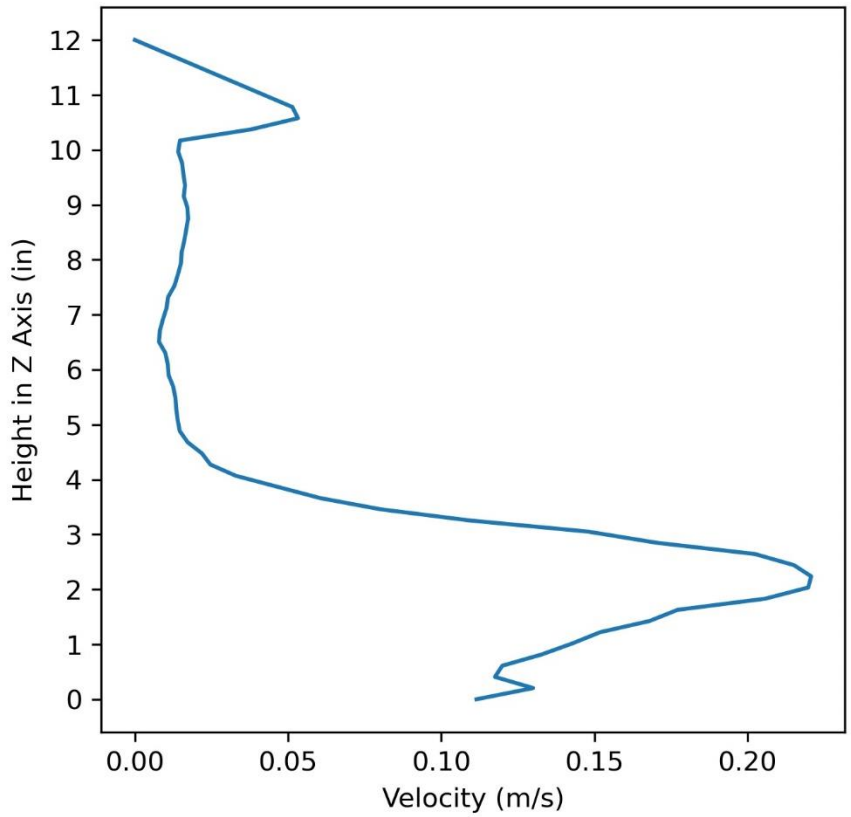

Figure 81: Bot-back port, 60 slpm Flowrate

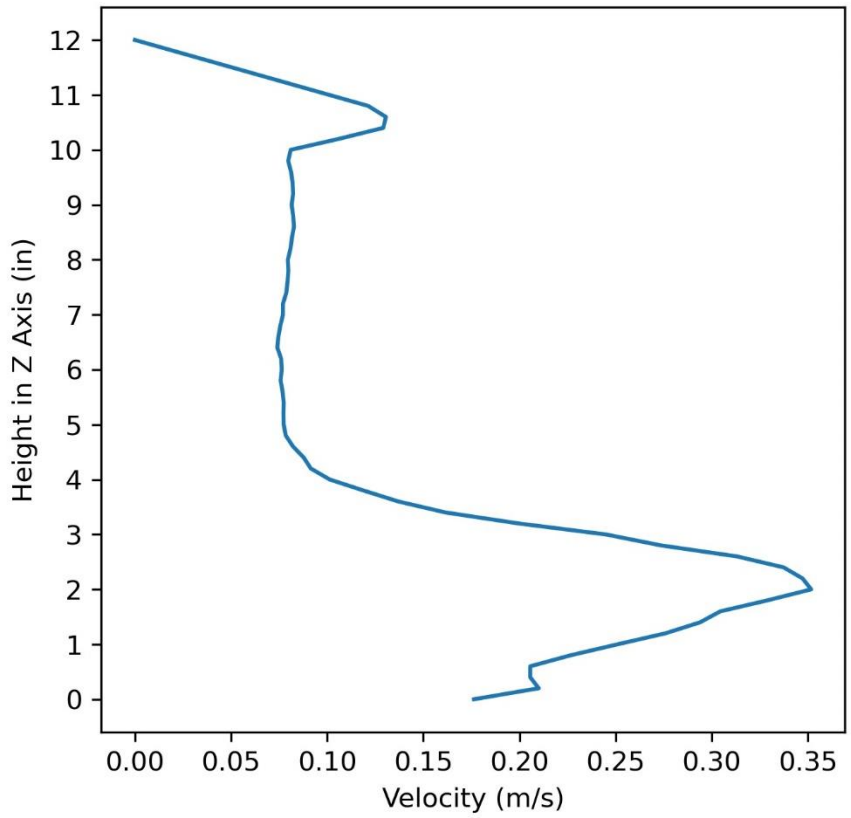

Figure 82: Bot-back port, 65 slpm Flowrate

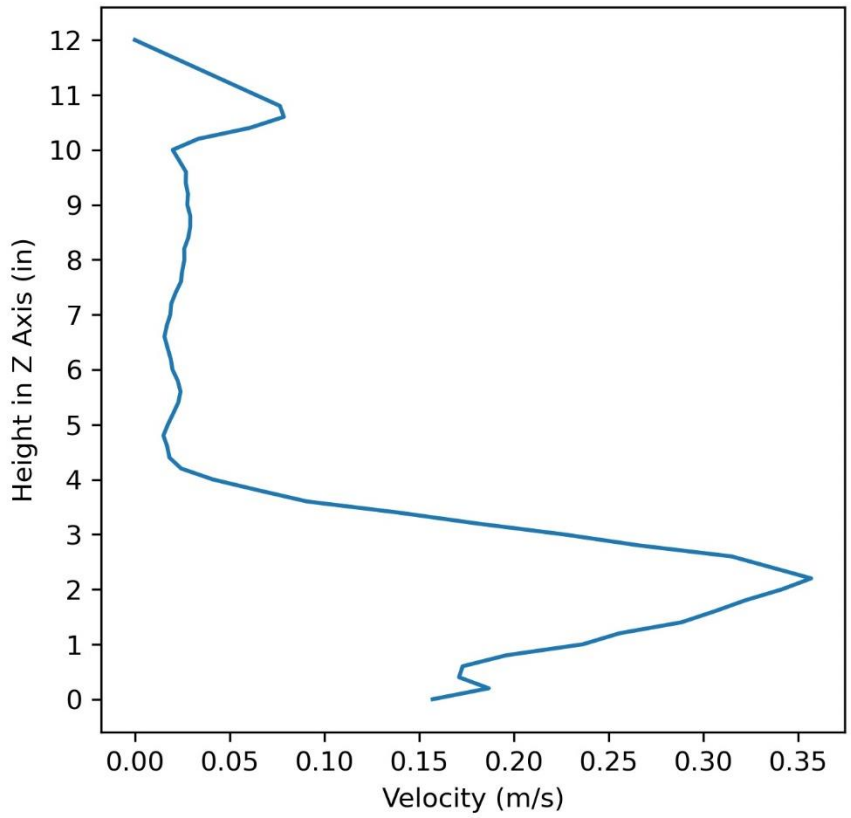

Figure 83: Bot-back port, 70 slpm Flowrate

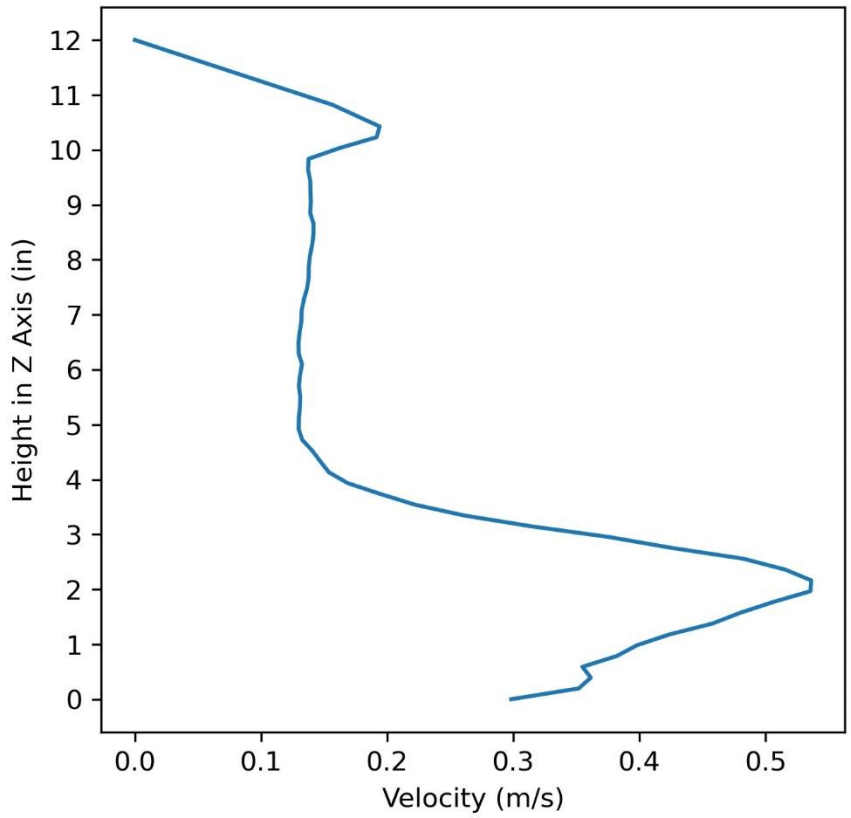

Figure 84: Bot-back port, 75 slpm Flowrate

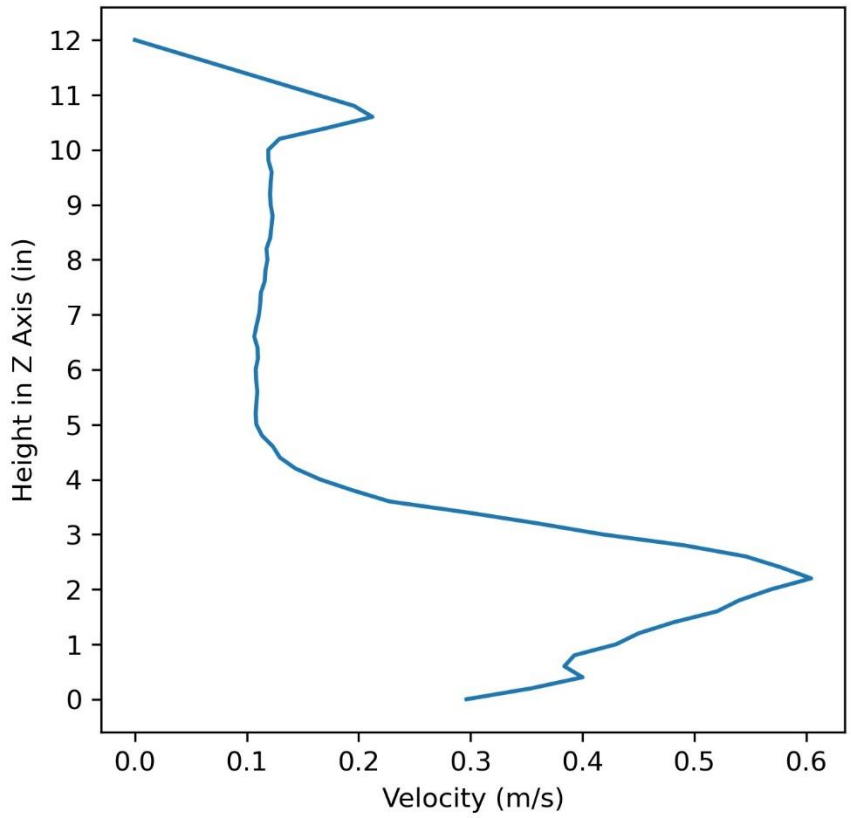

Figure 85: Bot-back port, 80 slpm Flowrate

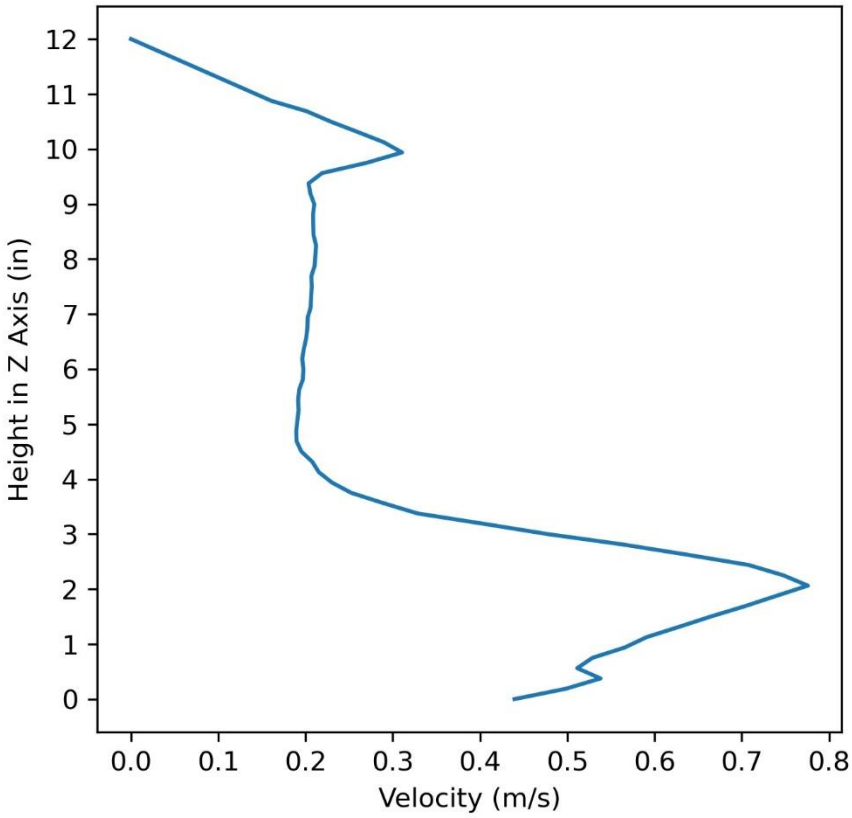

Figure 86: Bot-back port, 85 slpm Flowrate

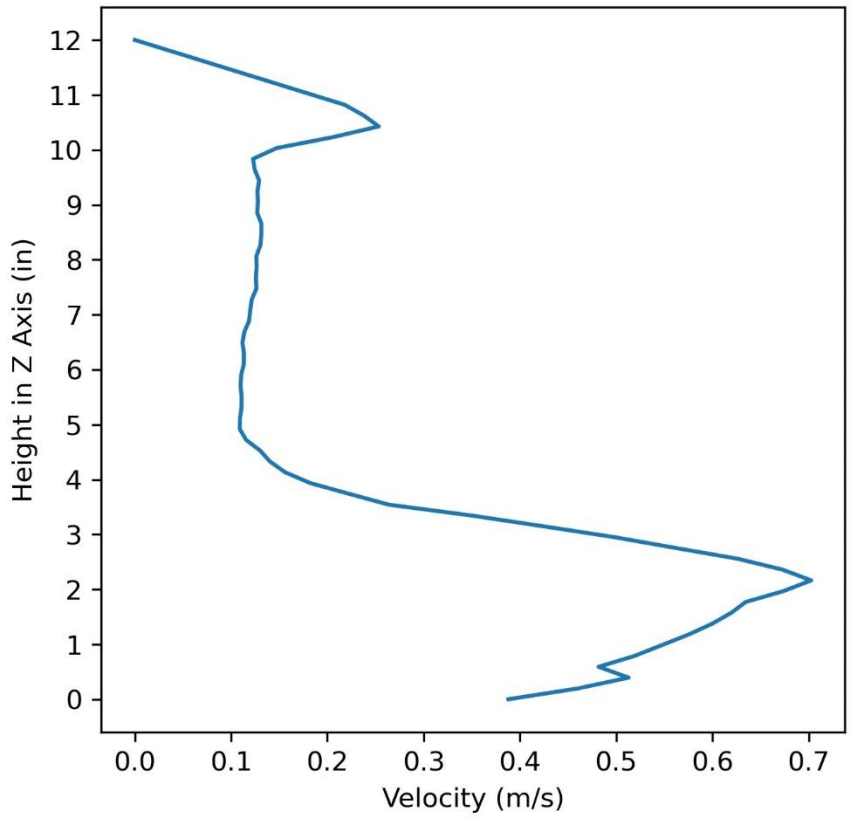

Figure 87: Bot-back port, 90 slpm Flowrate

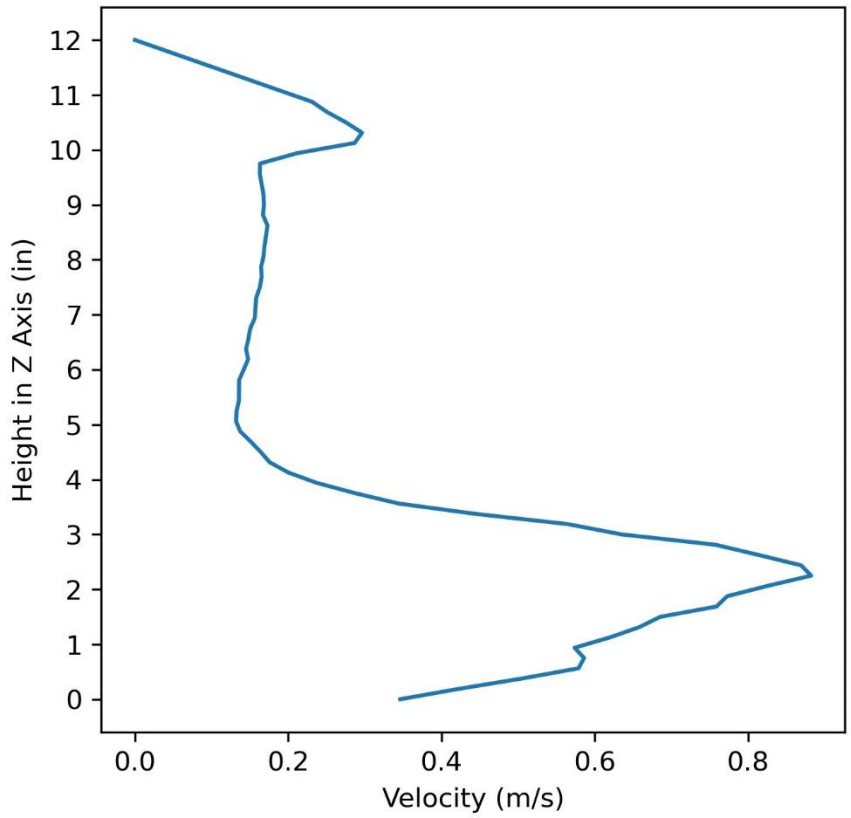

Figure 88: Bot-back port, 95 slpm Flowrate

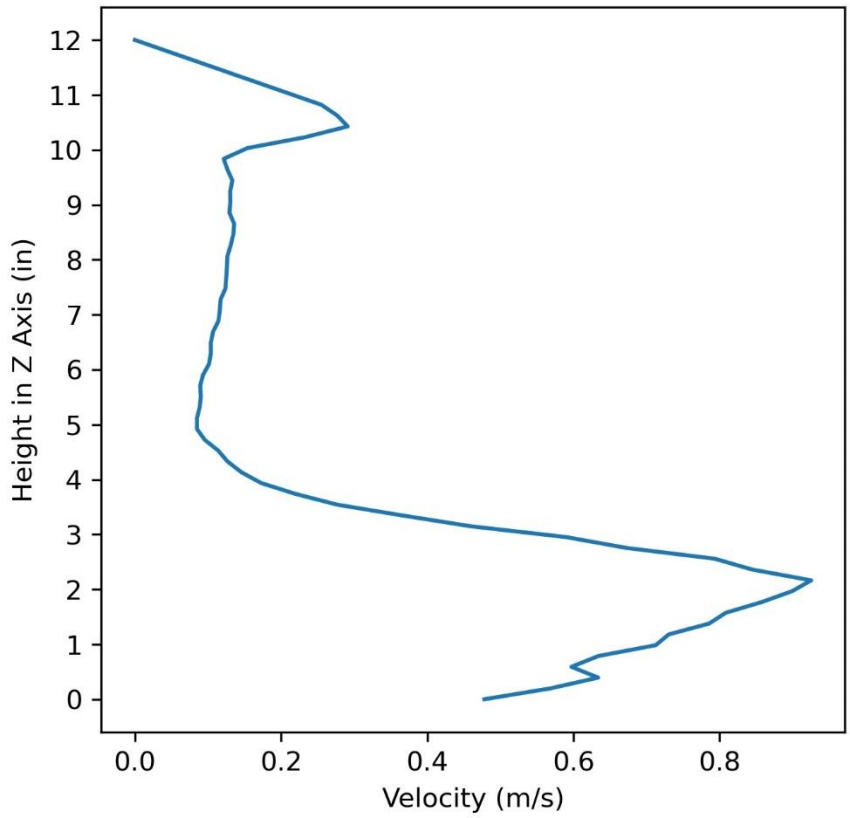

Figure 89: Bot-back port, 100 slpm Flowrate

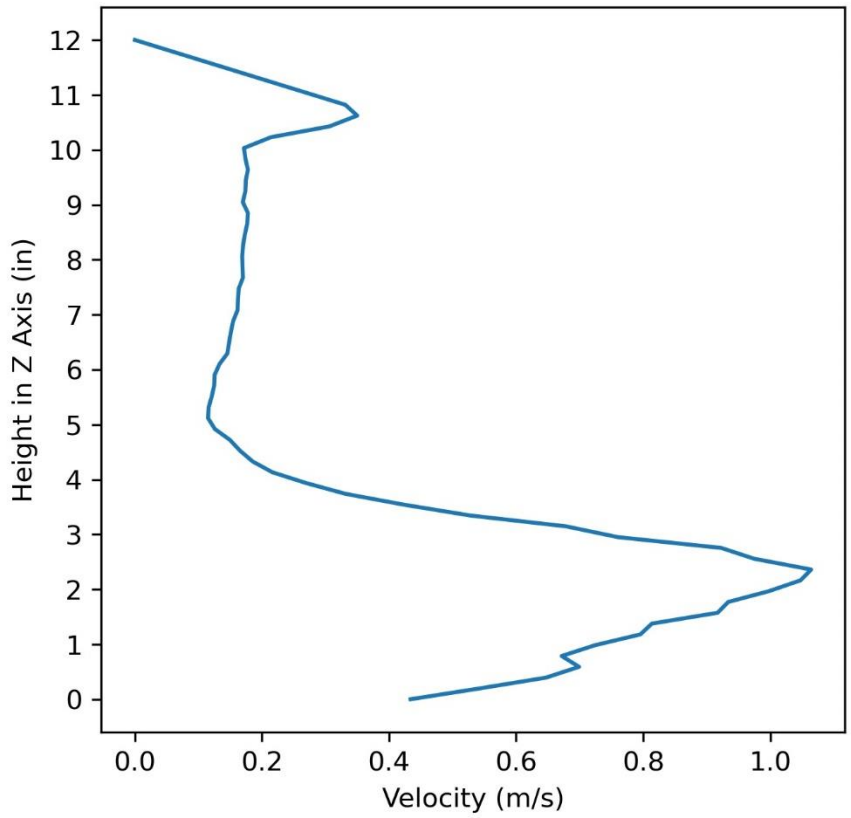

Figure 90: Bot-back port, 105 slpm Flowrate

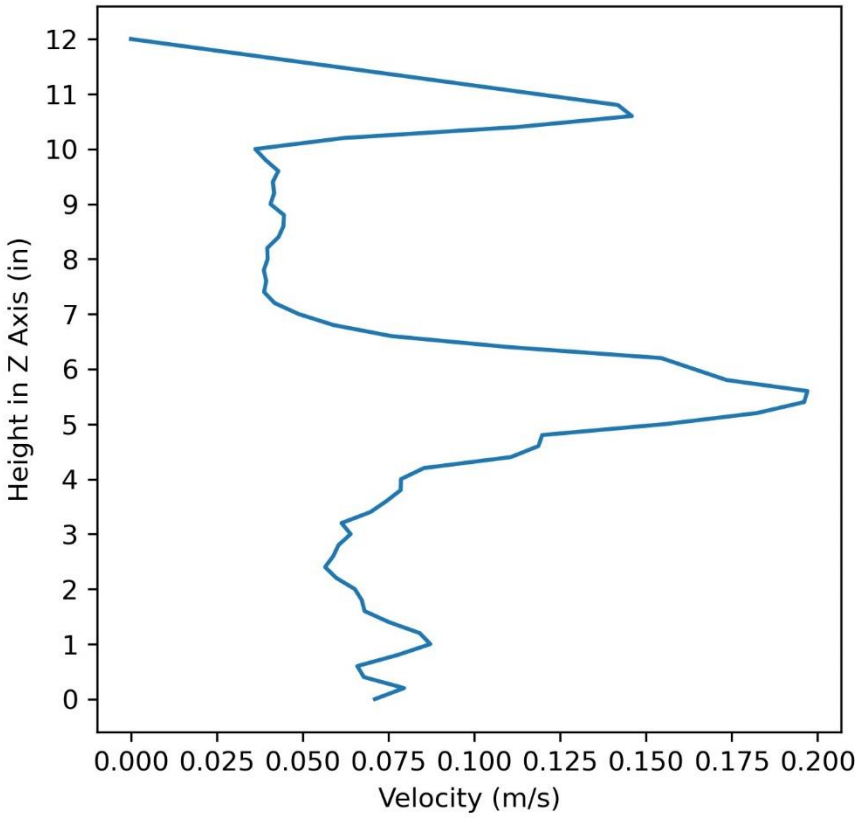

Figure 91: Mid-back port, 75 slpm

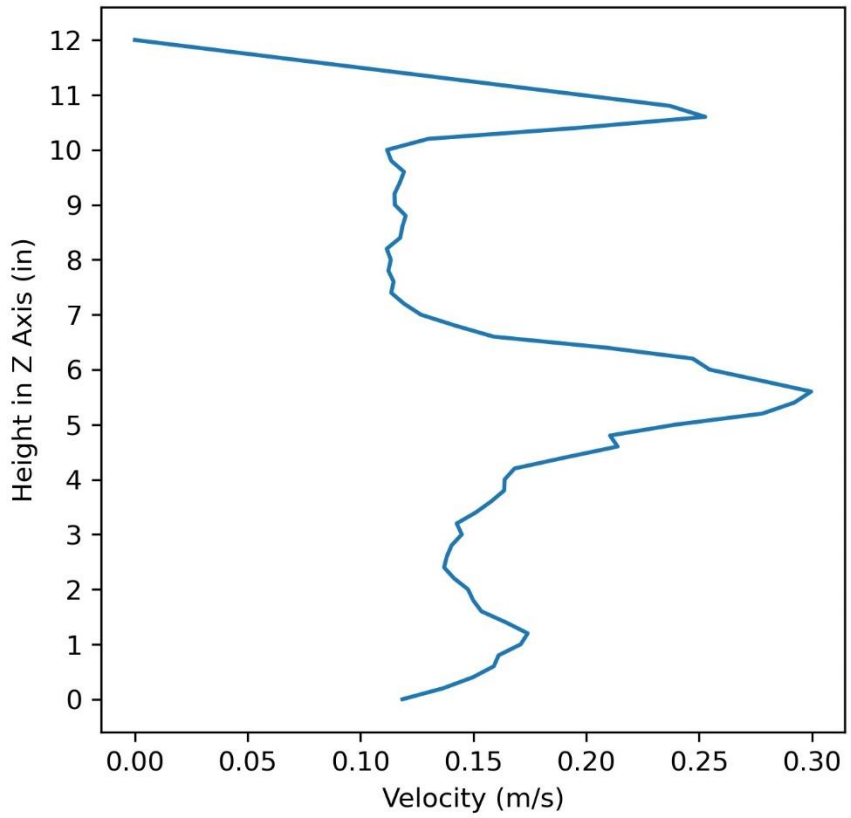

Figure 92: Mid-back port, 80 slpm

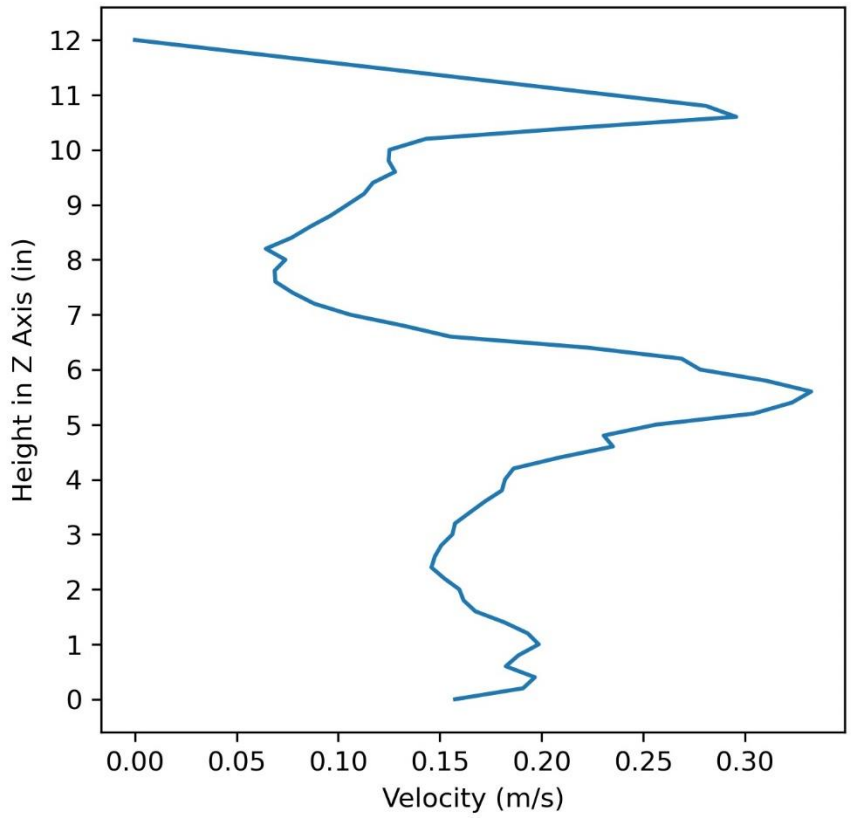

Figure 93: Mid-back port, 85 slpm

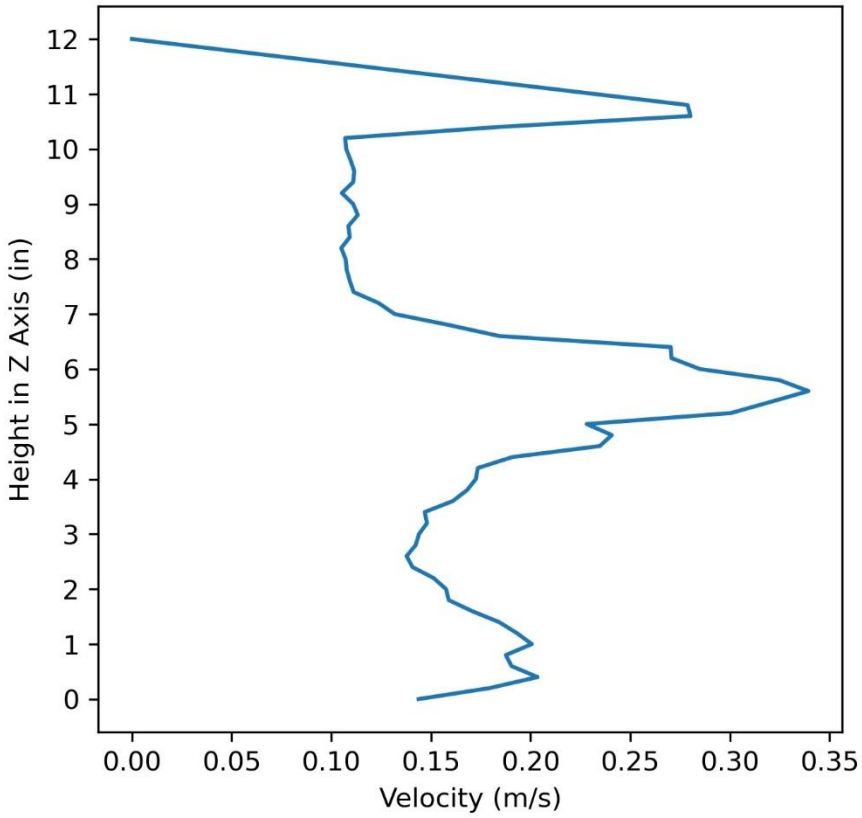

Figure 94: Mid-back port, 90 slpm

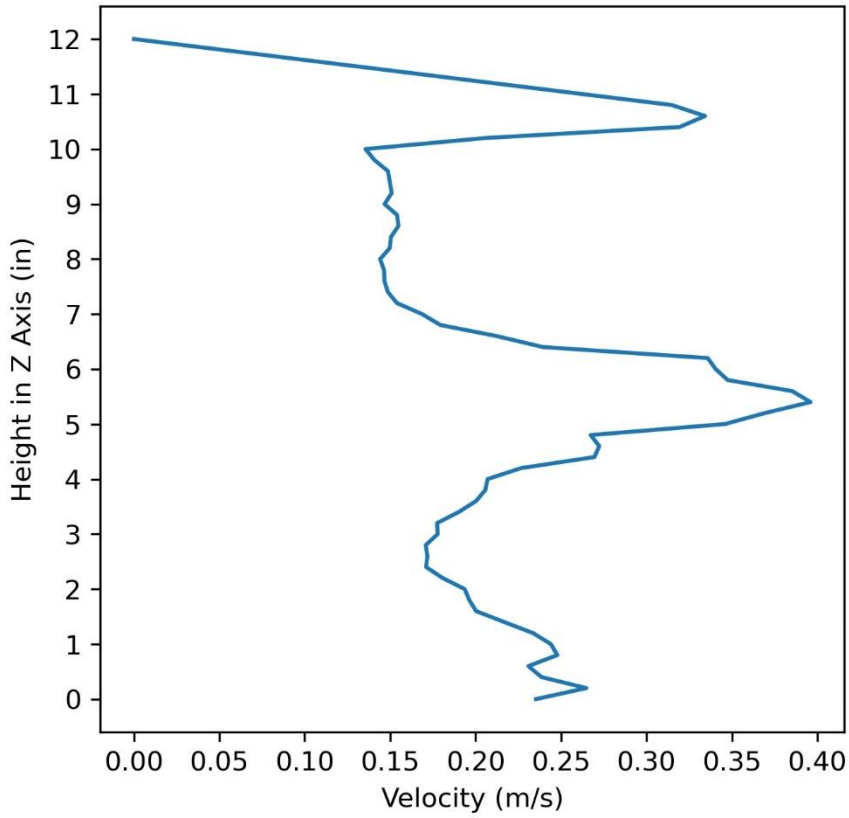

Figure 95: Mid-back port, 95 slpm

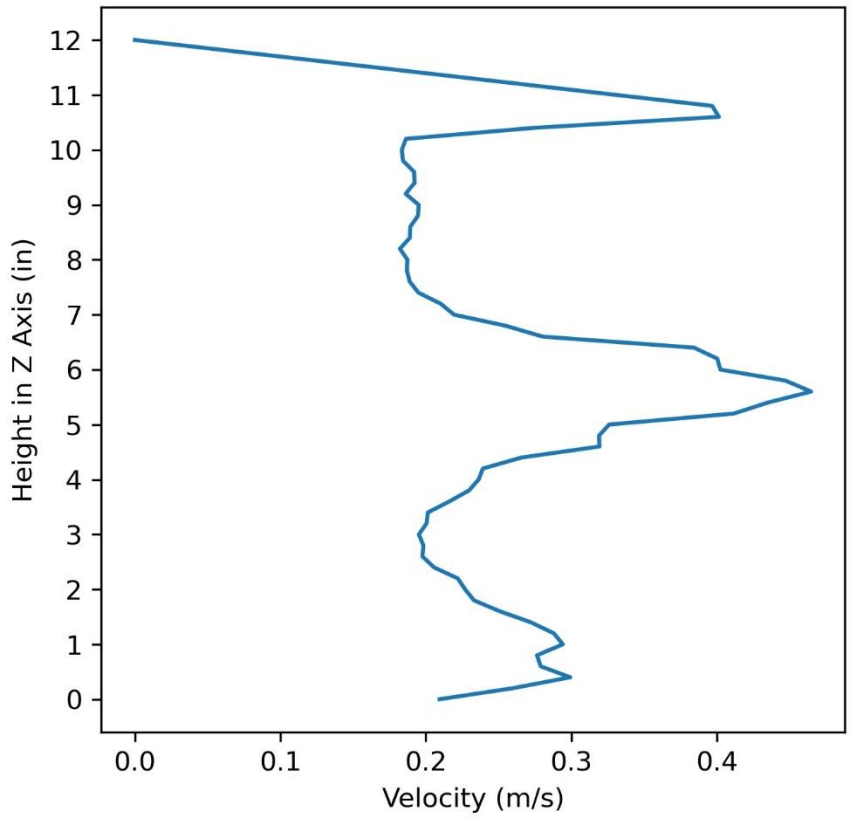

Figure 96: Mid-back port, 100 slpm

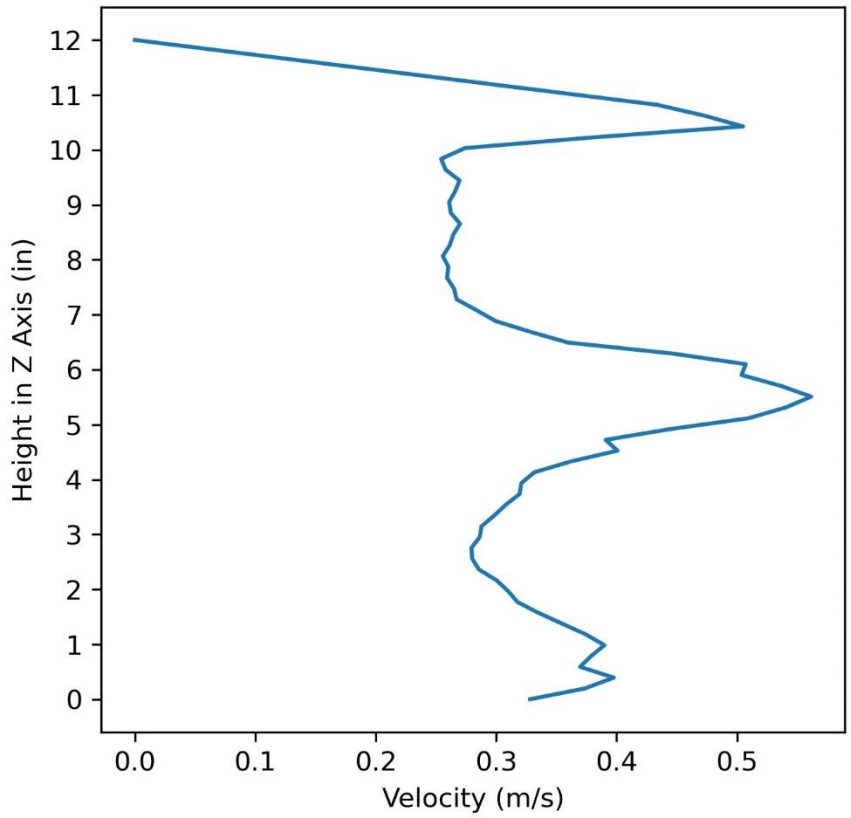

Figure 97: Mid-back port, 105 slpm

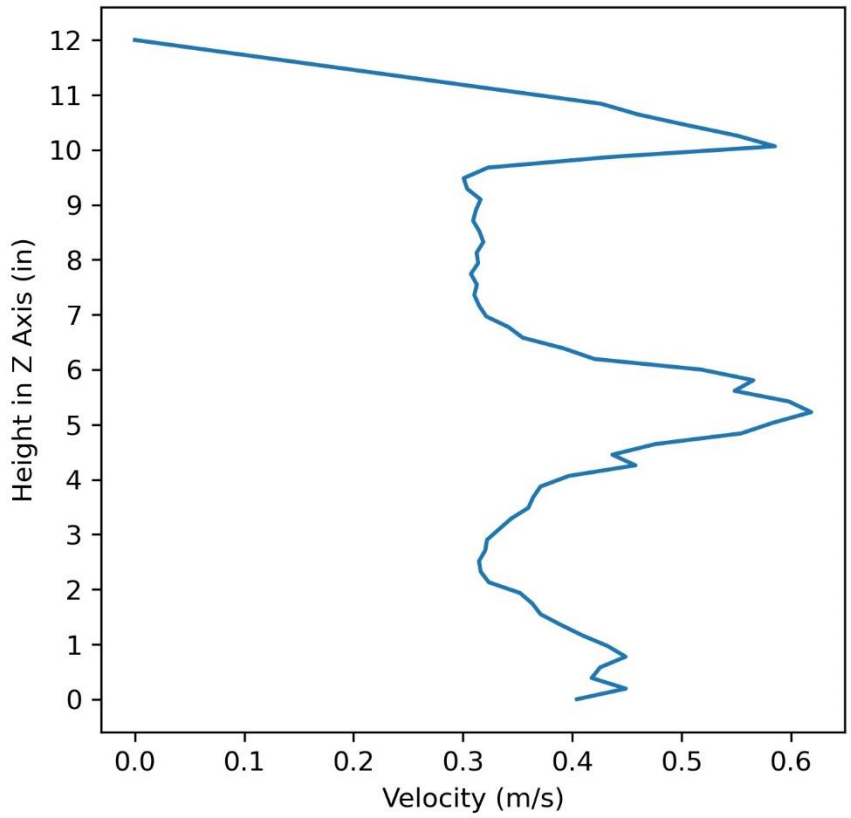

Figure 98: Mid-back port, 110 slpm

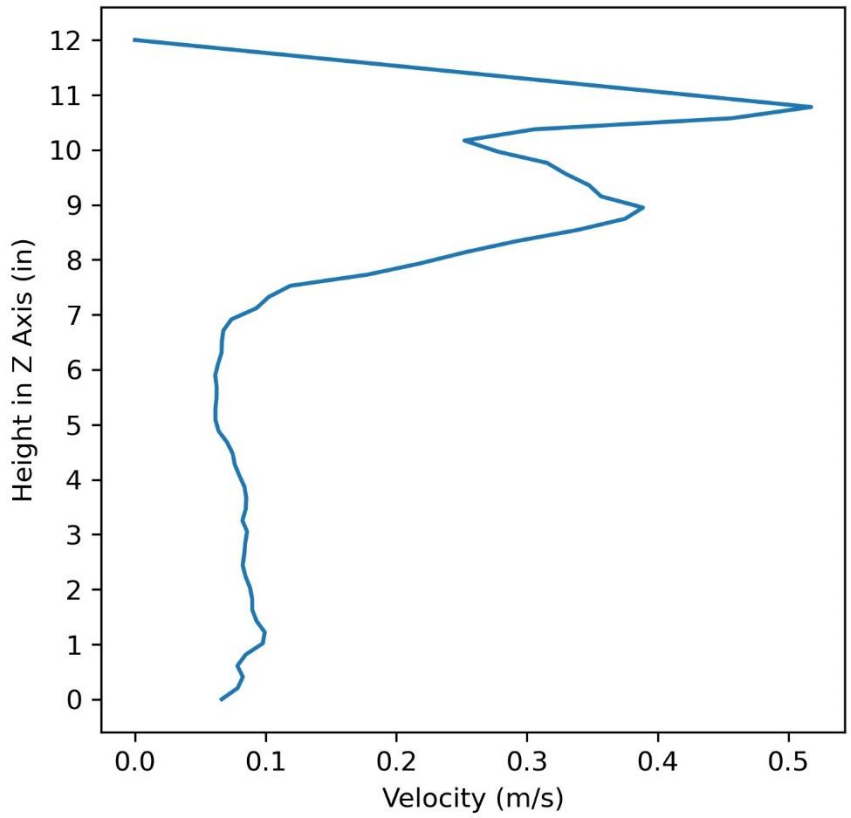

Figure 99: Top-back port, 75 slpm

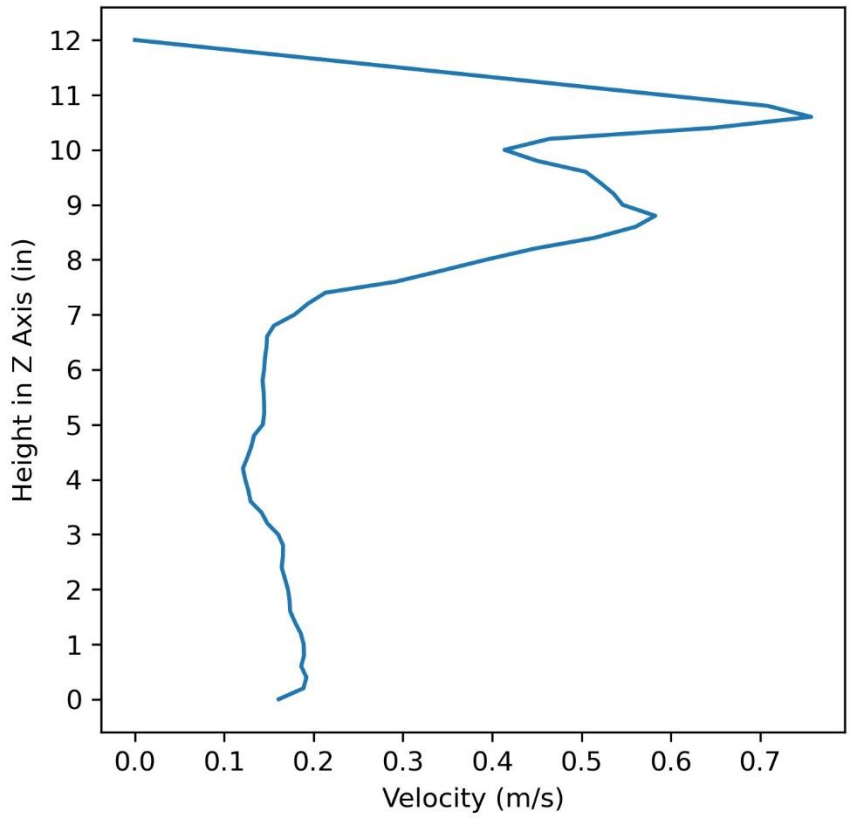

Figure 100: Top-back port, 80 slpm

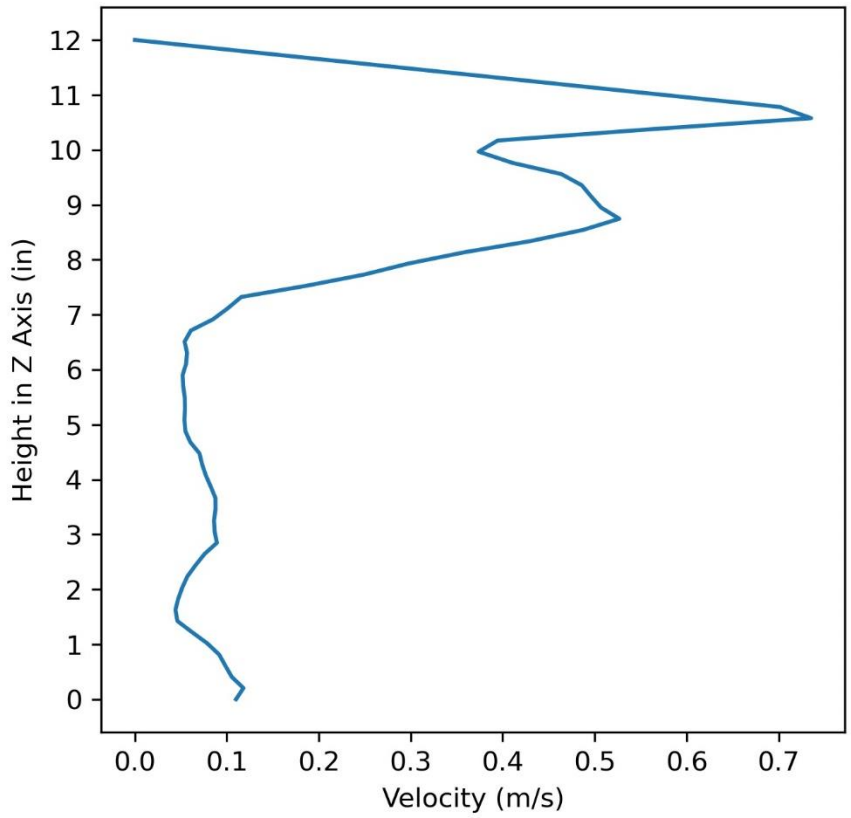

Figure 101: Top-back port, 85 slpm

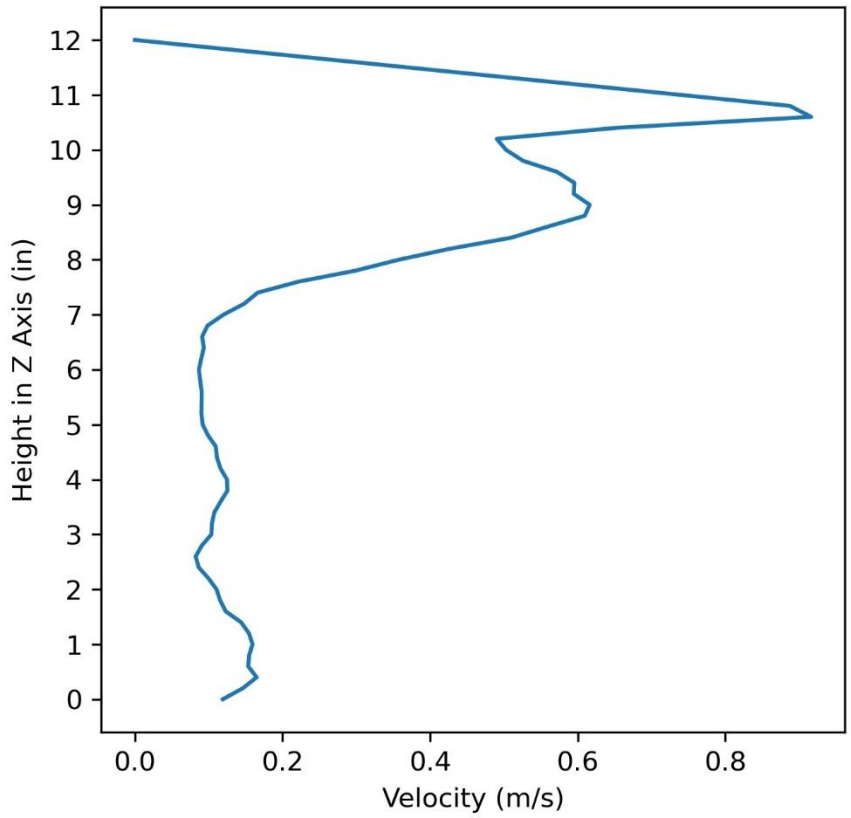

Figure 102: Top-back port, 90 slpm

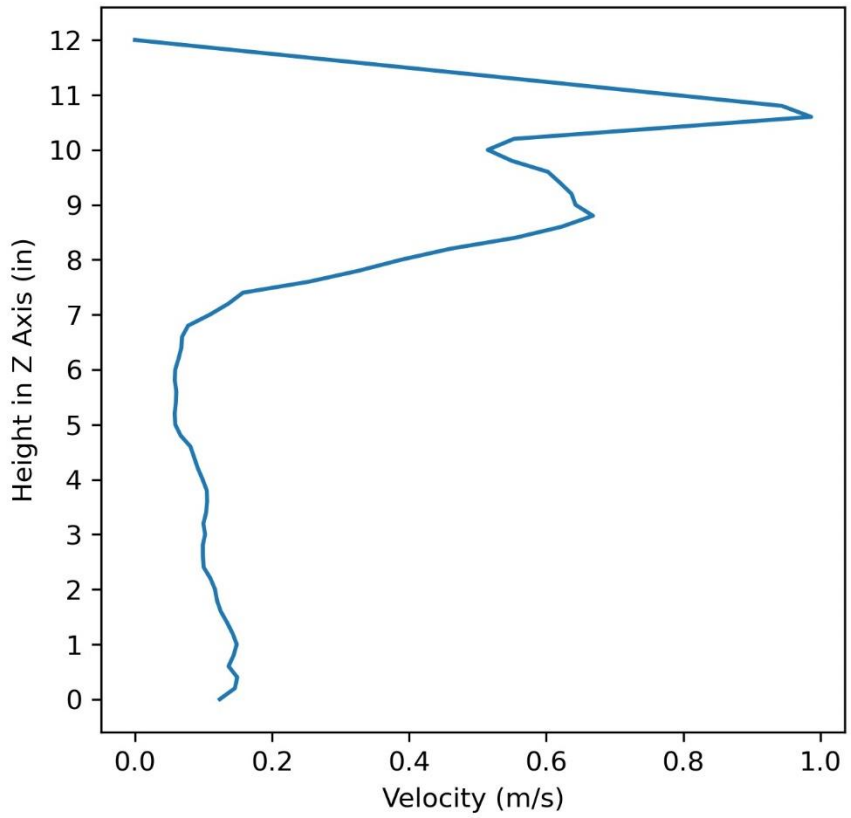

Figure 103: Top-back port, 95 slpm

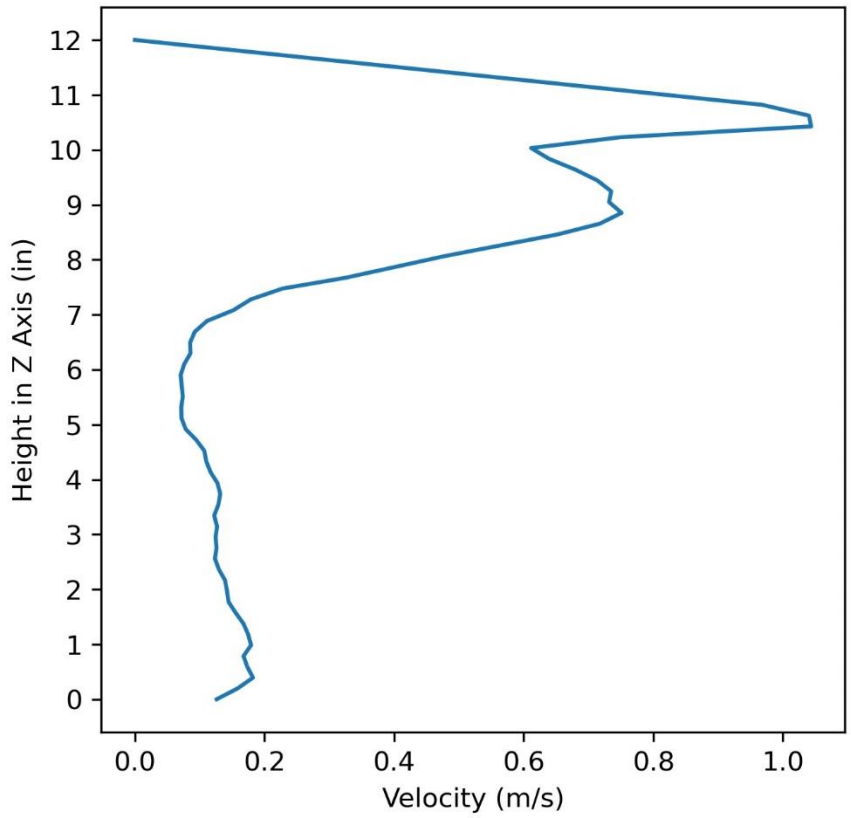

Figure 104: Top-back port, 100 slpm

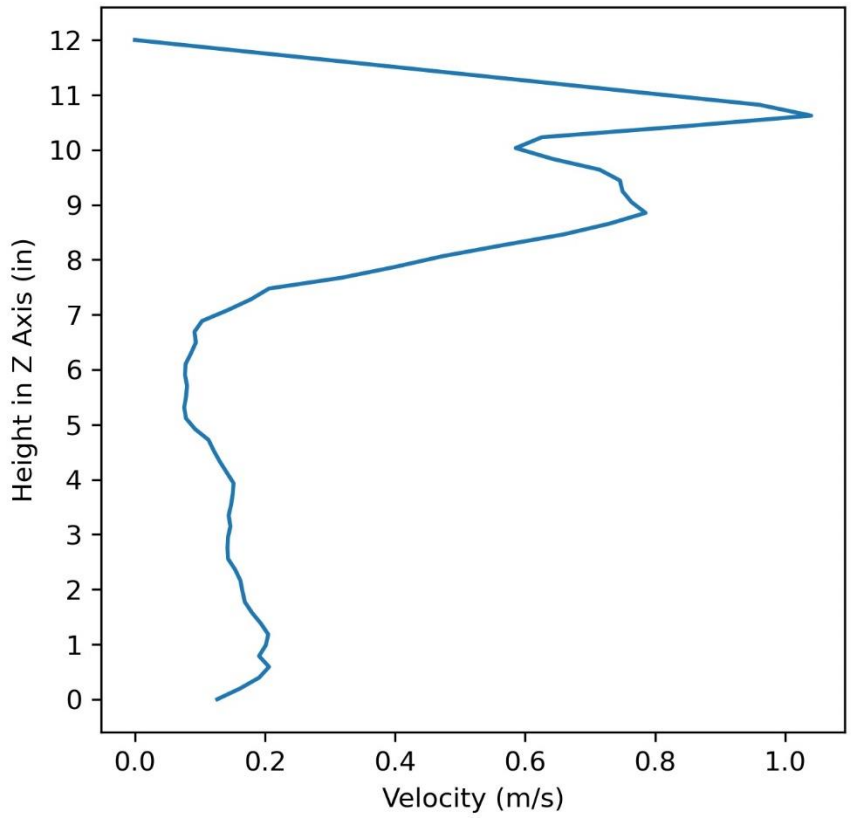

Figure 105: Top-back port, 105 slpm

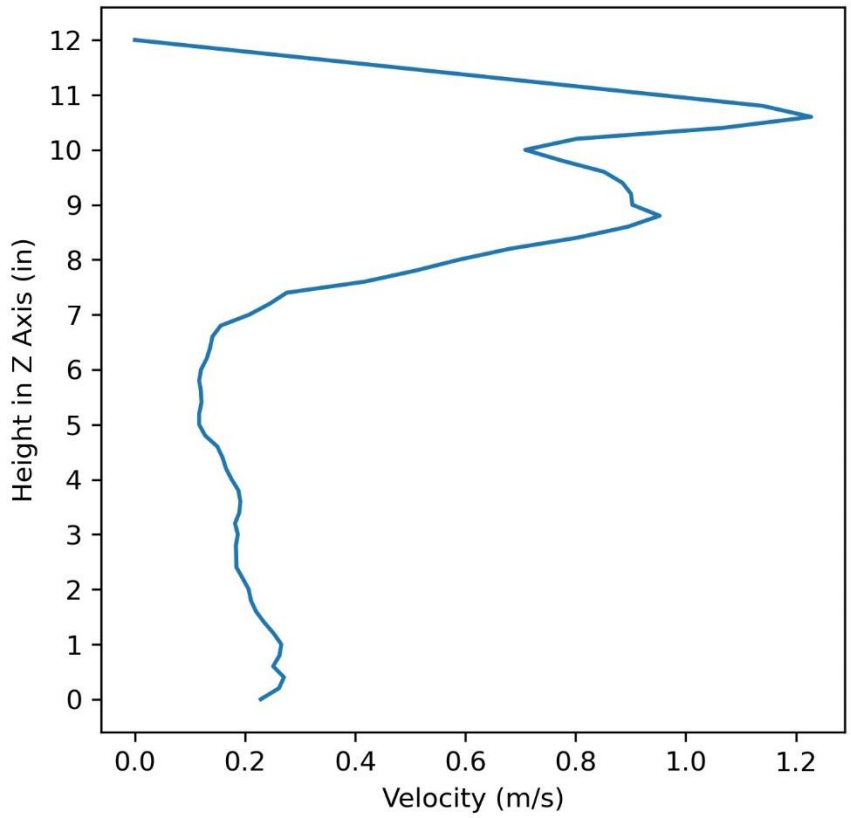

Figure 106: Top-back port, 110 slpm

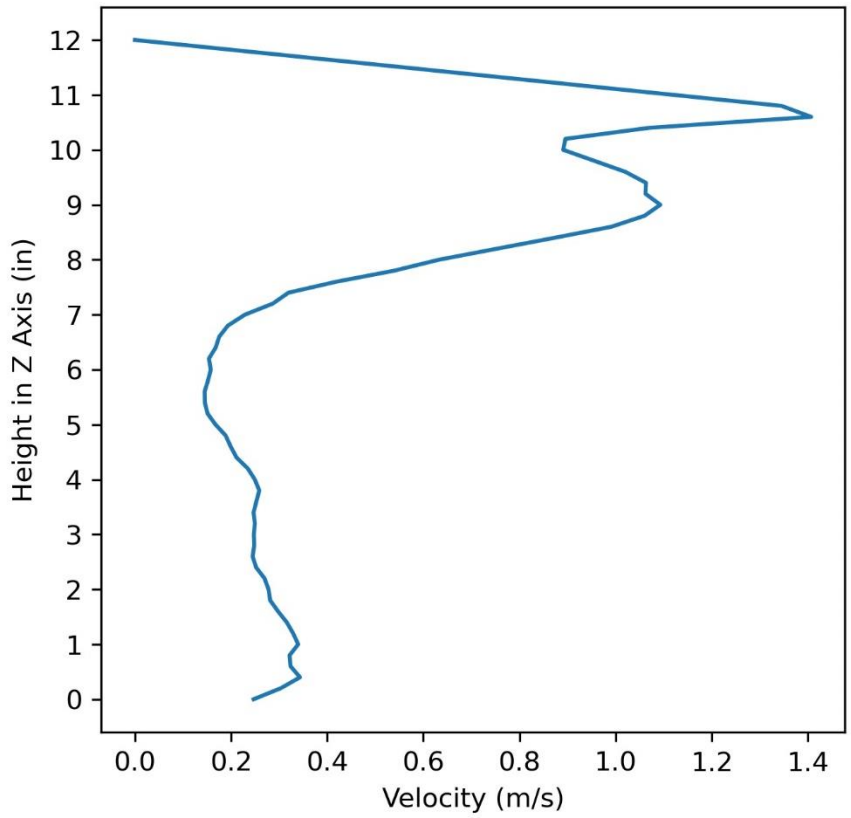

Figure 107: Top-back port, 115 slpm

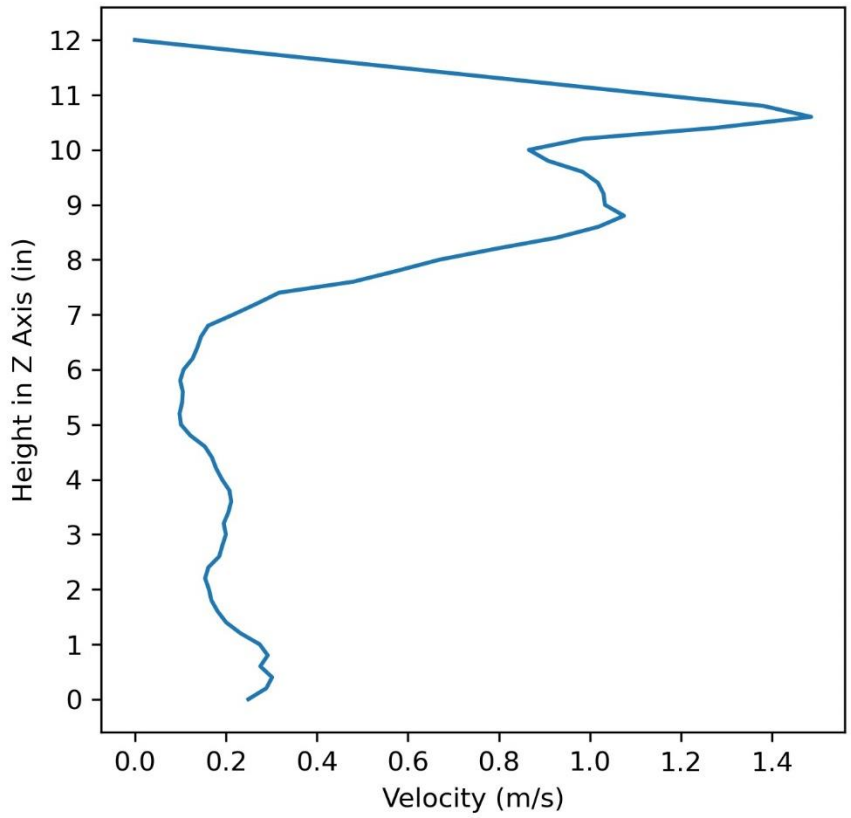

Figure 108: Top-back port, 120 slpm

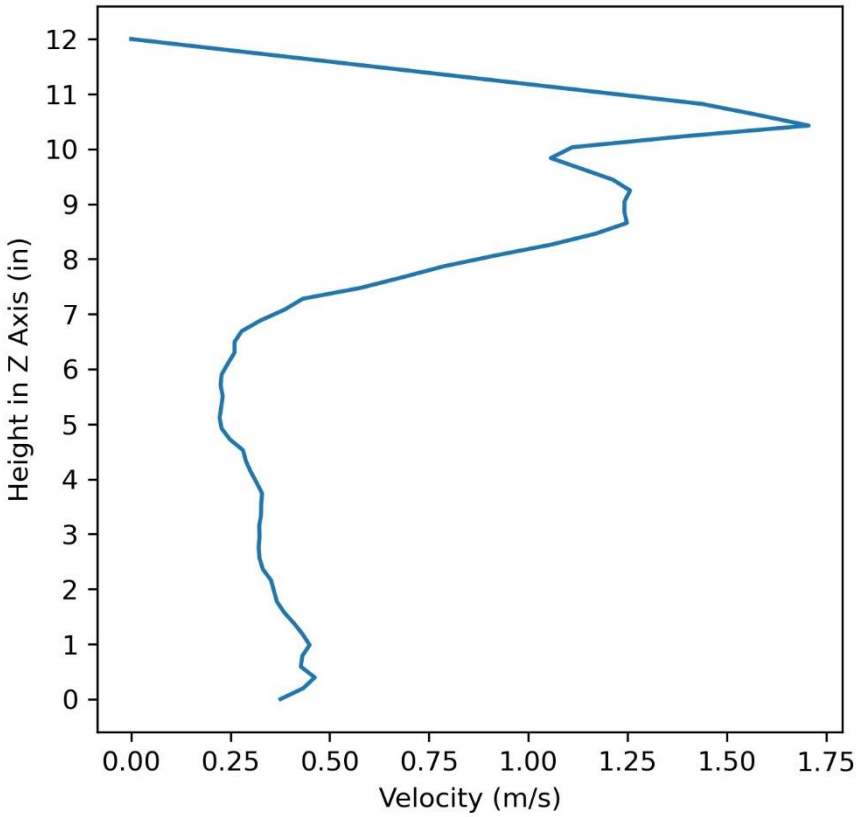

Figure 109: Top-back port, 125 slpm

Bibliography

[1] A. Tohidi, M. J. Gollner, and H. Xiao, “Fire Whirls,” *Annu. Rev. Fluid Mech*, vol. 50, pp. 187–213, 2018, doi: 10.1146/annurev-fluid-122316.

[2] H. Xiao, M. J. Gollner, and E. S. Oran, “From fire whirls to blue whirls and combustion with reduced pollution,” *Proc. Natl. Acad. Sci. U. S. A.*, vol. 113, no. 34, pp. 9457–9462, Aug. 2016, doi: 10.1073/pnas.1605860113.

[3] S. B. Hariharan, “The Structure of the Blue Whirl: A Soot-Free Reacting Vortex Phenomenon,” 2017.

[4] R. Zhou and Z. N. Wu, “Fire whirls due to surrounding flame sources and the influence of the rotation speed on the flame height,” *J. Fluid Mech.*, vol. 583, pp. 313–345, 2007, doi: 10.1017/S0022112007006337.

[5] A. Y. Snegirev, J. A. Marsden, J. Francis, and G. M. Makhviladze, “Numerical studies and experimental observations of whirling flames,” *Int. J. Heat Mass Transf.*, vol. 47, no. 12–13, pp. 2523–2539, 2004, doi: 10.1016/j.ijheatmasstransfer.2004.02.002.

[6] G. M. Byram and R. E. Martin, “The Modeling of Fire Whirlwinds,” *For. Sci.*, vol. 16, no. 4, pp. 386–399, Dec. 1970, doi: 10.1093/forestscience/16.4.386.

[7] C. M. Countryman, “Fire whirls... Why , When and Where,” *USFS Pacific Southwest Res. Stn.*, 1971.

[8] N. Liu, Q. Liu, Z. Deng, K. Satoh, and J. Zhu, “Burn-out time data analysis on interaction effects among multiple fires in fire arrays,” *Proc. Combust. Inst.*,

vol. 31 II, pp. 2589–2597, 2007, doi: 10.1016/j.proci.2006.08.110.

[9] R. I. Emori and K. Saito, “Model experiment of hazardous forest fire whirl,” *Fire Technol.*, vol. 18, no. 4, pp. 319–327, 1982, doi: 10.1007/BF02473115.

[10] K. Satoh and K. T. Yang, “Simulations of Swirling Fires Controlled by Channeled Self-generated Entrainment Flows.”

[11] M. I. Hassan, K. Kuwana, K. Saito, and F. Wang, “Flow Structure of a Fixed-frame Type Fire Whirl,” 2005.

[12] K. H. Chuah and G. Kushida, “The prediction of flame heights and flame shapes of small fire whirls,” *Proc. Combust. Inst.*, vol. 31 II, pp. 2599–2606, 2007, doi: 10.1016/j.proci.2006.07.109.

[13] Y. Hayashi, K. Kuwana, and R. Dobashi, “Influence of vortex structure on fire whirl behavior,” in *Fire Safety Science*, 2011, pp. 671–679, doi: 10.3801/IAFSS.FSS.10-671.

[14] K. Kuwana, S. Morishita, R. Dobashi, K. H. Chuah, and K. Saito, “The burning rate’s effect on the flame length of weak fire whirls,” *Proc. Combust. Inst.*, vol. 33, no. 2, pp. 2425–2432, 2011, doi: 10.1016/j.proci.2010.05.049.

[15] R. Dobashi, T. Okura, R. Nagaoka, Y. Hayashi, and T. Mogi, “Experimental Study on Flame Height and Radiant Heat of Fire Whirls,” *Fire Technol.*, vol. 52, no. 4, pp. 1069–1080, Jul. 2016, doi: 10.1007/s10694-015-0549-z.

[16] J. Lei *et al.*, “Experimental research on combustion dynamics of medium-scale fire whirl,” *Proc. Combust. Inst.*, vol. 33, no. 2, pp. 2407–2415, 2011, doi: 10.1016/j.proci.2010.06.009.

[17] K. Zhou, N. Liu, J. S. Lozano, Y. Shan, B. Yao, and K. Satoh, “Effect of flow circulation on combustion dynamics of fire whirl,” *Proc. Combust. Inst.*, vol. 34, no. 2, pp. 2617–2624, 2013, doi: 10.1016/j.proci.2012.06.053.

[18] P. Wang, N. Liu, L. Zhang, Y. Bai, and K. Satoh, “Fire Whirl Experimental Facility with No Enclosure of Solid Walls: Design and Validation,” *Fire Technol.*, vol. 51, no. 4, pp. 951–969, 2015, doi: 10.1007/s10694-014-0435-0.

[19] K. A. Hartl and A. J. Smits, “Scaling of a small scale burner fire whirl,” *Combust. Flame*, vol. 163, pp. 202–208, 2016, doi: 10.1016/j.combustflame.2015.09.027.

[20] J. D. Chung, “NUMERICAL SIMULATION OF THE BLUE WHIRL: A REACTING VORTEX BREAKDOWN PHENOMENON,” 2019.

[21] J. D. Chung, X. Zhang, C. R. Kaplan, and E. S. Oran, “The Strucuture of the Blue Whirl Revealed,” *Sci. Adv.*, vol. 6, 2020.

[22] X. Zhang, J. D. Chung, C. R. Kaplan, and E. S. Oran, “The barely implicit correction algorithm for low-Mach-Number flows,” *Comput. Fluids*, vol. 175, pp. 230–245, Oct. 2018, doi: 10.1016/j.compfluid.2018.08.019.

[23] J. D. Chung, X. Zhang, C. R. Kaplan, and E. S. Oran, “Low-mach-number simulation of diffusion flames with the chemical-diffusive model,” *AIAA Scitech 2019 Forum*, no. January, pp. 1–10, 2019, doi: 10.2514/6.2019-2169.

[24] J. Carpio, W. Coenen, A. L. Sánchez, E. Oran, and F. A. Williams, “Numerical description of axisymmetric blue whirls over liquid-fuel pools,” *Proc. Combust. Inst.*, vol. 000, pp. 1–8, 2020, doi: 10.1016/j.proci.2020.06.327.

[25] Y. Hu, S. B. Hariharan, H. Qi, M. J. Gollner, and E. S. Oran, “Conditions for formation of the blue whirl,” *Combust. Flame*, vol. 205, pp. 147–153, 2019, doi: 10.1016/j.combustflame.2019.03.043.

[26] S. B. Hariharan, Y. Hu, M. J. Gollner, and E. S. Oran, “Effects of circulation and buoyancy on the transition from a fire whirl to a blue whirl,” *Phys. Rev. Fluids*, vol. 5, no. 10, p. undefined, Oct. 2020, doi: 10.1103/PhysRevFluids.5.103201.

[27] W. Coenen, E. J. Kolb, A. L. Sánchez, and F. A. Williams, “Observed dependence of characteristics of liquid-pool fires on swirl magnitude,” *Combust. Flame*, vol. 205, pp. 1–6, 2019, doi: 10.1016/j.combustflame.2019.03.032.

[28] P. Anderson, L. Price, S. Gunukula, and D. T. Tran, “Blue Whirl Phenomenon: A Potential Fuel-Flexible and Soot-Free Combustion Technology,” *Energy and Fuels*, vol. 34, no. 9, pp. 11708–11711, 2020, doi: 10.1021/acs.energyfuels.0c01979.

[29] D. H. Peckham and S. A. Atkinson, “Preliminary Results of Low Speed Wind Tunnel Tests on a Gothic Wing of Aspect Ratio 1.0,” *A. R. C. Tech. Rep.*, p. 38, 1957.

[30] J. K. Harvey, “Some observations of the vortex breakdown phenomenon,” *J. Fluid Mech.*, vol. 14, no. 4, pp. 585–592, 1962, doi: 10.1017/S0022112062001470.

[31] J. J. Cassidy and H. T. Falvey, “Observations of unsteady flow arising after

vortex breakdown," *J. Fluid Mech.*, vol. 41, no. 4, pp. 727–736, 1970, doi: 10.1017/S0022112070000873.

[32] T. Sarpkaya, "Vortex breakdown in swirling conical flows," *AIAA J.*, vol. 9, no. 9, pp. 1792–1799, 1971, doi: 10.2514/3.49981.

[33] J. H. Faler and S. Leibovich, "An experimental map of the internal structure of a vortex breakdown," *J. Fluid Mech.*, vol. 86, no. 2, pp. 313–335, 1978, doi: 10.1017/S0022112078001159.

[34] O. Lucca-Negro and T. O'Doherty, "Vortex breakdown: a review," *Prog. Energy Combust. Sci.*, vol. 27, pp. 431–481, 2001.

[35] S. Leibovich, "The Structure of Vortex Breakdown," *Ann. Rev. Fluid Mech.*, vol. 10, pp. 221–246, 1978.

[36] M. G. Hall, "Vortex Breakdown," *Annu. Rev. Fluid Mech.*, vol. 4, no. 1, pp. 195–218, 1972, doi: 10.1146/annurev.fl.04.010172.001211.

[37] T. Sarpkaya, "Effect of the adverse pressure gradient on vortex breakdown," *AIAA J.*, vol. 12, no. 5, pp. 602–607, 1974, doi: 10.2514/3.49305.

[38] T. Sarpkaya, "On stationary and travelling vortex breakdowns," *J. Fluid Mech.*, vol. 45, no. 3, pp. 545–559, 1971, doi: 10.1017/S0022112071000181.

[39] C. Brücker and W. Althaus, "Study of vortex breakdown by particle tracking velocimetry (PTV) - Part 1: Bubble-type vortex breakdown," *Exp. Fluids*, vol. 13, no. 5, pp. 339–349, 1992, doi: 10.1007/BF00209508.

[40] C. Brücker, "Study of vortex breakdown by particle tracking velocimetry (PTV) - Part 2: Sprial-type vortex breakdown," *Exp. Fluids*, vol. 139, pp. 133–

139, 1993.

[41] J. M. Burgers, “A Mathematical Model Illustrating the Theory of Turbulence,” *Adv. Appl. Math.*, vol. 1, pp. 171–199, 1948.

[42] V. K. Horváth, J. R. Cressman, W. I. Goldburg, and X. L. Wu, “Hysteresis at low Reynolds number: Onset of two-dimensional vortex shedding,” *Phys. Rev. E - Stat. Physics, Plasmas, Fluids, Relat. Interdiscip. Top.*, vol. 61, no. 5, pp. 4702–4705, 2000, doi: 10.1103/PhysRevE.61.R4702.

[43] M. J. Tummers, A. W. Hübner, E. H. van Veen, K. Hanjalić, and T. H. van der Meer, “Hysteresis and transition in swirling nonpremixed flames,” *Combust. Flame*, vol. 156, no. 2, pp. 447–459, 2009, doi: 10.1016/j.combustflame.2008.10.027.

[44] M. J. Tummers, A. W. Hubner, K. Hanjalic, J. D. E. . Roekarts, and T. H. van der Meer, “Flow Field Measurements in Swirling Nonpremixed Turbulent Flames,” 2007.

[45] S. R. Turns and D. C. Haworth, *An Introduction to Combustion Concepts and Applications, Fourth Edition*. McGraw Hill LLC, 2021.